AMERICAN UNIVERSITY OF BEIRUT

LOW INTENSITY ULTRASOUND FOR SUPPRESSION OF

PERIPHERAL NERVE ACTIVITY

by
RIMA HAZEM EL HASSAN

A thesis
submitted in partial fulfillment of the requirements
for the degree of Master of Science
to the Biomedical Engineering Program
of the Maroun Semaan Faculty of Engineering & Architecture and the Faculty of Medicine
at the American University of Beirut

Beirut, Lebanon
January 2020

AMERICAN UNIVERSITY OF BEIRUT

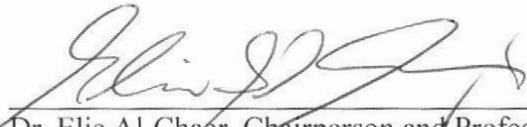LOW INTENSITY ULTRASOUND FOR SUPPRESSION OF

PERIPHERAL NERVE ACTIVITY

by
RIMA H. EL HASSAN

Approved by:

_____

Dr. Massoud Khraiche, Assistant Professor   Advisor
Biomedical Engineering Program
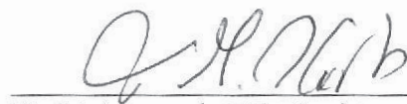Maroun Semaan Faculty of Engineering & Architecture

_____

Dr. Elie Al-Chaer, Chairperson and Professor   Co-Advisor
Department of Anatomy, Cell Biology and Physiological Sciences
Faculty of Medicine

_____

Dr. Zaher Dawy, Professor   Member of Committee
Department of Electrical and Computer Engineering
Maroun Semaan Faculty of Engineering & Architecture

_____

Dr. Mohammad Harb, Assistant Professor   Member of Committee
Department of Mechanical Engineering
Maroun Semaan Faculty of Engineering & Architecture

Date of thesis/dissertation defense: February 10, 2020

AMERICAN UNIVERSITY OF BEIRUT

THESIS, DISSERTATION, PROJECT RELEASE FORM

Student Name: __EL HASSAN_____RIMA_____HAZEM___
                     Last   First   Middle

☑ Master's Thesis   ◯ Master's Project   ◯ Doctoral Dissertation

☐   I authorize the American University of Beirut to: (a) reproduce hard or electronic copies of my thesis, dissertation, or project; (b) include such copies in the archives and digital repositories of the University; and (c) make freely available such copies to third parties for research or educational purposes.

☑   I authorize the American University of Beirut, to: (a) reproduce hard or electronic copies of it; (b) include such copies in the archives and digital repositories of the University; and (c) make freely available such copies to third parties for research or educational purposes

after : **One ---- year from the date of submission of my thesis, dissertation, or project.**
       Two ---- years from the date of submission of my thesis, dissertation, or project.
    ☑ **Three ---- years from the date of submission of my thesis, dissertation, or project.**

_Rima.H_____   _Feb 17, 2020_____

Signature   Date

ACKNOWLEDGMENTS

AN ABSTRACT OF THE THESIS OF

Rima El Hassan   for Master of Science
                             Major: Biomedical Engineering

Title: Neuromodulation of Neural Networks using Low Intensity Ultrasound
       Stimulation

Pain is commonly defined as "*an unpleasant sensory and emotional experience that is associated with actual or potential tissue damage*", yet physiologically, pain is simply a high frequency or high intensity stimulus in the nervous system. Research has shown that pain can be lessened by electrically stimulation specific regions in the central or peripheral nervous system. Electrical stimulation of the nervous system emerged as a clinically approved stimulating modality. This modality was successful in reducing symptoms but caused the formation of scar tissue. Therefore, considering new modalities became necessary to replace electrical stimulation. Over the years, ultrasound technology gained a major role in diagnostics and therapeutics. The broad range of intensities and frequencies of ultrasound signals, and the ability of their beams to be focused to propagate deeply through tissues into small scale targets non-invasively, made ultrasound technology very interesting for healthcare applications. In this work, the interest is in low intensity low frequency ultrasound stimulation of the peripheral nervous system that neuromodulates the behavior of neural networks and decreases pain sensation. The aim of the project is to study the effect of ultrasound stimulation on certain pain pathways in the peripheral nervous system, namely the reflex arc. Ultrasound stimulation is applied via an immersible transducer targeting the sciatic nerve in the Sprague Dawley rat animal model. The stimulation showed a decrease in the activity of the gastrocnemius muscle controlled by the sciatic nerve, and thus reduction of pain sensation. The mechanism of action of this mechanical stimulation modality remains unknown which channels our focus on developing a mechanical model that incorporates ultrasound stimulation into the existing electrical model of Hodgkin and Huxley for neural excitation. Mechanical forces including mechanical tension induced due to ultrasound stimulation, mechanical tension due to membrane voltage variation, and flexoelectric currents are incorporated to the Hodgkin-Huxley model and cause changes in amplitude, frequency and latency of action potential.

CONTENTS

ILLUSTRATIONS

TABLES

CHAPTER 1

INTRODUCTION

The human life begins with childbirth pain, continues with pathophysiological and emotional pain, and ends with death pain. Throughout history, the definition of pain progressed to become: "an unpleasant sensory and emotional experience that is associated with actual or potential tissue damage". This experience differs from one person to another and is a subjective incident than can neither be measured nor quantified. The most common pain control method is admission of analgesic drugs. Although analgesics showed great success, but they suffered from side effects varying from as simple as drowsiness and constipation to as complex as hallucinations, seizures, addiction, and severe allergic reactions. A second recent and successful treatment is the electrical stimulation of the central (CNS) and peripheral nervous system (PNS). In the CNS, deep brain stimulation of specific regions causes the formation of scar tissue which shortens the lifespan of the implanted device and causes the return of the pain experience. On the other hand, the stimulation of the spinal cord can cause hematoma, paralysis, epidural hemorrhage, and cerebrospinal fluid leakage. The severe complications accompanied with electrical stimulation caused the need for a new modality to stimulate the nervous system. this thesis will serve the purpose of exploring ultrasound as a stimulation modality to relief pain.

Ultrasound signals are mechanical vibrations with frequencies above the normal human hearing range (20Hz-20 kHz). Due to the ability of these signals to penetrate through human tissue and organs, they have long been used as diagnostic imaging

technologies, creating real-time images of soft tissues and measuring arterial blood flow. Recently, ultrasound emerged as a tool for therapeutics including drug and gene delivery, inflammatory inhibition, ablation, and tissue regeneration. In our work, we use the ultrasound technology to modulate the behavior of neural networks. We aim to characterize an ultrasound transducer to become a stimulation tool for specific neural pathways. This leads to exploring the effect of ultrasound mechanical stimulation on neural networks and classifying them as inhibitory, excitatory, or both depending at the targeted site or stimulation parameters. In the first part of the work, we aim at modulating pain through targeting the reflex arc- sciatic nerve- in the rat animal model, while in the second we develop a mechanical model that attempts to understand the mechanism of action of ultrasound stimulation on a single nerve fiber.

CHAPTER 2

LITERATURE REVIEW

2.1. Pain in the Nervous System

The *International Association for the Study of Pain* defined pain as a non-objective, sensory and emotional experience, associated with real or potential injuries, and affected by previous experiences [1]. The neural pain pathways are composed of the: (1) peripheral receptors (nociceptors), (2) peripheral afferent fibers, (3) the spinal cord, (4) peripheral efferent fibers, and (5) peripheral effectors. The pathways travel in dedicated tracts in the spinal cord, to and from the central nervous system [2].

The processing of the pain experience is composed of four major parts: (1) transduction, (2) transmission, (3) perception, and (4) modulation (Figure. 2.1). Transduction begins at the nociceptors that sense mechanical, heat or chemical intense stimuli and transform the stimulus into electrical signals. Then these signals are transmitted from the nociceptors to the spinal cord, namely the central pain-transmission cells, via peripheral afferent fibers. Transmission resumes from the central pain-transmission cells to the thalamus and then the cerebral cortex in the brain. In the brain, frequency and intensity of the electrical impulses are perceived and relayed to the midbrain and medulla of the spinal cord. These signals are modulated, the sensation is inhibited. Inhibition occurs either due to the activation of neural networks that have an inhibitory effect on the painful signal or due to activation of analgesia networks by substances that are pharmacologically compatible with synthetic drugs and some plant derived opiates. Finally, modulated electrical signals are relayed through efferent nerve fibers to the peripheral effectors or tissue [3].
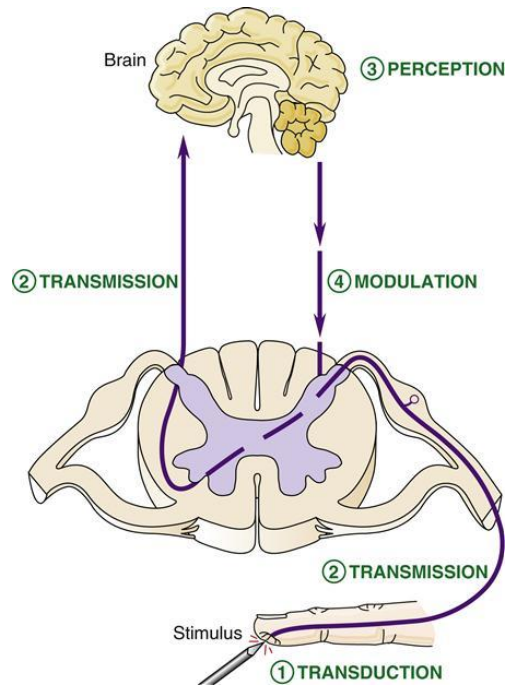
Figure. 2.1: Pain signaling [4]

Current treatments for acute and chronic pain include pharmaceutical drugs, spinal cord stimulation, deep brain stimulation , and motor cortex stimulation [5-12]. Pharmaceuticals for pain treatment fall within 3 main classes: (1) Non-opioid analgesics, (2) adjuvant analgesics, and (3) opioid analgesics. Class 1 works on inhibiting enzymes whose presence cause inflammation and pain. Class 2 are drugs used for indications other than pain but also provide pain relief. Class 3 are substances that act on opioid receptors in the nervous system causing morphine -like effects and relieve pain [6]. Over the years, reports of analgesic misuse and addiction cases are increasing dramatically [5, 7]. Deep brain stimulation (DBS) for pain relief initiated in 1953 [8]. DBS involves an implant that delivers electric impulses to specific regions deep in the brain. Common DBS targets included the sensory thalamus, periventricular grey, the periaqueductal grey, and the sensory thalamus capsule [9, 10]. In 1991, motor cortex stimulation (MCS) was introduced [11]. Unlike DBS, MCS procedures place electrodes at the surface of the brain

allowing electrical impulses to be delivered to the motor cortex. Both DBS and MCS serve as effective tools for suppressing for a short period of time due to the formation of scar tissue which renders the implants redundant with the onset of pain sensation again. Moreover, both technologies make patients highly susceptible to seizures, infections, and strokes. Finally, spinal cord stimulation (SCS) targets regions in the spinal cord. This technology has shown more success than DBS and MCS, yet still suffers from complications including infection, allergic reactions, epidural hematoma, and dural puncture [12]. DBS, MCS, and SPS are all invasive methods that implant devices into the body and increase the risk of inflammation and immune responses, which raise the interest in a non-invasive modality such as ultrasound stimulation.

One of the commonly studied pain pathways is the reflex arc due to its simple anatomical structure, where pain signals travel across synapses in the spinal cord and not into the brain. The pathway is activated when an intense stimulus is encountered. The signal travels to the spinal cord through afferent sensory neuron and back to the effector muscles through the efferent motor neurons [13].
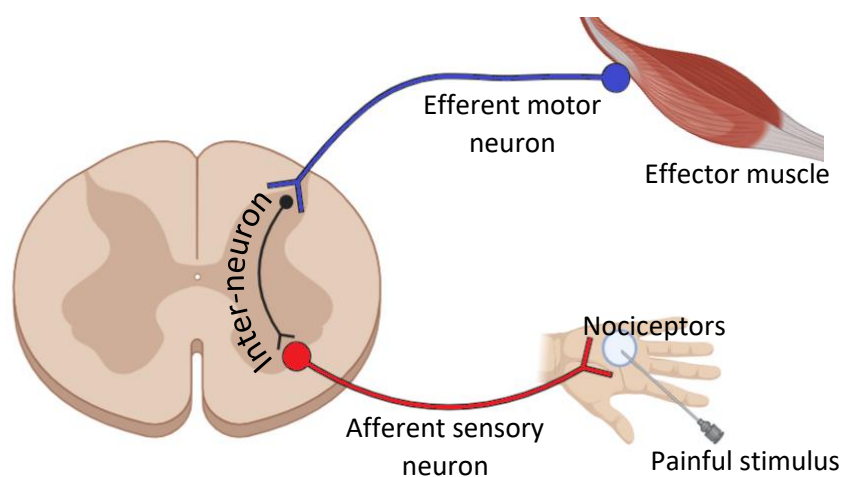
Figure. 2.2: Reflex Arc

In animal models, the reflex arc has been the target of neuromodulation in several studies and we shall study this pathway to understand the effect of low intensity US on the suppression of pain activity in this reflex arc [2]. Several works addressed the US stimulation effect on animal models, with the sciatic nerve being the target [14] since it represents one of the reflex arcs in the body. The sciatic nerve in the rat animal model emerges from the lumbar segments L4 and L6. The large nerve diverges into two and then into 4 and includes both sensory afferent and motor efferent fibers. The sciatic nerve is connected to the hindlimb in rats and causes its movement in response to stimuli [15]. Any neural activity in the sciatic nerve is reflected in the muscle activity of the hindlimb (gastrocnemius muscle) and can be detected using electromyograms (EMG). When any physically painful stimulus is applied to the hind limb, the reflex arc is activated and the animal twitches or withdraws its limb. In this case, the EMG records the afferent sensory stimulus to the spinal cord and the efferent motor responses to the muscles. Therefore, in our work, we will stimulate the reflex arc, i.e. the sciatic nerve, electrically via current injection, and apply mechanical ultrasound stimulation, and study the effect of this stimulation, regardless of its nature -excitatory or inhibitory- through the EMG recordings showing efferent responses.

2.2. Ultrasound in Diagnostics

Ultrasound (US) waves were first used as diagnostic tools in 1942 by neurologist Karl Dussik when he tried detecting brain tumors through ultrasound beam transmission into the human skull [16]. The technology evolved into a powerful imaging tool used for diagnosis [17-19] and image-guided surgeries [20-24]. Diagnostic US imaging involves intensities within the range of 0.05 to $0.5W/cm^2$ and frequencies between 2 and 18MHz

[25] ; these tools are capable of constructing 3D images [26, 27], measuring muscle contraction [28], and monitoring real-time blood flow [29, 30]. US is also used either alone [31-33] or with magnetic resonance imaging [23] to assist surgeons during operations or with US stimulation[20-22, 24].

2. 3. Ultrasound in Therapeutics

US then emerged as a successful therapeutic tool due to its nature - a mechanical wave- and its ability to be transmitted noninvasively to tissues and body organs. Therapeutic US can be either low or high intensity [34]. High intensity focused ultrasound (HIFU) ranges between 0.8 and 3.5MHz [35]. When these high frequency signals are focused, they carry amounts of energy capable of inducing heating effects and even burning tissues [36]. Therefore, HIFU is used for thermal ablation of tumors [31, 37-39], ablation in the central nervous system (CNS) where targets include areas involved in epilepsy [39, 40], Parkinson [41], and tremor [42, 43], and disruption or opening of the blood-brain barrier (BBB) [44-50] for drug and gene delivery. HIFU is also being tested on rabbits to noninvasively remove occlusions in prenatal tracheas [51]. Low intensity focused ultrasound (LIFU), which ranges from 200 to 800 kHz, is more widely used than HIFU. Uddin et al. used LIFU to enhance mesenchymal stem cell differentiation [52]. Using LIFU, Zheng et al. attenuated cardiac inflammation [33]. Rego et al. used low intensity US in dental treatments and promoted periodontal ligament regeneration, restored damaged dental roots, and decreased root resorption [53]. LIFU was used in bone healing [32, 54-59], soft tissue regeneration [32, 60, 61], axon regeneration [62], dementia treatment [63], osteoarthritis treatments [64], and protein and gene expression [65-67]. Kirupa et al. applied US stimulation to reduce pain in joint disorders and the reduction

was found more effective than electrical stimulation [68]. Finally, LIFU is currently being explored for neuromodulation of neural networks in the central and peripheral nervous system [69-76].

2.4. Ultrasound in Neuromodulation

The first attempt to use non-invasive ultrasound to modulate neural networks was in 1928 by Harvey and Loomis who observed suppression of excitation of the sciatic nerve when exposed to US waves and stimulated by touch [77]. Later, Fry et al. were successful in suppressing electrical responses in the visual cortex upon subjecting an exposed brain to US waves [78]. Gavrilov showed changes in neural activity upon exposure to US signal [76]. Forester et al. used 1MHz, 1 W/cm^2 US signals on cats under a hypoxic episode to depress visually evoked potentials [69]. Velling and Shklyaruk noticed that FUS has no effect on the brain when the applied intensity is below 0.1mW/cm^2, while this effect causes suppression of Electrocorticography (EcoG) activity at intensities between 1 and 100W/cm^2 [75]. Bachtold et al. studied focused pulsed US with a frequency of 500kHz and pulse frequency 200kHz and observed depression of electrically evoked potentials in rat hippocampal neurons [79]. Tsui et al. exposed excised frog sciatic nerves to 3.5MHz continuous US waves at intensities ranging between 1 and 5 Watts for 5 mins. At intensities of 1 to 3W, the conduction velocity increased by 5 to 20%. As for the evoked compound potential, it increased by 8% at 1W US stimulation then decreased progressively as the US stimulation intensity increased [72]. As advances occurred in ultrasound transducer fabrication and focusing methods [80, 81], US neuromodulation experiments started to increase. Foley et al. exposed rat sciatic nerves and subjected them to HIFU with a frequency of 5.7MHz and intensities

ranging from 390 to 7890 W/cm^2. Muscle potentials were suppressed in lower intensities and recovered after 28 days. As for higher intensities, muscle potentials didn't recover even after 28days. Histology showed damage to the nerves exposed to higher intensities with presence of Shawn cells and hemorrhagic regions [82]. Foley et al. also applied HIFU to rabbit sciatic nerves. The US waves, with 3.2MHz frequency and 1930 W/cm^2 intensity, blocked nerve conduction and resulted in axonal degeneration [21]. Khraiche et al. observed an increase in spike frequency of primary hippocampal neurons upon exposure to high frequency bursts of US waves [83]. Tyler et al. investigated the effect of low intensity and low frequency US on mice hippocampal slice cultures and showed US's capability to excite neurons remotely and non-invasively [84]. Colluci et al. explored the effects of high and low frequency US waves on frog sciatic nerves and observed a decrease in action potential accompanied by an increase in temperature. Moreover, some of these effects were irreversible [85]. Tufail et al. applied transcranial pulsed US to rat hippocampal neurons and remotely stimulated neuronal activity without disrupting the BBB [86]. Yoo et al. neuromodulated rabbit activity using focused US waves without eliciting tissue damage or an immune response [87]. Min et al. subjected the rat brain to low frequency (690kHz), low intensity (130mW/cm^2) transcranial focused US after an epileptic seizure suppressing the number of epileptic bursts [40]. Yang et al. reduced extracellular GABA levels in rats when applying transcranial focused US stimulation of the thalamus [88]. Legon et al. showed that pulsed US can stimulate somatosensory circuits in humans [89]. Kim et al. were successful in stimulating abducens nerve using transcranial focused US [90]. King et al. explored different parameters for neuromodulation using focused US signals. Their study showed that US causes neuromodulation on the onset of the signals, whether continuous or pulsed, and

that stimulation success rates increases as a function of intensity and duration of stimulation [91]. Deffieux et al. showed that low intensity focused US are capable of modulating monkey visuomotor behavior [92]. Lipsman et al. were successful in reducing tremor in four patients using magnetic resonance focused ultrasound stimulation of the thalamus [24]. Menz et al. were successful in evoking visual potentials upon stimulating the retina with focused US of frequency 43 MHz [93]. Juan et al. were successful in inhibiting vagus nerve activity in rats due to exposure to focused pulsed US with a frequency of 1.1 MHz and intensity ranging from 13.6 to 93.4 W/cm^2 [94]. Kim et al. were successful in finding threshold intensities and sonication parameters for focused US brain stimulation by transcranially stimulating the somato-motor area of rats [95]. Lee et al. observed somatosensory sensations and evoked EEG potentials upon application of transcranial focused US to the human cortex [20]. King et al. showed promising effects when stimulating the rat motor cortex with US beams, and that these effects vary when different rostral and caudal regions are stimulated [96]. Legon et al. further applied transcranial focused US and managed to attenuate amplitudes of somatosensory evoked potentials [97], while Mueller et al. also used these signals to modulate intrinsic and evoked EEG phases and phase rates [98]. Kim et al. used pulsed focused US with several intensities to inhibit visually evoked potentials and concluded that applying different intensities to specific regions can have inhibitory and even excitatory effects [99]. Gulick et al. stimulated the rat motor cortex with an US signal of frequency 200kHz and intensity 100W/cm^2 and observed evoked hindlimb movement with variation in refractory periods when compared to electrical stimulation [100]. Han et al. studied the effect of Ketamine in inhibiting US-induced neuromodulation [101]. Li et al. fabricated an US transducer to stimulate freely moving rats and achieve effective neuromodulation [102]. Guo et al.

applied transcranial US to guinea pigs and observed activation of cortical and subcortical regions of the brain [103]. Xie et al. showed that cortico-muscular coupling can be altered using US stimulation with different numbers of tone bursts [104]. Lee et al. developed a head gear for transcranial focused US stimulation of the motor cortex of awake moving rats and observed changes in the actions of the rat [105]. Li et al. also fabricated a miniature head-mounted US transducer that was successful in inducing action potentials in situ and evoking head motion in the freely moving mouse [106]. Legon et al. applied US stimulation along with magnetic stimulation to the human motor cortex and showed that US inhibits single pulse motor evoked potentials, and attenuates intra-cortical facilitation [107]. Wang et al. applied transcranial ultrasound stimulation to mouse motor cortex with different parameters to modulate motor cortex oscillations (theta and gamma) and observed muscle contraction and motion in the mouse's tail. Their study showed that US intensity and stimulation duration are the dominating parameters in modulating these oscillations [108].

2.5. Ultrasound in Computational Models

The nervous system has always been viewed as an electrical system where each neuron represents a firing source. In 1952, Alan Hodgkin and Andrew Huxley developed a computational model that describes how an action potential in initiated and propagates in a single neuron. The Hodgkin and Huxley (HH) model is composed of electrical components that represent that dielectric neural membrane, the distribution of ions across this membrane, and the ion channels distributed throughout this membrane [109]. Electrical neuromodulation techniques are easily modeled and coupled to the HH model since they involve injection of electrical charges into neurons that are already modeled as

electrical components in the HH model. On the other hand, ultrasound is a purely mechanical stimulation modality. There is a huge body of literature that represent ultrasound as a successful stimulation modality, yet the mechanism of action of how and why this modality is successful remains unknown. There are several parameters that can be altered in ultrasound stimulation including intensity, frequency, sonication time, and pulse repetition frequency [91]. Incorporating these parameters into a mechanical model and coupling them to the HH electrical model remains a challenge until today. Jerusalim et al. developed a mechanical model that incorporates mechanical strain on axons to the electrophysiological responses of a neuron. The mechanical strain on the axon is represented via Maxwell's elastic spring and damper in series model. The mechanical component is coupled to the HH model [109]. Tian et al. developed an electro-mechanical model that studies the response of central neurons to mechanical stretching and plastic deformation. The model is composed of 3 main sub-models: (1) mechanical sub-model that relates mechanical forces to axonal deformation, (2) the mechanoelectrical coupling model that couples mechanical loading to electrophysiological changes, namely membrane capacitance and cell membrane area, and (3) the electrical HH model [110]. Finally, Lemaire et al. introduced a multi-scale optimized neuronal intramembrane cavitation (SONIC) model that accelerates computation and offers an increased interpretability to the effects of ultrasonic stimuli explaining how varying LIFUS parameters is reflected in spike amplitude and firing rates [111].

CHAPTER 3

AIMS

3.1. Aim #1

Build a biomechanical model for ultrasound effect on neural excitability

3.1.1. Hypotheses:

Hypothesis A: We investigate the impact of mechanical ultrasound forces, flexoelectric currents, and alternating membrane potential induced forces on ion channels

Hypothesis B: We test the hypothesis that mechanical ultrasound forces affect neural excitability

3.1.2. Challenge

Incorporate mechanical forces into the electrical Hodgkin and Huxley (HH) model

3.1.3. Approach

We model ultrasound signal propagation to reach a single neuron, modeled via the HH model, and induce mechanical tension forces on the ion channels and affect action potential generation and conduction.

3.1.4. Impact

Understand the mechanism of action of ultrasound stimulation and its effect on the neural membrane

3.2. Aim #2

Stimulation of the peripheral nervous system of the rat animal model using low intensity low frequency ultrasound stimulation to induce neuromodulation and suppression of pain

3.2.1. Hypotheses

Hypothesis A: We investigate the ability of an immersible ultrasound transducer to produce acoustic intensities for stimulating nerves at a low frequency range (300-700 kHz)

Hypothesis B: We test the hypothesis that ultrasound stimulation modulates the behavior of neural networks of the peripheral nervous system

3.2.2. Challenge

Explore the effect of each ultrasound parameter on the modulation and behavior of the neural networks involved in pain sensation

3.2.3. Approach

Ultrasound stimulation with different parameters (intensity and frequency) is applied on the rat animal model peripheral nervous system, mainly the sciatic nerve (reflex arc)

3.2.4. Impact

Investigate the impact of mechanical ultrasound stimulation on the reflex arc

CHAPTER 4

METHODS FOR COMPUTATIONAL MODEL

The mechanism of action of US stimulation, which is mechanical in nature, remains unknown especially since the nervous system is viewed as a pure electrical system. Therefore, in this section of the work, components of a biomechanical model are presented. The model incorporates mechanical effects of US stimulation on a single neuron membrane through incorporating membrane tension, ion channels and ion specific transmembrane proteins, and the flexoelectric effect of the neural membrane, and coupling them to the electrical Hodgkin and Huxley model (HH). The model focuses on low intensity low frequency US stimulation applied on a single neuron.

4.1 Biomechanical Forces

4.1.1 Membrane forces

The first component of the model deals with the lipid membrane and the external mechanical force acting on it during US stimulation. The mechanical waves exert pressure on the membrane. The pressure applied induces tension in the membrane of the neuron [112]. The amount of lateral tension produced is a function of the applied pressure and the length of the neuron subject to this force. Equation 4.1 estimates the value of the tension.

Equations 4.1: $\psi = PL$

In equation 4.1, P is the pressure in Pascal (P), ψ is the lateral tension in Newton per meter (N/m) and L is the length of neuron subjected to tension in meters (m).

The US transducer was modeled with several elements; the area of each element is assumed to be greater than the area of the neural membrane.

In addition to externally applied US force, tension also rises internally from variation in the membrane potential. The capacitive nature of the lipid membrane results in a charge accumulation that impacts ionic concentrations on both sides of the membrane. As the potential varies, tension rises on each side of the membrane as a function of the charge mobility. Therefore, the internally induced total tension is the sum of tension on both sides and the pre-existing voltage-independent tension [113, 114]. The force is governed by equation 4.2.

Equations 4.2:
$$\frac{(\gamma - \gamma^0)e_0}{\sqrt{(2k_B T)^2 \epsilon_w \epsilon_0}} =$$
$$\sqrt{n_{ex}}\left[\sinh^{-1}\left(\frac{\sigma_{ex} - C_m V}{2\sqrt{2n_{ex}k_B T\epsilon_w\epsilon_0}}\right)\right]^2 + \sqrt{n_{in}}\left[\sinh^{-1}\left(\frac{\sigma_{in} - C_m V}{2\sqrt{2n_{in}k_B T\epsilon_w\epsilon_0}}\right)\right]^2$$

γ is the total internally produced tension, γ^0 is the total surface tension in the absence of electric field, e_0 is the electronic charge, ϵ_0 and ϵ_w are the permittivity of free space and water respectively, C_m is the interface capacitance, V is the induced potential, T is the absolute temperature in kelvin, k_B is Boltzmann's constant, n is the ionic strength of the solution, σ is the structural charge density, and the subscripts ex and in represent the external and internal membrane interfaces.

4.1.2 Ion Channel Conductance

In this component, we model the impact of the total tension in the neural membrane on the conductance of ion channels. Ion channels have intrinsic energy levels that rise from isomerization processes and control the opening and closing of the channels. As the US is applied, inducing tension in the membrane, this energy is altered proportionally to the amount of applied tension. Thus, we combine the external tension induced by the mechanical US stimulation and the internal tension induced by the membrane voltage to alter the intrinsic energy difference ΔG according to equation 4.3 [112, 113].

Equation 4.3: $\Delta G_{mech\ tension} = -\chi \Delta a + \Delta u$

Where χ is the total tension from equations 4.1 and 4.2, Δa is the change in the area of the ion channel after opening, and Δu is the intrinsic energy difference between states in the absence of tension [113]. Δu presents the energy that rises from the transition between open and closed states of isomer conformations of ion channel proteins [115]. In equation 4.3, the change in the area of an ion channel upon opening is assumed to be 50% of the total ion channel area. The intrinsic energy difference influences ligand and voltage gated ion channel activity that is reflected by the change in the probability of the channel being open governed by equation 4.4.

Equation 4.4: $P_O = \dfrac{1}{1 + e^{\left(\frac{\Delta G}{k_b T}\right)}}$

P_O is the probability of the channel being open, T is the absolute temperature in kelvin, and k_b is Boltzmann's constant [113].

4.1.3 Flexo-electric Currents

The dielectric nature of the neural membrane gives rise to the flexoelectric effect where strain gradient leads to spontaneous electrical polarization. The induced flexoelectric current can be expressed by the following equation (4.5) [113, 114]:

Equation 4.5: $I_\omega = f \dfrac{C_0}{\varepsilon_0} 2 c_m \omega$

f is the flexoelectric coefficient in coulombs, ε_0 is the absolute dielectric permittivity of free space, c_m is the maximal curvature, C_0 is the membrane capacitance, and ω is the angular frequency.

This current depends on the flexoelectric voltage induced in equation 4.6 and on the membrane capacitance of equation 4.7.

Equation 4.6: $U_\omega = \dfrac{f}{\varepsilon_0} 2 c_m$

Equation 4.7: $C_0 = \frac{\varepsilon_0 S_0}{d}$

f is the flexoelectric coefficient in coulombs, ε_0 is the absolute dielectric permittivity of free space, S_0 is the flat membrane area, and c_m is the maximal curvature.

4.2 Biomechanical Forces and Neural Excitability

To test the effect of mechanical transduction and US stimulation, the flexoelectric current and the tension were applied to a neuron placed near the US transducer. The flexoelectric current and the probability change that resulted from the tension and intrinsic energy were incorporated into the Hodgkin-Huxley (HH) model. The HH model represents the neural membrane as a capacitive component in parallel with conductive components representing the permeability of the membrane to a flow of sodium (Na+), potassium (K+), and chloride (Cl-) currents that govern the membrane potential [116]. Figure 4.1 shows the HH model components.
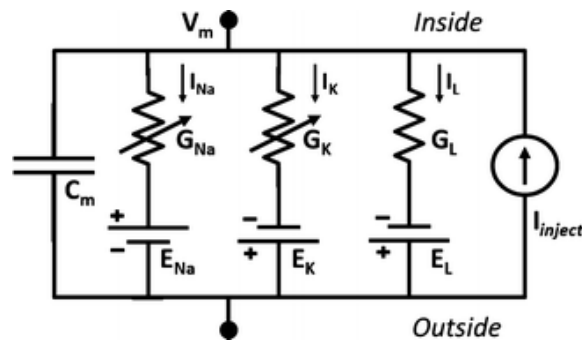
Figure 4.1: HH model components

The latter concept is at the basis of HH's differential equation 4.8 for the computation of the membrane potential.

Equation 4.8: $A \frac{\partial^2 V}{\partial x^2} = B \frac{\partial V}{\partial t} + CV + D$

Parameters governing equation 4.8 are:

Equation 4.9: $A = \frac{\pi d_0^2}{4 \rho a}$

18

Equation 4.10: $B = \frac{C_m \pi d_0}{h_0}$

Equation 4.11: $C = \frac{\pi d_0}{h_0}(G_L + G_{Na} + G_K)$

Equation 4.12: $D = \frac{\pi d_0}{h_0}(G_L E_L + G_{Na} E_{Na} + G_K E_K)$

The constants in the above equations are specified in table 4.1. Knowing that Na+ channels have an activation gate (m) and an inactivation gate (h) while K+ channels only have an activation gate (n), the conductance components G_{Na} and G_K are based on the gating variables m, n, and h as seen in equations 4.13 and 4.14. These gating variables are both voltage and time dependent. According to HH, the probability of each ion channel to be open is equal to the probability of the gates of the ion channel being open, raised to the number of gates.

Table 4.1: Constants used in the model

Symbol	Constant	Value	ref
γ^0	Surface tension if no electric field	16×10^{-12}	[116]
e^0	Electronic charge	$1.60217662 \times 10^{-19}$	-
$\in_0$	Permittivity of free space	$8.85418782 \times 10^{-12}$	-
$\in_w$	Permittivity of water	80.1	-
C_m	Interface capacitance	3.6×10^{-19}	-
T	Absolute temperature in kelvin	307.95	-
k_B	Boltzmann's constant	$1.38064852 \times 10^{-23}$	-
n_{ex}	Ionic strength of the solution external	15.8×10^{-3}	[117]
n_{in}	Ionic strength of the solution internal	154.1004×10^{-3}	[117]
σ_{ex}	Structural charge density external	-5×10^{-3}	[118]
σ_{in}	Structural charge density internal	-18×10^{-3}	[118]
f	Flexoelectric coefficient in coulombs	2.5×10^{19}	-
S_o	Flat membrane area	302400×10^{-18}	-
c_m	Maximal curvature	$(1/0.7) \times 10^6$	[119]
d	Membrane capacitive thickness	10×10^{-9}	[120]
G_k	Conductance of potassium ion channel	36	[116]
G_{Na}	Conductance of sodium ion channel	120	[116]
G_L	Conductance of chloride ion channel	0.3	[116]
E_K	Nernst potential of potassium	-12	[116]
E_{Na}	Nernst potential of sodium	115	[116]
E_L	Nernst potential of chloride	10.613	[116]
Δu	Intrinsic energy-no tension	6.0286×10^{-20}	[115]

Equations of HH:

Equation 4.13: $G_{Na}(V) = \overline{G_{Na}}m^3h$

Equation 4.14: $G_K(V) = \overline{G_K}m^4$

Equation 4.15: $\frac{dm}{dt} = \alpha_m(V)(1-m) - \beta_m(V)m$

Equation 4.16: $\frac{dn}{dt} = \alpha_n(V)(1-n) - \beta_n(V)n$

Equation 4.17: $\frac{dh}{dt} = \alpha_h(V)(1-h) - \beta_h(V)h$

Equation 4.18: $\alpha_m(V) = \frac{25-(V-V_{rest})}{10(e^{\frac{25-(V-V_{rest})}{10}}-1)}$

Equation 4.19: $\alpha_n(V) = \frac{25-(V-V_{rest})}{100(e^{\frac{25-(V-V_{rest})}{10}}-1)}$

Equation 4.20: $\alpha_h(V) = 0.07e^{-(V-V_{rest})/20}$

Equation 4.21: $\beta_m(V) = 4e^{-(V-V_{rest})/18}$

Equation 4.22: $\beta_n(V) = 0.125e^{-(V-V_{rest})/80}$

Equation 4.23: $\beta_h(V) = \frac{1}{e^{\frac{30-(V-V_{rest})}{10}}+1}$

The HH model for neural membrane firing lacks the mechanical components discussed within this work. Knowing that all voltage, time, and tension dependencies of the conductance components are to be considered, we propose the following:

Let $P(A \cap B) = P(A).P(B)$ where A and B are two distinct events. A is the opening of ion channels due to the gating variables as discussed by HH while B is the opening of ion channels due to the applied tension explained in component 2 of our work. Since the opening of ion channels depends on both tension and gating variables, the probability of each ion channel to be open is finally given by $(A \cap B)$. In cases such as that of Cl⁻ channels where gating variables do not exist, P(A) is equal to 1. The mechanical

stimulation and transduction affect the conductance as described by the following equations:

Equation 4.24: $G_{Na}(V) = \overline{G_{Na}} \times P(A) \times P(B) = \overline{G_{Na}} \times m^3 h \times P_0$

Equation 4.25: $G_K(V) = \overline{G_k} \times P(A) \times P(B) = \overline{G_K} \times n^4 \times P_0$

Equation 4.26: $G_L(V) = \overline{G_L} \times P(B) = \overline{G_L} \times P_0$

4.3 Model Implementation

The model was implemented using MATLAB.

4.3.1 US transducer

The US transducer was modeled via an acoustic toolbox in MATLAB entitled: "k-wave", which solves time domain acoustic and ultrasound simulations in complex and tissue-realistic media, using the k-space pseudo spectral method.

In MATLAB k-wave the followed was implemented:

1. Define a 2D grid (64×64)

2. Define time explicitly with a step size of 0.2μsecs

3. Define the medium of propagation using medium density and speed of sound

4. Define a time varying force source where US signals propagate in the x-direction inside the grid

5. Add a perfectly matching layer (PML) to absorb US signals at the edge of the grid and avoid their reflection

6. Add input signal as acoustic pressure (AP) in pascal (Pa)

7. Convert input signal from AP to particle velocity (PV) in m/sec using the formula $PV = \dfrac{AP}{\text{acoustic impedance}} = \dfrac{AP}{density \times speed\ of\ sound} = \dfrac{AP}{\rho V}$

8. Add sensor to measure the pressure and acoustic intensity

9. Run the simulation

10. Detect maximum intensity pixel in the grid

11. Compute the pressure at this point

4.3.2 Biomechanical model components

The HH electrical model equations are incorporated into MATLAB. Since we are studying the US effect on a naturally firing neuron, we injected the minimum current to excite the neuron into the HH model. The flexo-electric current was also added to the injected current. This current injection caused changes in the membrane voltage which induced membrane tension. On the other hand, pressure from the US simulation was transformed into tension, added to the membrane voltage induced tension, and both tensions affected the free energy. Finally, the effect of energy change was incorporated into the probabilities of the ions channels as discussed in the previous sections. It is important to mention that the model runs in loops, the change in membrane voltage causes tension and tension itself affects membrane voltage again. Figure 4.2 shows a flow chart of the model.

4.4 Parameters

The parameters that the modeled explored are:

1. *US frequency*: 250-750 kHz with step frequency 50 kHz

2. *US acoustic pressure*: 50 kPa to 10 MPa with step size 50 kPa

3. *US mode*: continuous and pulsed stimulation

4.5 Model Outputs

The following outcomes are observed in the model:

1. *Maximum and minimum membrane voltages*

2. *Action Potential (AP):* amplitude between V_{max} and V_{min}

3. *Acoustic intensity:* the intensity of the US signal that stimulates the HH model (a section of the neuron) (*W/cm²*)

4. *Firing rates:* the number of spikes observed in a second *(Hz)*

5. *Latency:* the time between the stimulation and the response *(ms)*

6. *Inter-spike interval (ISI)*: the time between subsequent spikes (*ms*)
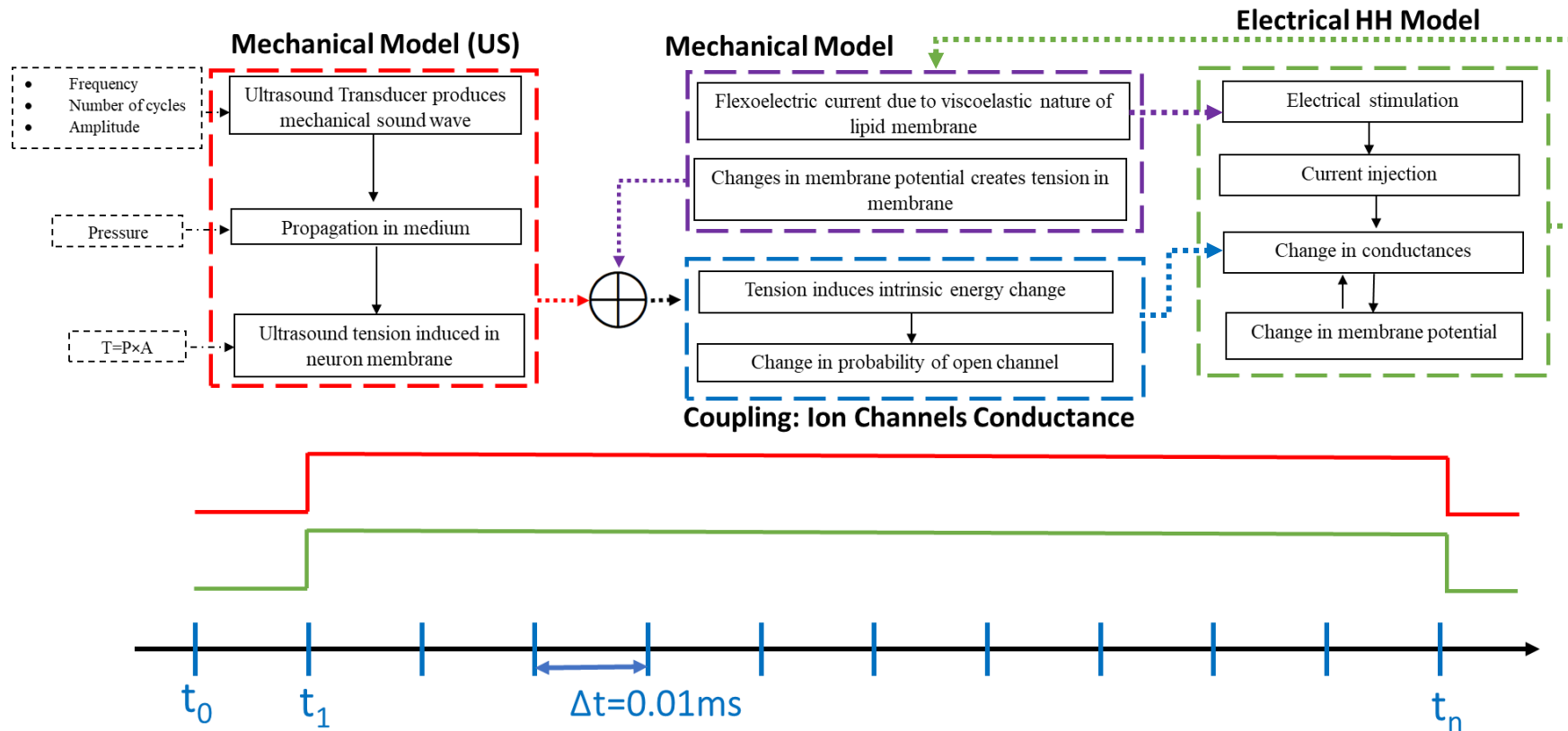
Figure 4.2: Model flow Diagram: The model simulates ultrasound waves propagating in US gel medium and inducing pressure on neurons in this medium (red box). The pressure results in tension in the neuron membrane, which when added to the tension induced from membrane voltage fluctuation and flexoelectric currents (purple box), causing changing in intrinsic energy and the probability of ion channels being open (blue box). The change in ion channel state affect the HH model through altering conductances and therefore membrane potentials (green box).

CHAPTER 5

RESULTS FOR COMPUTATIONAL MODEL

5.1 Action Potential of a Naturally Firing Neuron (No US)

The results of the effect of US stimulation on the neural excitability were compared to a naturally firing neuron with no US stimulation. Figure 5.1 shows the variation action potential and the gating variable m, n, and h for a naturally firing neuron. The membrane voltage fluctuated between -88 and 24 mV with the amplitude of the action potential around 112 mV, the firing rate around 53.2 Hz, and an ISI of around 18.8 ms.
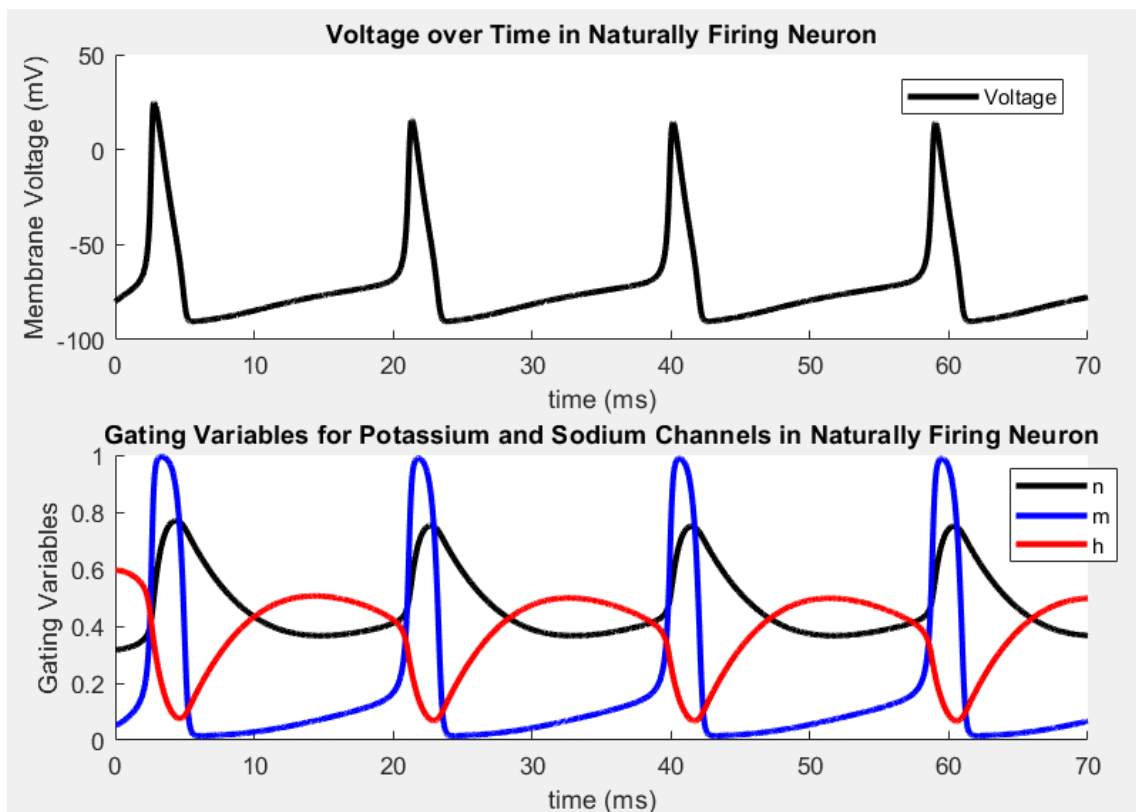
Figure 5.1: Action Potential and gating variables of a naturally firing neuron (No US): The membrane potential of a naturally firing neuron varies between -99 and 24 mV as shown in the top figure where the time between spies is around 18.8 ms. The below figure shows the gating variables m (blue), n (black), and h (red) which represent the probabilities of sodium channel activation, potassium channel activation, and sodium channel inactivation and fluctuate between 0 and 1.

5.2 Effect of US stimulation on a Single Firing Neuron

The US model simulated 4,400 cases of US stimulation as mentioned in section 4.4.

5.2.1 US stimulation Acoustic Intensities

The distribution of acoustic intensities varied as a function of acoustic medium impedance, frequency, and input impedance. The acoustic impedance is related to the medium properties. The chosen medium was coupling US gel. Figures 5.2 and 5.3 show the variation of the maximum acoustic intensity observed as a function of input acoustic pressure and input frequency respectively.

The simulations show that as the acoustic input pressure increased, higher acoustic intensities were observed, ranging from 0 to around 300 W/cm^2. Figure 5.2 shows that the same increasing pattern was observed with all frequencies. It also shows that the range of the intensities dropped to zero to 150 W/cm^2 as the US mode is switched from continuous to pulsed. Figures 5.2 and 5.3 also show that as the US frequency increased from 250 to 500 kHz, the acoustic intensity dropped. The intensities then increased at 550 kHz and then dropped again. Most US modulation intensities fall in a range below 10 W/cm^2. That being said, and looking to figure 5.4, we can limit the range of US acoustic pressure between zero and 3.5 MPa for continuous stimulation mode, and zero to around 5 MPa for the pulsed mode for all the frequencies between 250 kHz and 750 kHz.

5.2.2 Action Potential Amplitude

US stimulation caused a change in membrane potential and action potential. Action potential amplitudes dropped from around 110 mV to ranges between 80 and 100 mV for continuous US stimulation and 66 to 74 mV for pulsed stimulation (Figure 5.5). Figure 5.5 shows that lower intensities, at all frequencies, cause a greater decrease in AP amplitudes. Moreover, figure 5.6 shows that in continuous stimulation, 99.5 % of the

simulations showed a 20% drop in AP amplitude, while in the pulsed simulations, 99 % showed a drop between 20 and 40 % in AP. Therefore, results showed that first, pulsed stimulation was more successful in suppressing AP and in modulation of a single neuron firing; and second, lower acoustic intensities were more successful in suppressing AP amplitudes.

5.2.3 Firing Rate

US stimulation increased firing rates. Pulsed US stimulation increased firing rates from around 53 Hz to a range between 70 and 76 Hz, with most rates falling between 70 and 71 Hz and few between 75 and 76 Hz as figure 5.7 shows. Moreover, as frequency increased, firing rates tend to increase. Figure 5.8 shows the distribution of firing rates at each frequency. The lower blue region represents intensities whose firing rates are between 75 and 76 Hz, while the upper orange region represents intensities with firing rates between 70 and 71 Hz. The line separating between the two regions shows the intensities separating between the two rates at each frequency.

Continuous stimulation increased firing rates to a range between 65 and 76 Hz, with 98.5% of the simulations with firing rates between 65 and 70 Hz as table 5.1 shows.

Table 5.1: Distribution of firing rate for continuous US stimulation

Frequency	Firing Rate %	
	[65-70]	[70-76]
250	97.5	2.5
300	99.5	0.5
350		
400		
600		
450	98.5	99.5
550		
650		
700		
750		

Both stimulation modes showed that lower US intensities had a larger impact on neural excitability since they had a greater magnitude of change on firing rates.

5.2.4 ISI & Latency

US stimulation had a slight effect on ISI and latency. ISI dropped from around 18.8 ms to around 15 ms for continuous stimulation and around 14 ms for pulsed stimulation. On the other hand, latency changed from around 20 ms to around 18.5 ms for continuous stimulation and 18.4 ms for pulsed. Results show that US stimulation had a higher impact on firing rates and AP amplitude than it affected latency and ISI.
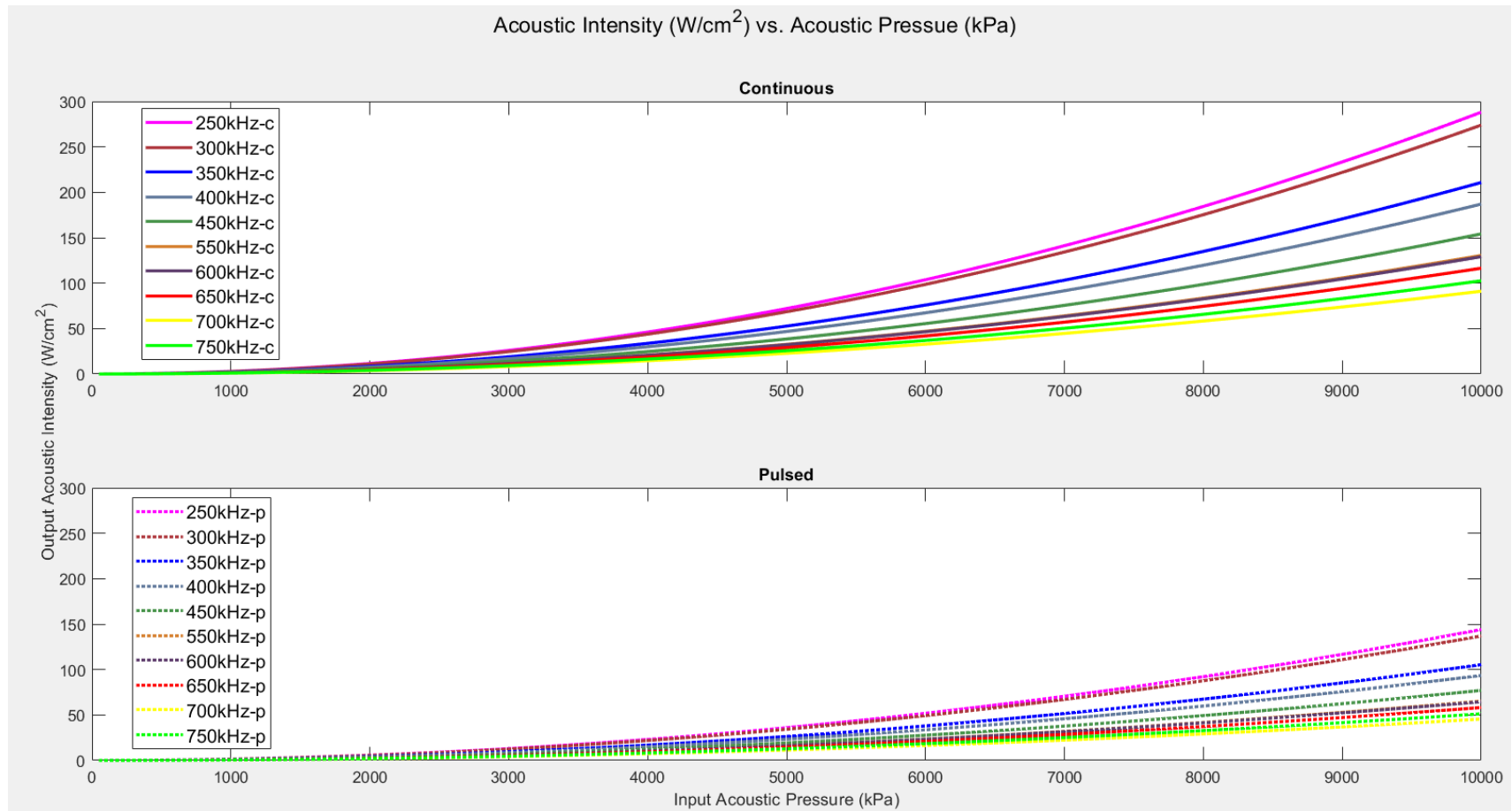
Figure 5.2: Variation of Acoustic Intensity as a function of Input Acoustic Pressure: The maximum acoustic intensity generated in the medium increases as the input acoustic pressure increases. This increase is observed among all frequencies. As the US frequency and the output acoustic intensity are inversely proportional which is shown since higher frequencies (650 (red), 700 (yellow), and 750 kHz (green)) are smaller than lower frequencies (250 (magenta), 300 *brown) and 350 kHz (navy blue)). Continuous US stimulation (top) can produce higher intensities than pulsed stimulation (bottom).
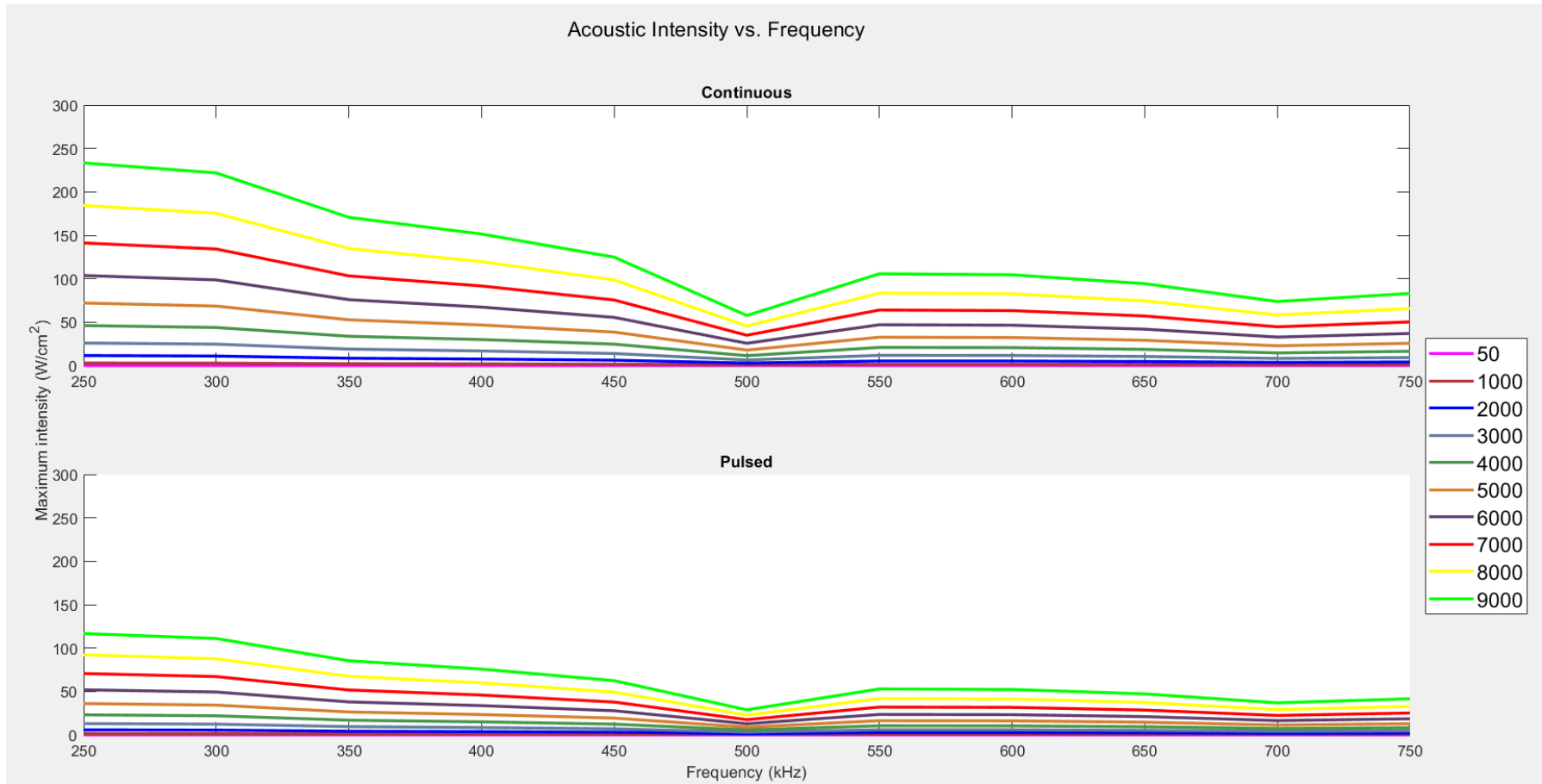
Figure 5.3: Variation of Acoustic Intensity as a function of US input Frequency: Acoustic intensity is inversely proportional to US stimulation frequency, with continuous stimulation (top) carrying higher acoustic intensities than pulsed (bottom). Each line represents different input acoustic pressure, which as it increases the output acoustic intensity increases.
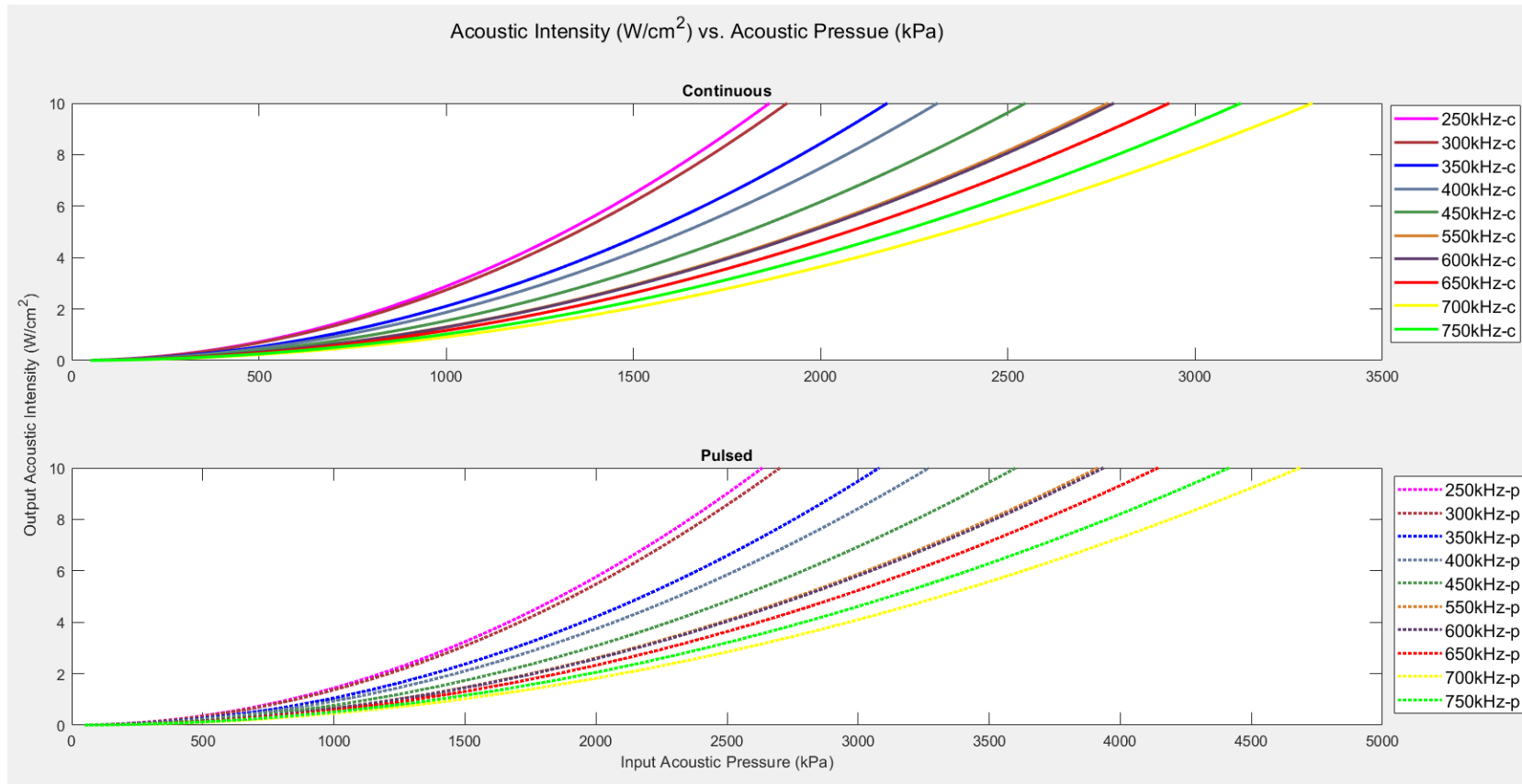
Figure 5.4: Acoustic Intensity (limited to 10 W/cm2) vs. Acoustic Pressure: The maximum acoustic intensity generated in the medium increases as the input acoustic pressure increases. This increase is observed among all frequencies. As the US frequency and the output acoustic intensity are inversely proportional which is shown since higher frequencies (650 (red), 700 (yellow), and 750 kHz (green)) are smaller than lower frequencies (250 (magenta), 300 *brown) and 350 kHz (navy blue)). Continuous US stimulation (top) can produce higher intensities than pulsed stimulation (bottom).

31
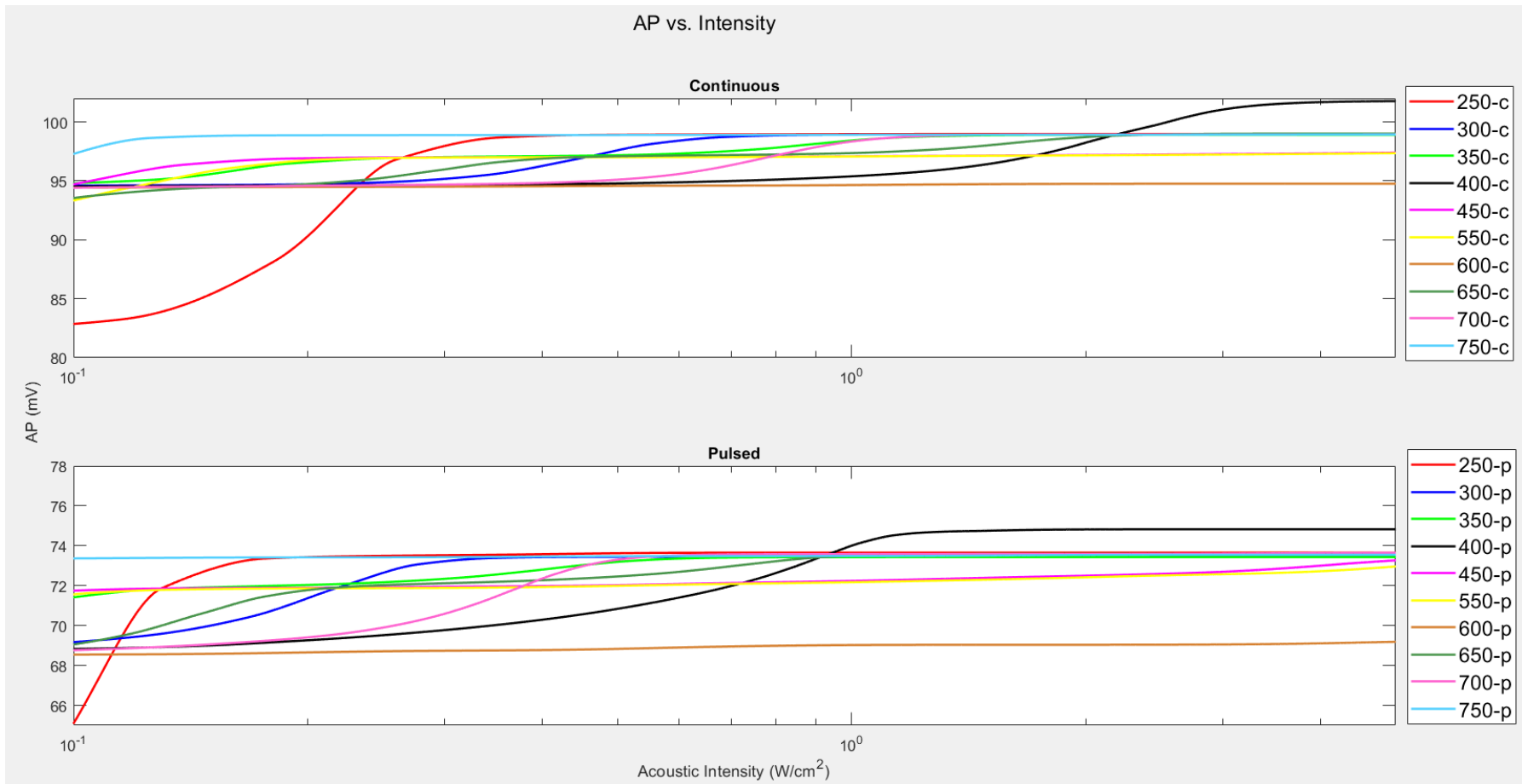
Figure 5.5: Variation of Action Potentials Amplitude as a function of Acoustic Intensity (W/cm^2) and Frequency: The AP amplitude is altered upon US stimulation. Continuous US stimulation (top) causes a drop in AP from 112 mV to between 80 and 100 mV with lower frequencies causing higher suppression of AP (250 kHz causes highest drop- red line plot). Pulsed US stimulation (bottom) causes further suppression of AP amplitudes to below 74 mV, also with lower frequencies having greater impact.

32
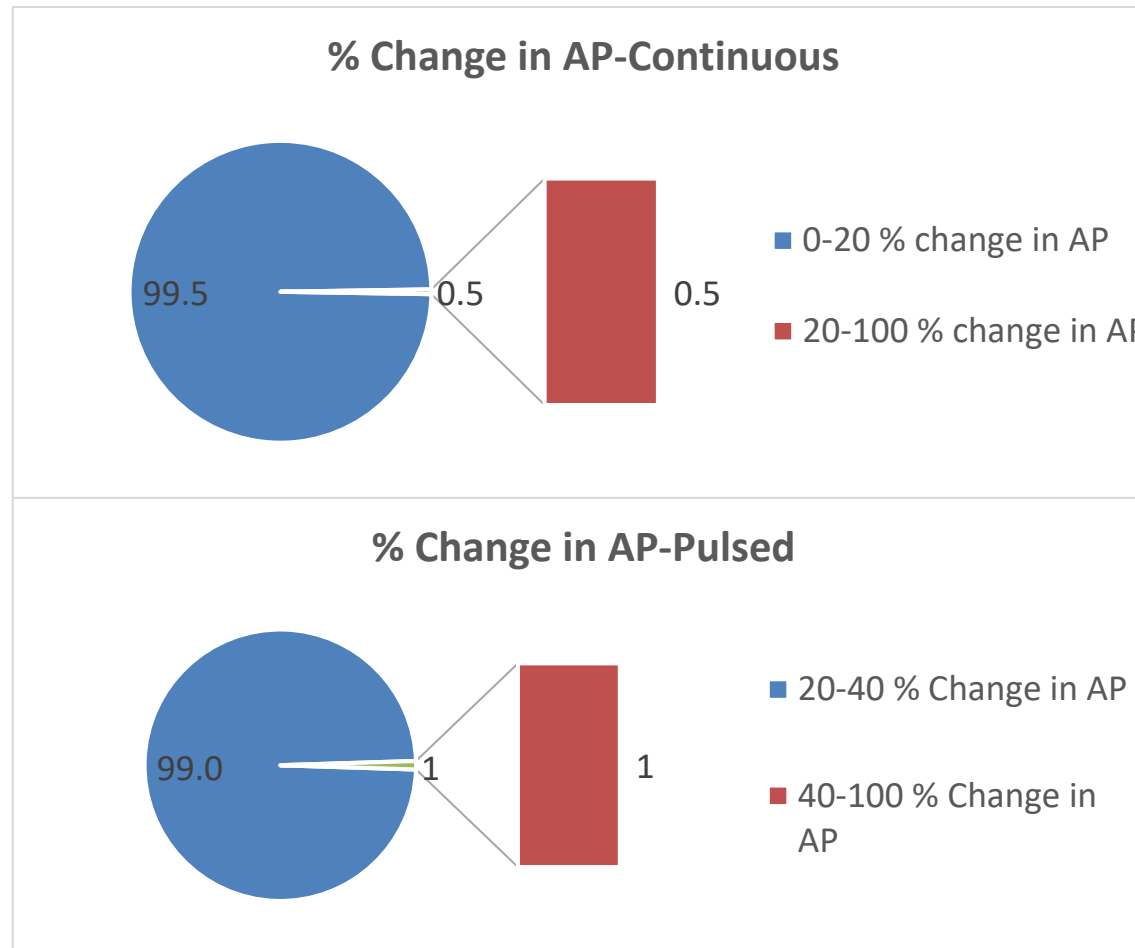
Figure 5.6: Distribution of AP percentage change for Pulsed and Continuous US stimulation: In continuous stimulation, 99.5 % of the simulations showed a 20% drop in AP amplitude (top), while in the pulsed simulations, 99 % showed a drop between 20 and 40 % in AP (bottom). Pulsed US stimulation caused greater suppression of neural firing.
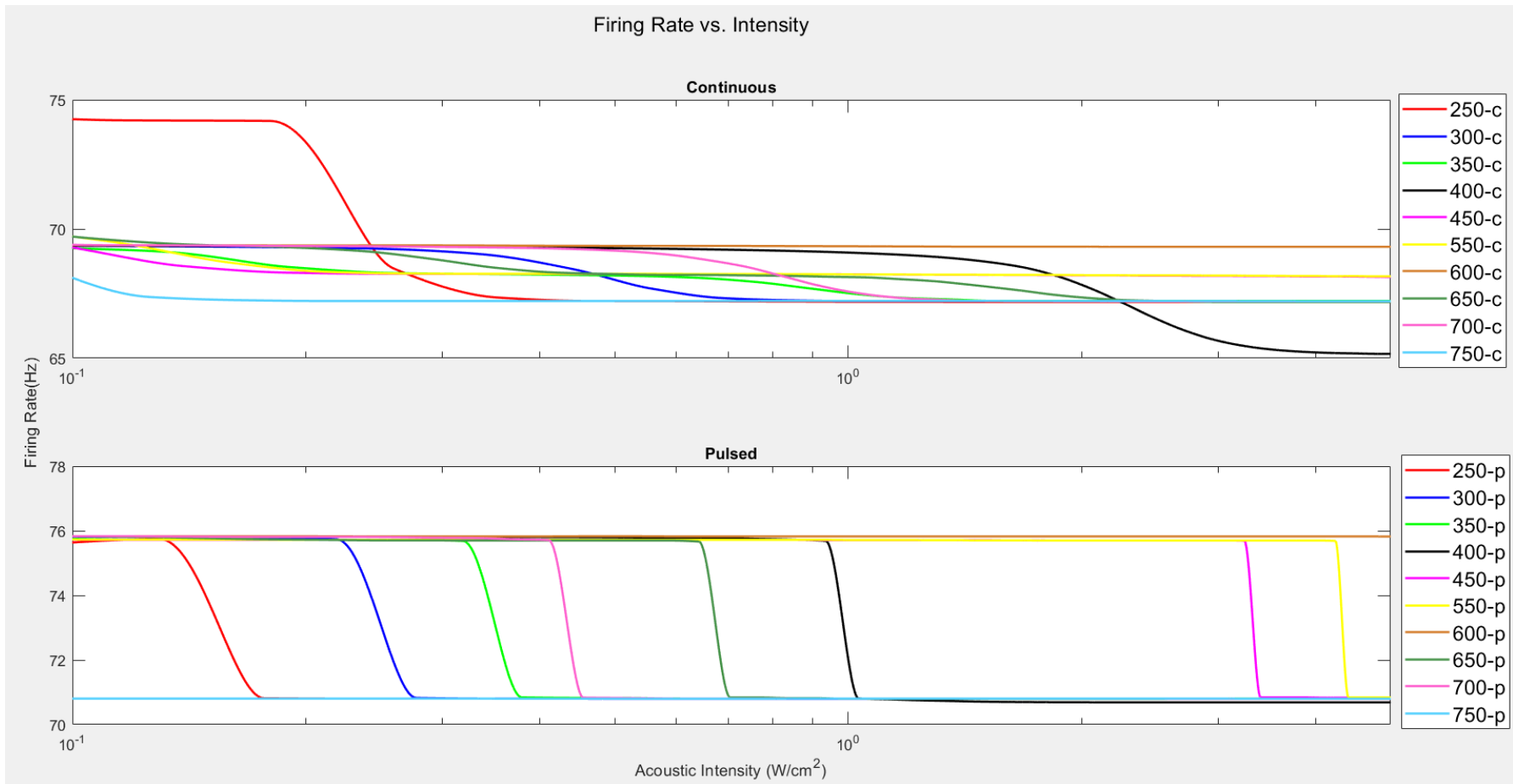
Figure 5.7: Variation of Firing rate as a function of Acoustic Intensity (W/cm2) and US stimulation Frequency: Continuous US stimulation increased firing rates from around 53 Hz to a range between 65 and 75 Hz (top), while pulsed US stimulation increased firing rates to a range between 70 and 76 Hz, with most rates falling between 70 and 71 Hz and few between 75 and 76 Hz (bottom). As frequency increased, firing rates tend to increase.
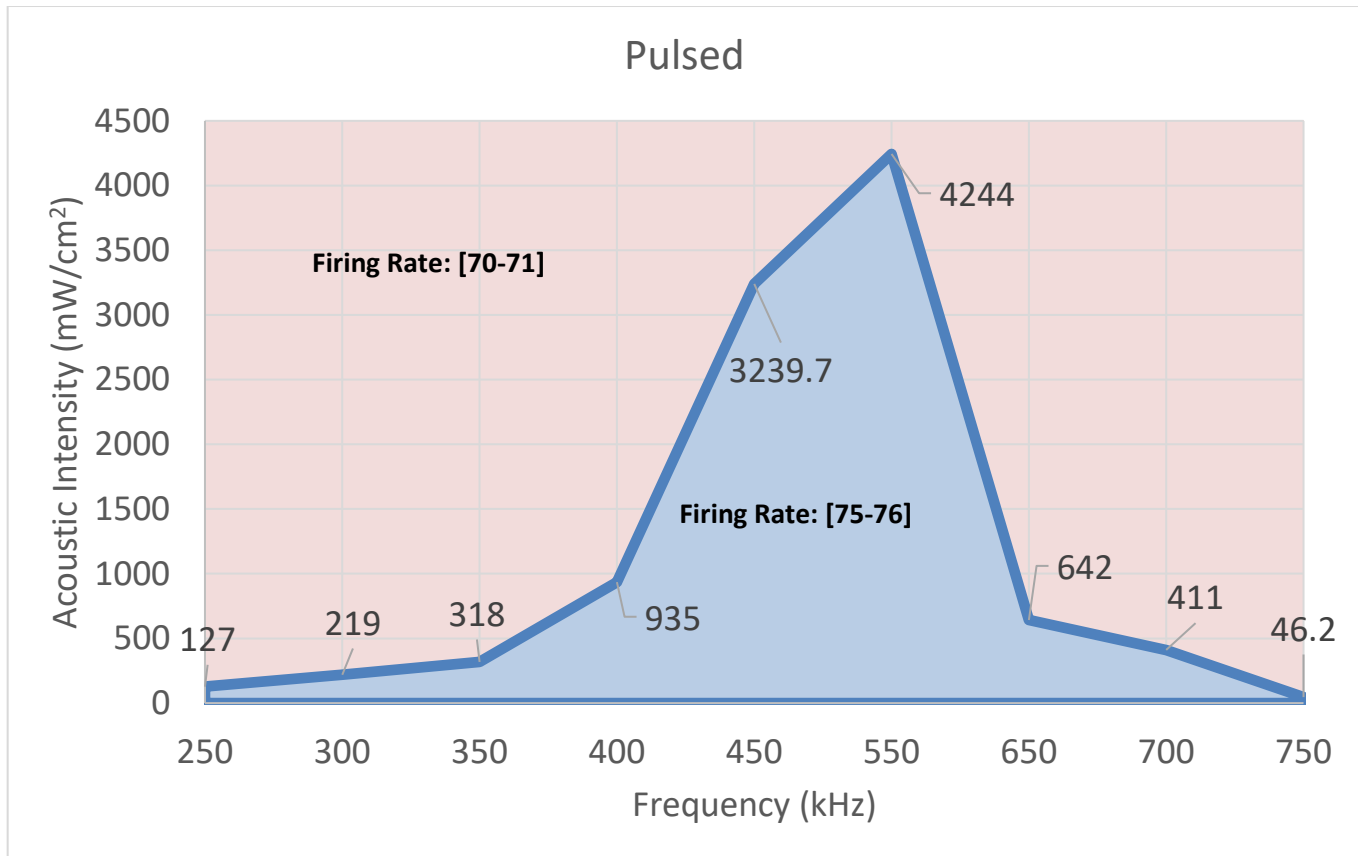
Figure 5.8: Distribution of firing rates at each US frequency (Pulsed Stimulation): The lower blue region represents intensities whose firing rates are between 75 and 76 Hz, while the upper orange region represents intensities with firing rates between 70 and 71 Hz. The line separating between the two regions shows the intensities separating between the two rates at each frequency.

CHAPTER 6

DISCUSSION FOR COMPUTATIONAL MODEL

In recent studies, ultrasound technology succeeded as a stimulation modality to excite and inhibit neural pathways, modulate neural functions, or even induce activity in silent networks[79, 83, 86, 91, 95, 121]. The promise that this modality offers as a non-invasive stimulation method, that travels through tissues without triggering immune responses or toxic byproducts, calls for further investigations to understand and predict the mechanisms involved in US stimulation.

The major effects of US stimulation are thermal [31, 37], mechanical, or cavitation effects [122, 123]. Thermal effects appear only at high intensities and cavitation was eliminated by histological analysis confirming no gas bubbles in targeted tissue and their surroundings [124, 125]. US waves are capable of displacing small ions, molecules, and organelles or inducing movement of the fluid along and around cell membranes [126]. These mechanical effects can result in mechanical stress in the neural membrane and modulate mechano-sensitive transmembrane proteins and ion channel behaviors [112, 121, 126, 127]. Therefore, we developed a model in an attempt to simulate the effects of US stimulation on neural membrane potential and subsequent activity of a single neuron.

The model incorporated membrane tension, ion channels and ion specific transmembrane proteins, and the flexoelectric effect of the neural membrane and coupled these mechanical components to a typical HH model of a firing neuron via ion channel probabilities. We explored the impact of US parameters of intensity and frequency on neuronal excitability through the HH model.

The model was successful in predicting modulation of neural activity. US stimulation, continuous and pulsed, was effective in suppressing action potential

amplitudes and modulating firing rates. On the other hand, US stimulation had minimal effect on ISI and latency. The model also showed higher success rates and modulation effects with lower frequencies and intensities which agrees with results obtained in our animal experiments.

The novelty of the biomechanical model that lies in incorporating mechanical forces to the electrical HH model makes it difficult to compare our results to computational models in literature, yet, there is a huge body of literature on experimental studies. The modulation of neural behavior due to US stimulation reflected in a suppression of action potential amplitude is a common result [95, 99, 128, 129]. Moreover, the higher success of lower frequencies and intensities is also observed in several experiments [91, 95] including our work in the rat animal model and could be explained by the natural behavior of higher frequency US waves in tissue that tend to diffract more than lower frequencies causing a reduction in their impact.

CHAPTER 7

METHODS FOR ANIMAL MODEL

7.1. Characterizing the Ultrasound Transducer

Ultrasound transducers receive electrical signals and transmit mechanical signals that can travel in tissue and in fluids. The mechanical signals are quantized by measuring the acoustic intensity (W/cm^2) they produce. Characterization of the immersible transducer is required to find the distribution and magnitude of the acoustic intensity that is needed to modulate neural networks. The mechanical signal produced by the US transducer is acquired via a hydrophone- a device that changes mechanical signals to electrical signals- and processed. The required setup consists of the following:

1. A waveform generator to produce an electrical signal with determined parameters

2. A radio frequency (RF) amplifier to amplify the electrical signal since high voltages are required to operate the US transducer and the waveform generator is limited to 10V at 50Ω output impedance

3. An impedance matching circuit to reduce the impedance mismatch between the amplifier and the US transducer's input impedance

4. An immersible US transducer

5. A water bath to provide a suitable medium for the propagation of US signals

6. A hydrophone to collect produced mechanical signals

7. Motorized axes to mount the hydrophone and program it to scan specific geometric volumes around the US transducer

8. A data acquisition system

9. A PC for data processing and creating acoustic profiles

Figure 7.1 describes the required setup and its connections. The Rf amplifier receives a signal from the waveform generator, amplifies it, and sends it to the US transducer through the matching circuit. The US transducer produces mechanical waves that are transformed back to electrical signals and relayed to the DAQ board. The PC receives and post-processes acquired data and controls the motion of the hydrophone by controlling the 3-axes motorized system.
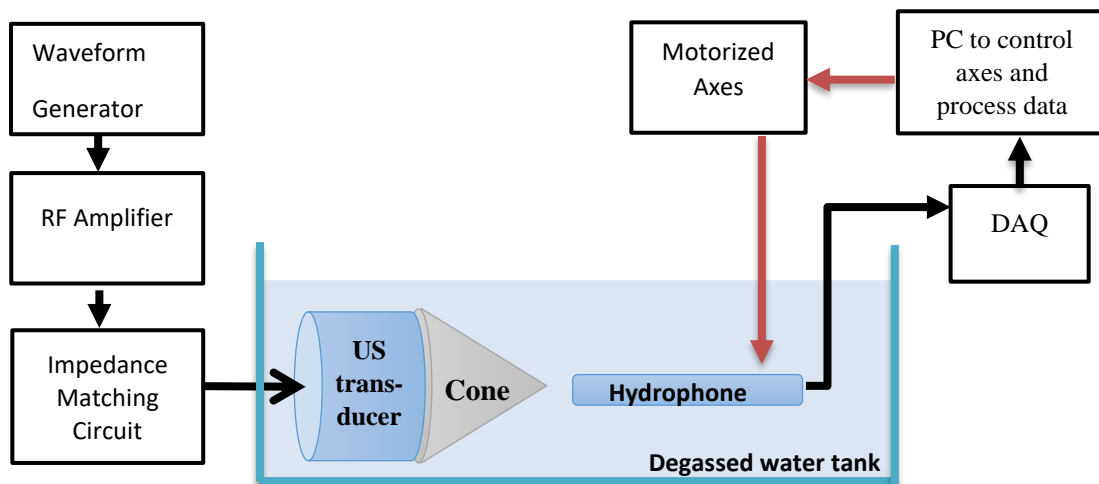
Figure 7.1: Schematic Diagram of Experimental Setup

7.1.1 Impedance Matching Circuit

To supply the US transducer with electric power, the waveform generator will be set to a continuous sine wave with frequencies 200, 500, and 700 kHz, output voltage 0.5Vpp, and output impedance 50Ω. We chose 200, 500, and 700 kHz for two reasons; first we tend to explore neuromodulation at low frequencies (less than 1MHz), and second since the immersible US transducer has a center frequency 1MHz and a frequency response that spans these frequencies. The output voltage should be strictly less than 1 Vpp since RF amplifiers require low input voltages else the "Gain Compression Phenomena" will occur causing distortion and attenuation in its output signal.

The output impedance of the RF amplifier is fixed to 50Ω. On the other hand, the US transducer is composed from piezo material whose response is frequency dependent. The input impedance of the transducer is therefore frequency dependent and is in mismatch with that of the RF amplifier. This mismatch will cause a reflection of the input signal to the transducer which, if not addressed, might damage the RF amplifier and the waveform generator.

7.1.1.1 Measuring Impedance Using RLC meter

The impedance of the transducer was measured at frequencies of 200, 500, and 700 kHz using an RLC meter. Figure 7.2.a and 7.2.b show plots for the impedance magnitude and phase between frequencies 100 kHz and 1MHz.
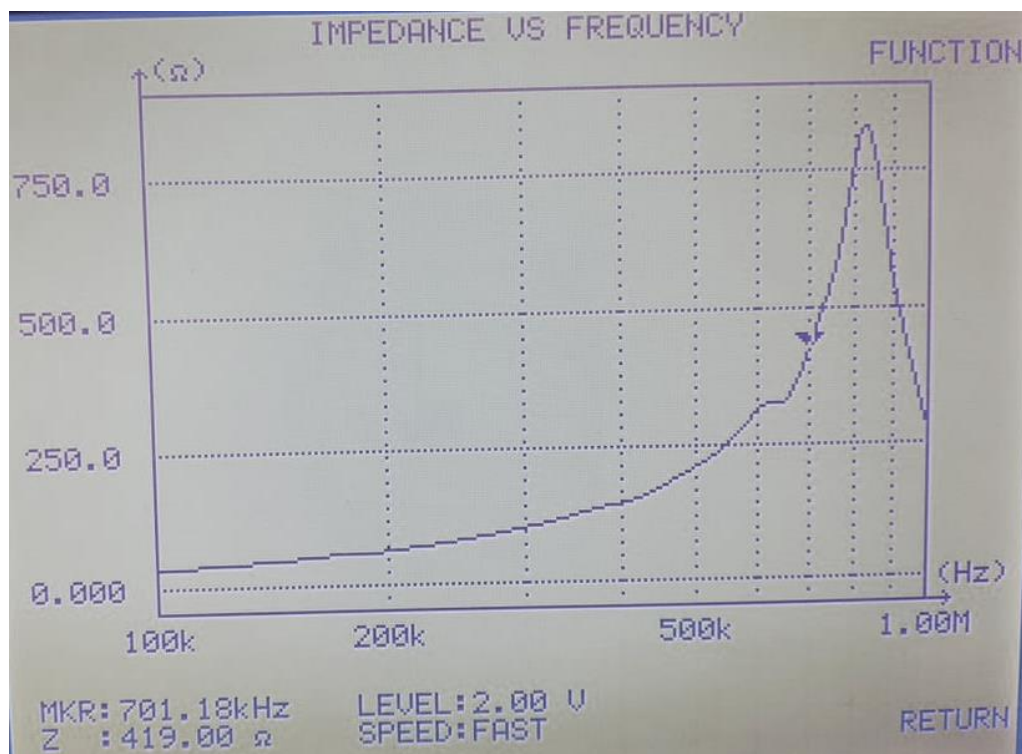
Figure 7.2.a. Plot representing variation of Impedance magnitude of the US transducer as a function of frequency
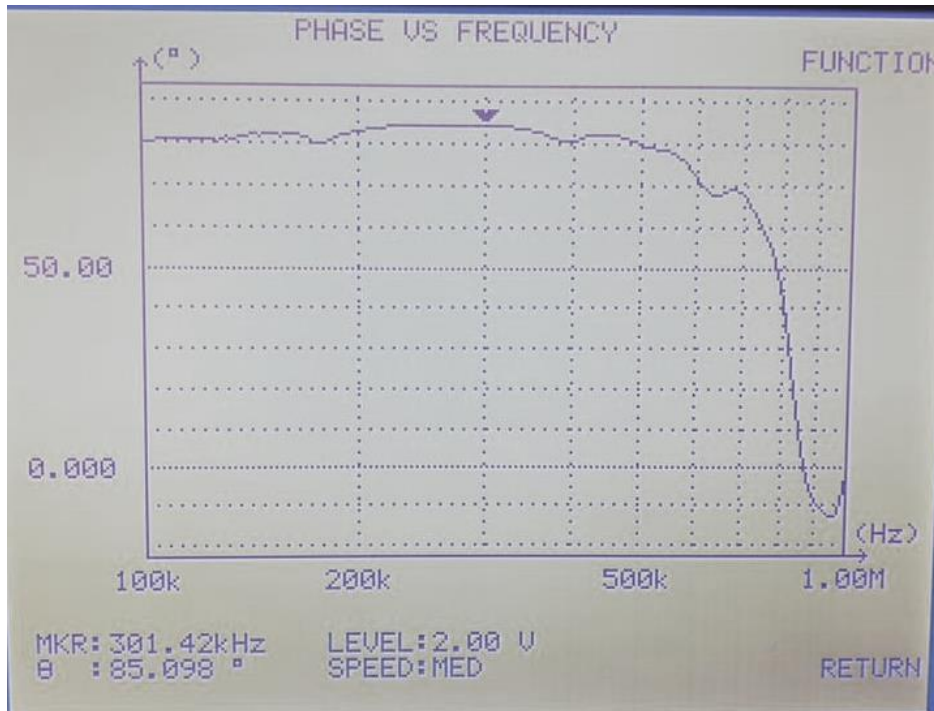
Figure 7.2.b. Plot representing variation of Impedance phase of the US transducer as a function of frequency

The measured values should be transformed from polar to rectangular to be able to design a matching circuit. The real part of the rectangular form represents the resistive part of the impedance while the imaginary part represents the capacitive or inductive component. Equations 7.1 and 7.2 are used to obtain the capacitor/inductor values from the imaginary part of the impedance. The nature of the storage devices, capacitors or inductors, is distinguished from the sign of the imaginary part of the impedance. Positive imaginary parts indicate inductive components while negative imaginary parts indicate capacitive parts.

Equation 7.1: $jX = j2\pi fL$

where f is the frequency, L is the inductance, and X is the imaginary part of the impedance

Equation 7.2: $-jX = \dfrac{1}{j2\pi fC}$

where f is the frequency, C is the capacitance, and X is the imaginary part of the impedance

Finally, an impedance of 50Ω must be added to the resistive component of the impedance to take into consideration the 50Ω impedance of the coaxial cable connecting the matching circuit to the US transducer. The coaxial cable is viewed by the source as a 50Ω resistor in series with the impedance of the US transducer. Table 7.1 shows the measured impedances, their frequencies, and their corresponding resistor, inductor, and capacitor values.

Table 7.1: Impedance of US transducer and corresponding resistor and inductor values

Frequency (KHz)	Impedance (Polar Form)		Impedance (Rectangular Form)		Resistor (Ω) (50Ω cable added)	Inductor (µH)
	Impedance magnitude (Ω)	Impedance angle	Real*	Imaginary		
200	59.29	83.82	6.38	58.94	56.38	46.91
500	206.71	80.72	33.33	204.00	83.33	64.94
700	412.13	68.87	148.57	384.42	198.57	87.40
*Real part of load impedance without considering coaxial cable 50Ω resistance						

7.1.1.2 Designing Impedance Matching Circuits using Advanced Design System (ADS) software

Advanced Design System (ADS) is a design software than can be used with RF applications including impedance matching. Impedance matching involves reducing the mismatch between the output impedance of the amplifier and the varying input impedance of the US transducer. In ADS, we set the input impedance (Z_{in}) to 50Ω and the load impedance (Z_L) and frequency to:

1. $56.38 + j46.91$ and $200\ KHz$

2. $83.33 + j64.94$ and $500\ KHz$

3. $198.57 + j87.4$ and $700\ KHz$

Using the Smith Chart Utility in ADS, we added components, inductors or/and capacitors, and observed the paths created between the load and input impedance. Then ADS generates a schematic diagram of the designed circuit. Finally, we ran the simulation and

checked the reflection coefficient S_{11} parameter. The S_{11} parameter shows how much power is reflected from the US transducer to the RF amplifier. If this parameter has a "0 dB" value, then all the power is reflected, and nothing is transmitted to the US transducer. Therefore, the lower the S_{11} parameter, the better the design is. The design process is shown in figures 7.3 (200KHz), 7.4 (500KHz), and 7.5 (700KHz).

In each figure, subfigure *"a"* shows the **Smith Chart** of the design, *"b"* shows the generated *circuit* schematic, and *"c"* the simulated S_{11} *parameter*. In subfigure (c), the S11 parameters are displayed with two different scales, the first in dB scale which should be below zero and more negative to ensure success of design, and the second in a unitless non-dB scale, ranging between zero and one, which should be closer to zero for the design success.
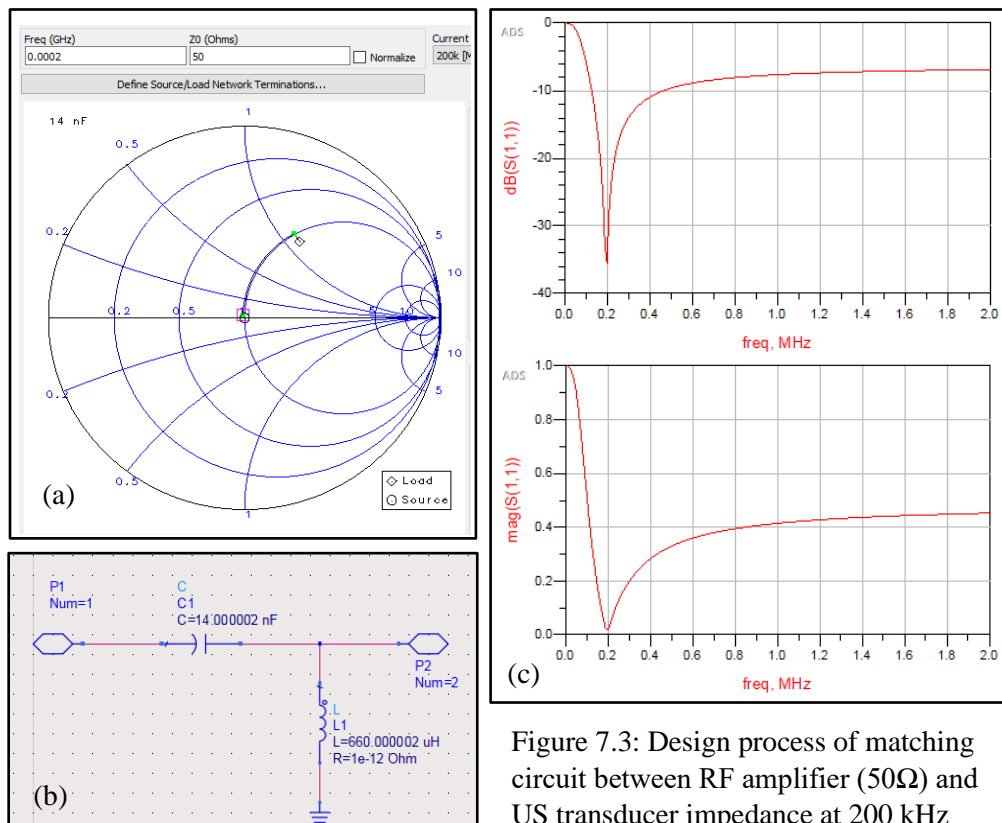
Figure 7.3: Design process of matching circuit between RF amplifier (50Ω) and US transducer impedance at 200 kHz

43
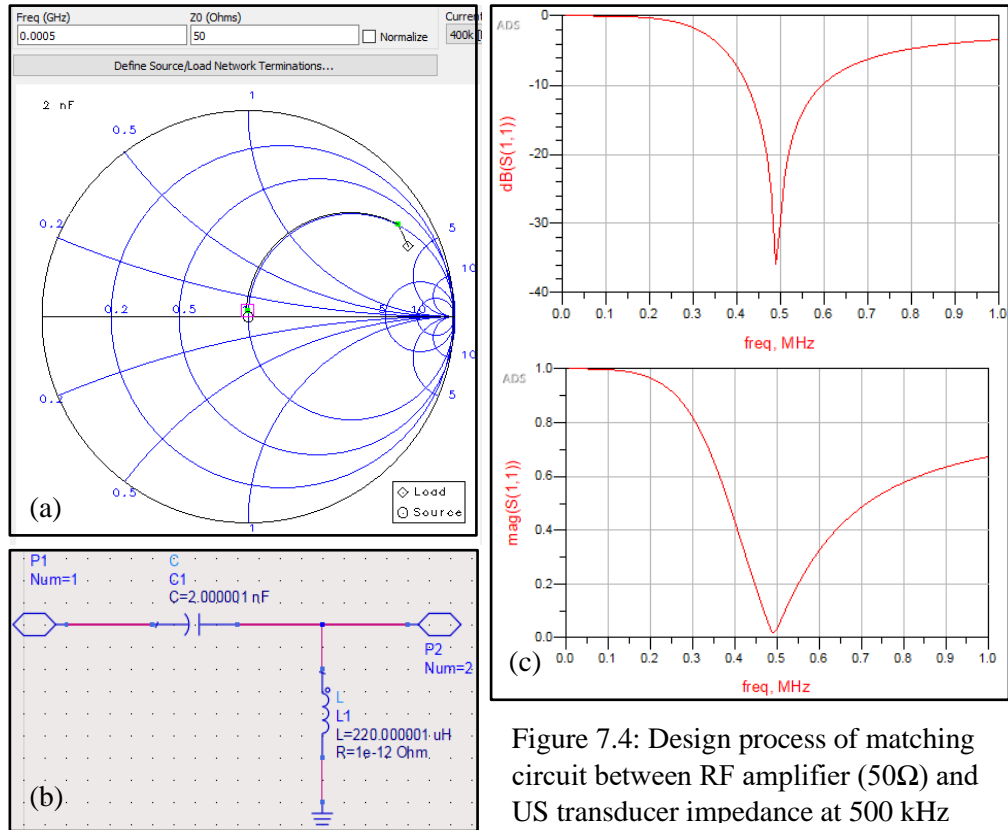
Figure 7.4: Design process of matching circuit between RF amplifier (50Ω) and US transducer impedance at 500 kHz
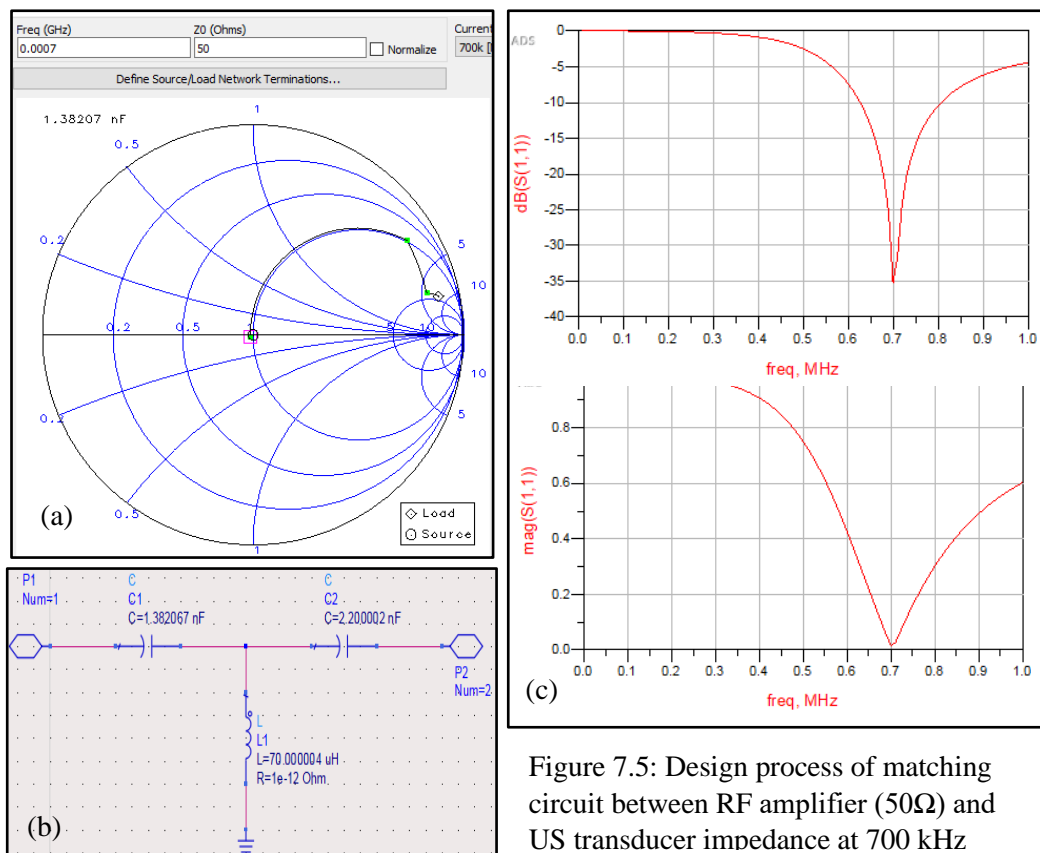
Figure 7.5: Design process of matching circuit between RF amplifier (50Ω) and US transducer impedance at 700 kHz

7.1.1.3 Choosing Components for Impedance Matching Circuits

ADS designs are theoretical designs that can use any capacitor and inductor value to ensure matching of impedances. This scenario is an ideal one since many suggested components are not commercially available. Therefore, table 7.2 summarizes the combinations of commercially available capacitors and inductors used to obtain components with values as close as possible the theoretical required ones.

Table 7.2: Commercial Inductors & Capacitors Used for Matching Circuit Design

Frequency	$C_{theoretical}$	$C_{commercial}$	Configuration	$L_{theoretical}$	$L_{commercial}$	Configuration
200 kHz	14 nF	10 nF × 1 / 1 nF × 4	Parallel	660 µH	220 µH× 3	Series
500 kHz	2 nF	1 nF× 2	Parallel	220 µH	220 µH × 1	-
700 kHz	1.38nF	1nF× 1 / 150pF× 1 / 100pF× 2 / 10pF× 3	Parallel	70 µH	10 µH× 7	Series
	2.2 nF	150pF× 1	-			

7.1.1.4 Building and testing Impedance Matching Circuits

The matching circuits were assembled and soldered based on the previously discussed designs. To test them, a waveform generator, the US transducer, and an oscilloscope were used. Figure 7.6 shows the setting for the testing. The waveform generator was set to frequencies 200, 500, and 700 kHz and output impedance 50Ω. It was then connected to the matching circuits and then to the transducer. The oscilloscope probes were connected at the output of the waveform generator and the input of the US transducer.
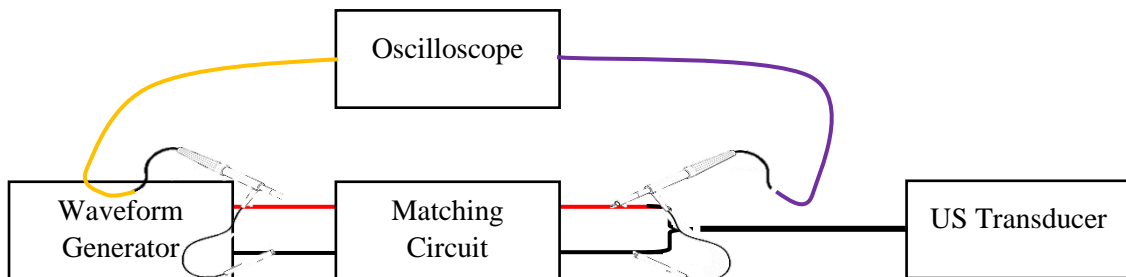
Figure 7. 6: Setup to test matching circuits

Figures 7.7, 7.8, and 7.9 show the measured voltages for frequencies 200 kHz, 500 kHz, and 700 kHz respectively. It is notable that the signal from the output of the waveform generator (yellow) and that from the input of the US transducer (purple) were in some cases out of phase, which is expected since capacitive and inductive elements were added to the circuit. Moreover, when the frequency of the waveform generator was different from that corresponding to the design of the matching circuit, a drop in the voltage was observed at the input of the US transducer.
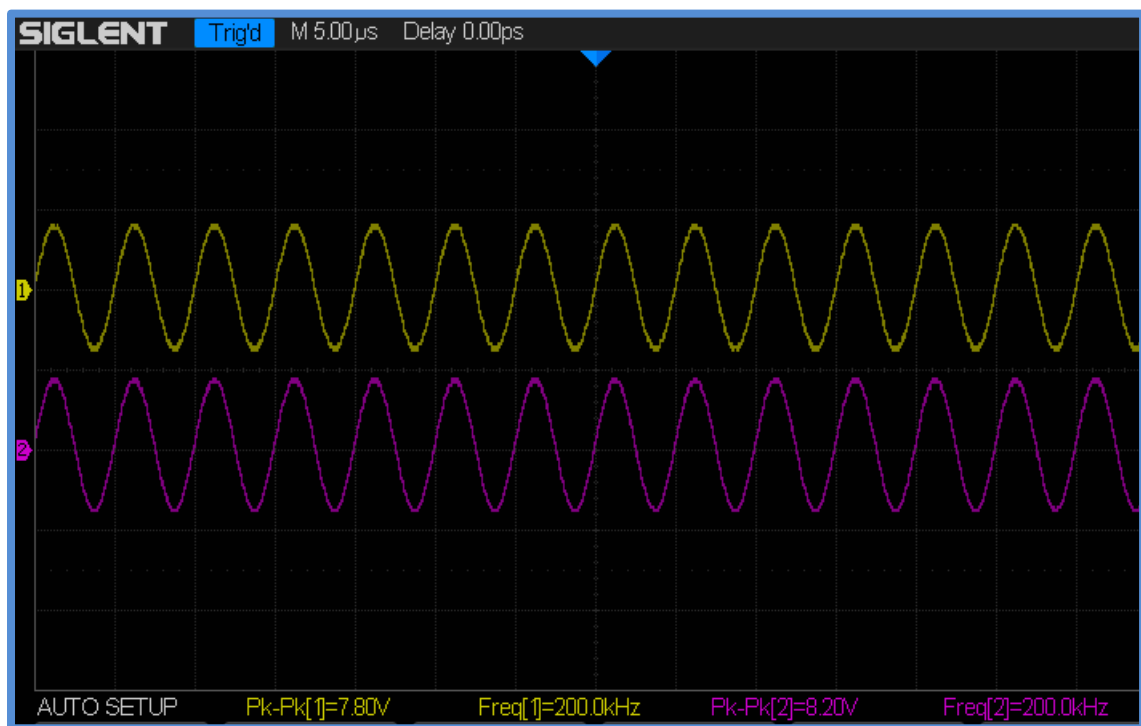
7.7: Oscilloscope screenshots for testing the matching circuit of frequency 200 kHz. The input signal to the matching circuit (yellow) has an amplitude of around 7.8 Vpp while the output signal of the matching circuit driving the US transducer has an amplitude of 8.2 Vpp with a slight phase sift due to inductive and capacitive components in the matching circuit.
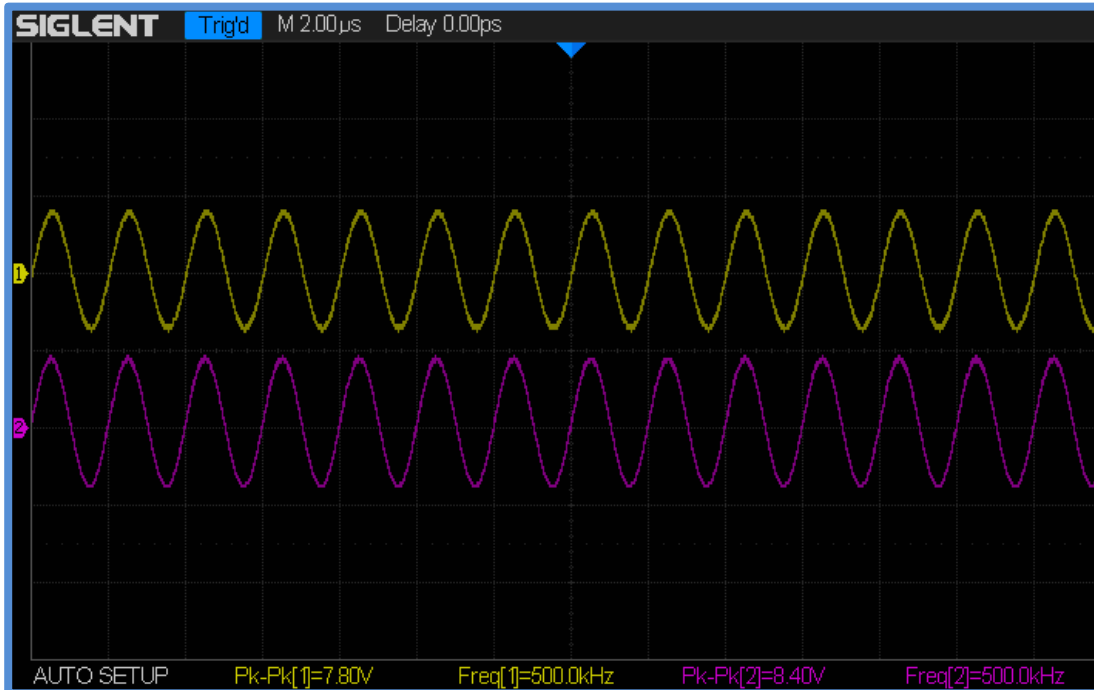
Figure 7.8: Oscilloscope screenshots for testing the matching circuit of frequency 500 kHz. The input signal to the matching circuit (yellow) has an amplitude of around 7.8 Vpp while the output signal of the matching circuit driving the US transducer has an amplitude of 8.2 Vpp .
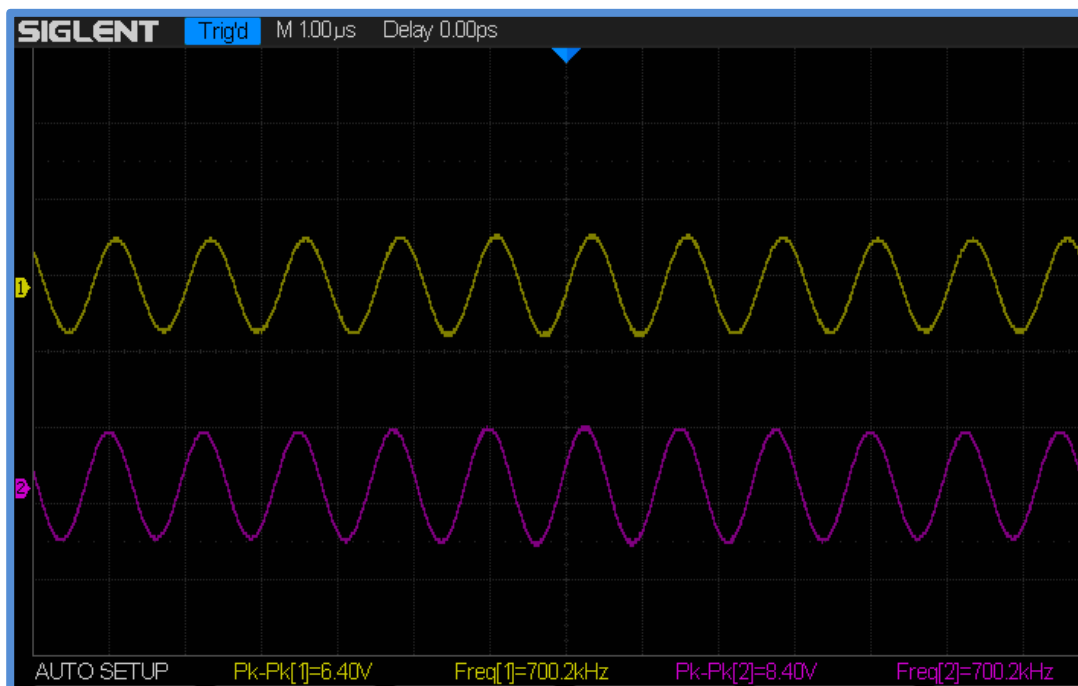
7.9: Oscilloscope screenshots for testing the matching circuit of frequency 700 kHz. The input signal to the matching circuit (yellow) has an amplitude of around 6.4 Vpp while the output signal of the matching circuit driving the US transducer has an amplitude of 8.4 Vpp with a slight phase sift due to inductive and capacitive components in the matching circuit.

7.1.2 Acoustic Profile

The mechanical signal produced by the US transducer was collected using the hydrophone to be quantized into acoustic intensity (W/cm^2). The hydrophone was mounted to a 3-axes motorized system. The system was programmed to scan the volume in front of the transducer. The data was collected and further processed.

7.1.2.1 Programming the 3-axes Motorized System

The motorized system is composed of 3 motors mounted perpendicular to each other. The micron precision of the system allows it to move in steps as small as 1.65µm. Each motor can move in both positive and negative directions. The motors were programmed to scan a cuboidal grid with a pause time of 2 seconds per move, a time enough for the data to be acquired and sent to the PC. As each motor advances, a trigger is generated and used to synchronize the waveform generator, the hydrophone motion, and the data acquisition. As figure 7.10 shows, each time one of the motors advanced, the produced trigger signaled the waveform generator to supply the US transducer and started the acquisition of the DAQ board.

The acquisition of the trigger will be discussed in section 7.1.2.2.

The motorized system was programmed while taking into consideration the size of the transducer used, the volume to be scanned, and the required precision. The transducer's diameter is 16mm. The scanned volume was a cube of side 40 mm, around 2.5 times the transducer's diameter to ensure covering the volume of the transducer and around it. Each motor was programmed to advance 1212 steps, with each step 0.001651 mm. Therefore, every time any motor moved it crossed 1212×0.001651~2mm. With a cube side of 40mm and a travel distance of 2 mm, the size of the grid considered was 20×20×20, with each
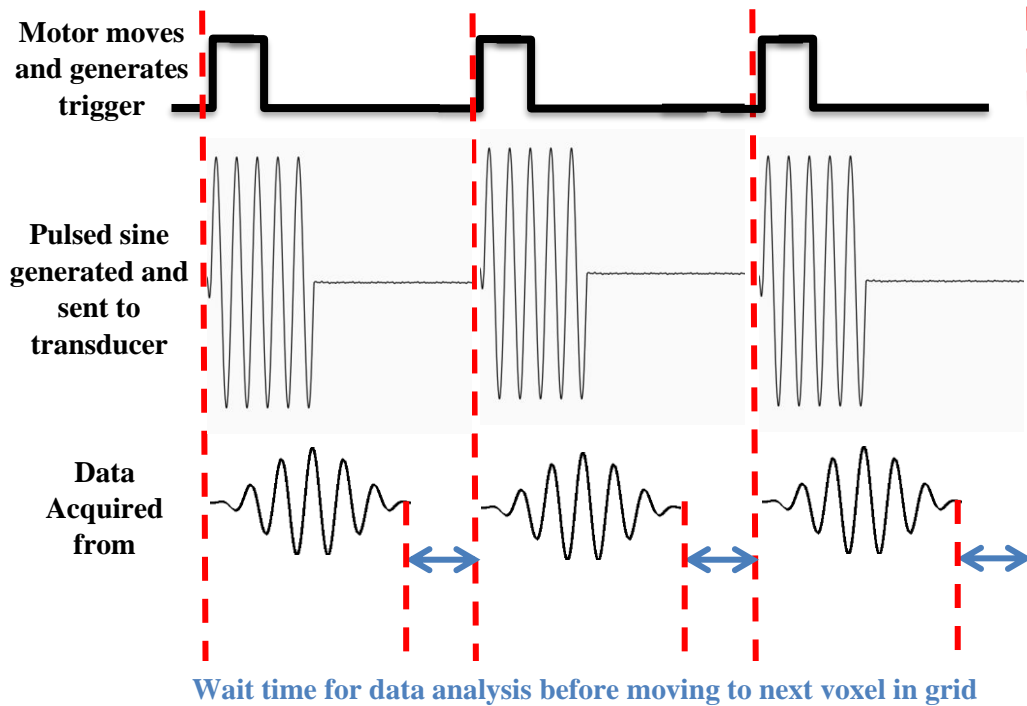
Figure 7.10: Synchrony of waveform generator, motorized axes, and data acquisition

voxel of side 2mm. This way, if we consider a horizontal cut passing through the diameter of the US transducer, 8 voxels were on this diameter, (8 acquisitions) and 12 surrounded it, 6 on its right and 6 on its left. Next, the path that the hydrophone scanned was designed. The reference point, for the directions mentioned in this part, was the face plate of the US transducer. Motor 1 moves towards (+ve) and away (-ve) the transducer; motor 2 moves to the right (+ve) and left (-ve) of the transducer; and motor 3 moves downwards (+ve) and upwards (-ve). Figure 7.11 summarizes the motors' direction of motion.
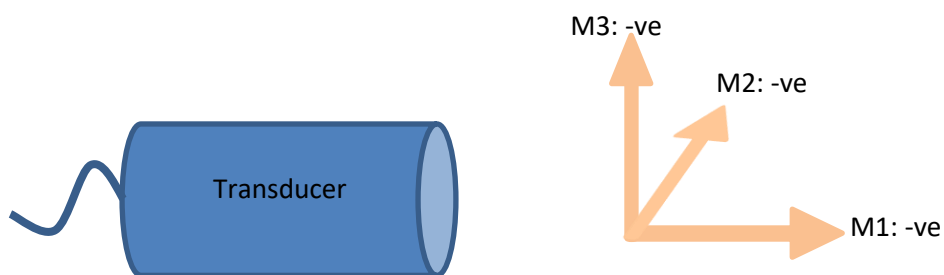
Figure 7.11: Direction of motion for motors 1,2, and 3

The path that the hydrophone took to scan the 20 by 20 by 20 grid was as follows: first motor one advanced 1212 steps (2mm) in the positive downwards direction; second motor 2 advanced 1212 steps (2mm) in the positive (to the right of the transducer) for 21 times with pausing 2 seconds after each advancement; third motor 1 advanced 1212 steps in the negative direction (away from transducer); forth motor 2 advanced 1212 steps in the negative direction for 20 times with pausing 3 seconds after each advancement, and finally motor one moved 1212 steps in the negative direction (away from transducer). By now, the hydrophone moved two rows from the first plane. This pattern was repeated for 10 times resulting in scanning the full first plane. For the next plane, the path was similar and programmed by inverting the motors. In other words, motor 3 advanced 1212 steps downwards, motor 2 advanced 1212 steps for 20 times but in the positive direction, motor 1 advanced 1212 steps in the positive direction towards the transducer, and then motor 2 moved 1212 steps in the negative direction for 20 times. This was repeated 10 times to cover all the plane. As every plane index was incremented the direction of the motors was inverted, with all odd planes the same and opposite to even planes. Figures 7.12 and 7.13 show schematics of the described path for odd and even planes respectively, but with a grid of 4 by 4 by 4 for the sake of simplicity.

The motorized system suffers from the following limitation: if motor X moved Y steps in the positive direction and then Y steps in the negative direction, a trigger won't be generated. In other words, the trigger is only generated when the sum of this step and the previous one is different than zero. To overcome this issue, the path of the motors was adjusted with an extra step out of the grid to set the sum of moves to zero and then resume the scanning process. Figure 7.14 shows the adjusted path.
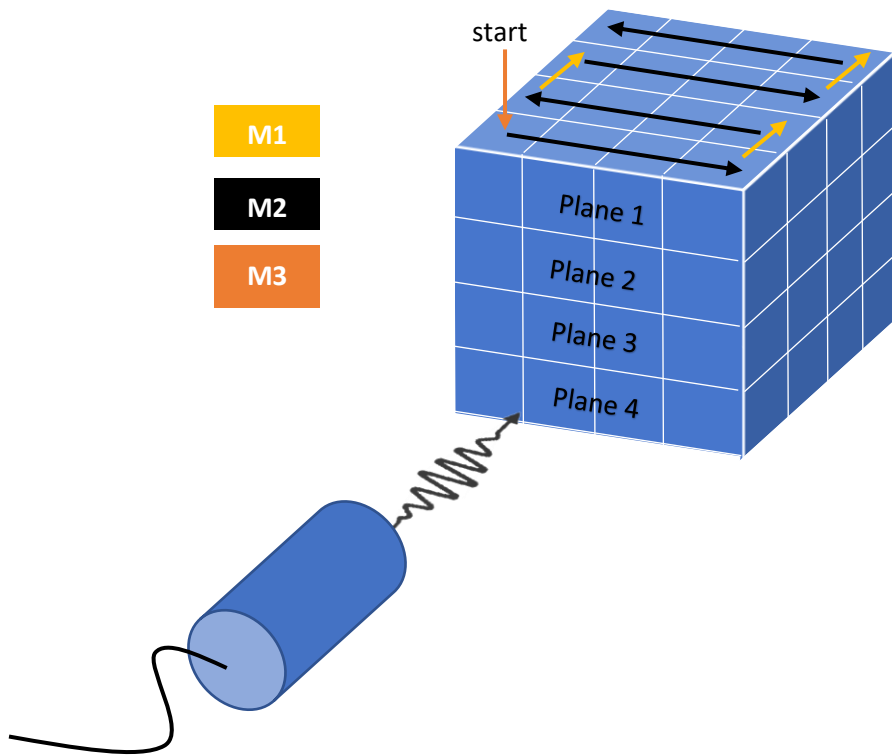
Figure 7.12: Path taken by the hydrophone in odd planes
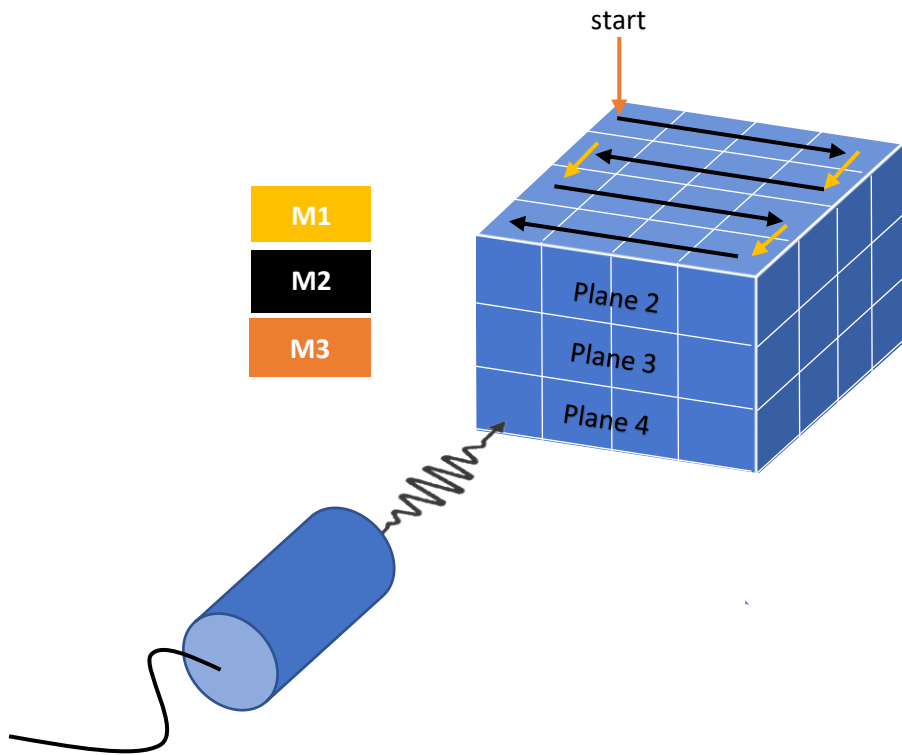
Figure 7.13: Path taken by the hydrophone in even planes
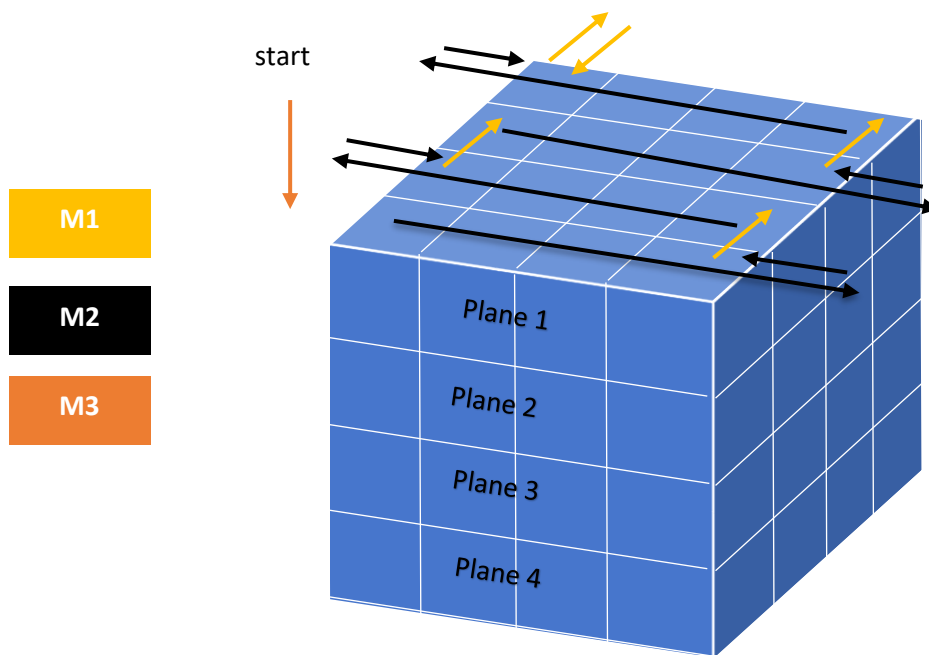
Figure 7.14: Adjusted path for odd planes

To program the motorized system, the code was written and added in a LabVIEW sub VI provided with the system. Below is a sample code for the $4 \times 4 \times 4$ grid in figure 17.14:

F,C,LM0,setPA2000,setP3M1212,I3M1212,LM0,setPA2000,setP2M1212,P20,I2M1212,P20,L4,I2M1212,I2M-1212,setPA2000,setP1M-1212,P20,I1M-1212,P20,L-4,P20,LM-0,LM-3,LM-0,L2,R

The code is further explained:

F,C,

LM0,   % Set marker 1 at current location

setPA2000,   % Set pulse width 20000us = 20ms

setP3M1212,   % Send trigger when motor 3 moves

I3M1212,   % Move motor 3 downwards

LM0,	% Set marker 1 at current location
setPA2000,	% Pulse width 20000us = 20ms
setP2M1212,	% Send trigger when motor 2 moves
P20,	% Pause for 2 seconds
I2M1212,	% Move motor 2
P20,	% Pause for 2 seconds, but this command is ignored by the next line so it is added to avoid ignoring the motion of motor code
L4,	% Repeat 4 times and ignoring previous command (P20)
I2M1212,	% Move motor 2 extra step
I2M-1212,	% Move motor 2 back the extra step
setPA2000,	% Pulse width 20000us = 20ms
setP1M-1212,	% Send trigger when motor 1 moves
P20,	% Pause for 2 seconds
I1M-1212,	% Move motor 1
P20,	% Pause for 2 seconds, but this command is ignored
L-4,	% Repeat from first marker 4 times while alternation Motor 2 direction and ignoring previous command (P20)
P20,	% Pause for 2 seconds
LM-0,	% Reset marker loop to first one in program
LM-3,	% Repeat code from current set marker while alternating motor 1 and 2 direction (**By now we have 2 planes**)
LM-0,	% Reset marker to first one
L2,	% Repeat from marker 1 more time (**By now we have 4 planes**)
R	% Run motors

The pseudo code is:

```
for i=1                                   4 planes
    for j=1:2                             2 planes
        for k=1:4                         1 plane
            for m=1:4                     1 row
                move motor 2
                pause
            move motor 2 extra step and revert it
            move motor 1
            invert sign of motor 2
        move motor 1 extra step and revert it
        flip sign of motors 1 and 2
```
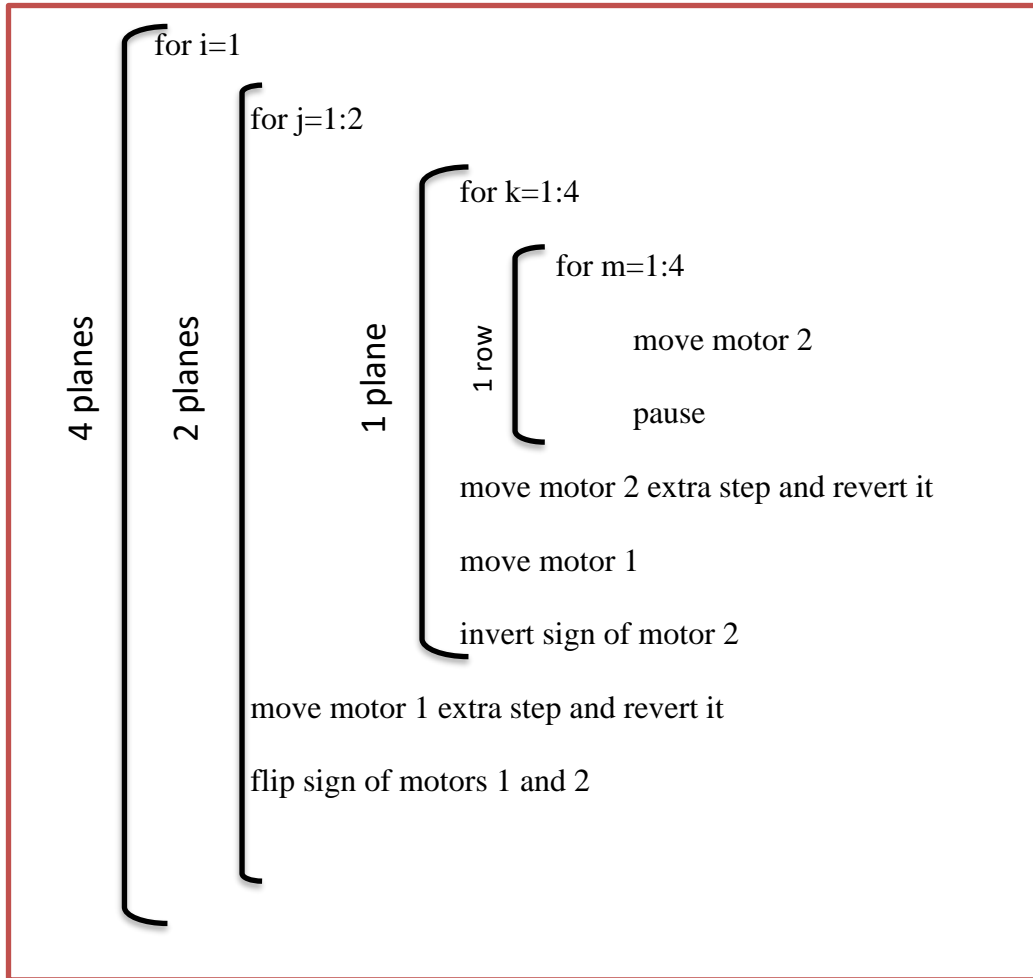
7.1.2.2 Data Acquisition

Two signals were acquired for characterizing the US transducer, the trigger from the motorized axes and the hydrophone signal.

7.1.2.2.1: Acquiring the Motorized Axes Trigger

As mentioned earlier, the trigger is produced whenever any of the motor advances. This trigger is generated through the auxiliary I/O Connections, from pins 1 (ground) and 15 (output 2- O2). Knowing that the trigger is a TTL signal with amplitude 5V and is generated every motor advancement, or every 2 seconds (0.5 Hz), the sampling frequency was set above the Nyquist rate (1Hz). The motorized axes system is composed of two

motor boxes, the first is for controlling for motors 1 and 2 and generates their triggers, and the second for motor 3 control and trigger generation. Therefore, triggers from both motor boxes should were connected to the Analogue input pins of the data acquisition board. For our application, we used the NI Elvis III board. The low sampling rate requirement for the trigger allowed us to use the analogue input pins indicated with an orange box in figure 7.15.
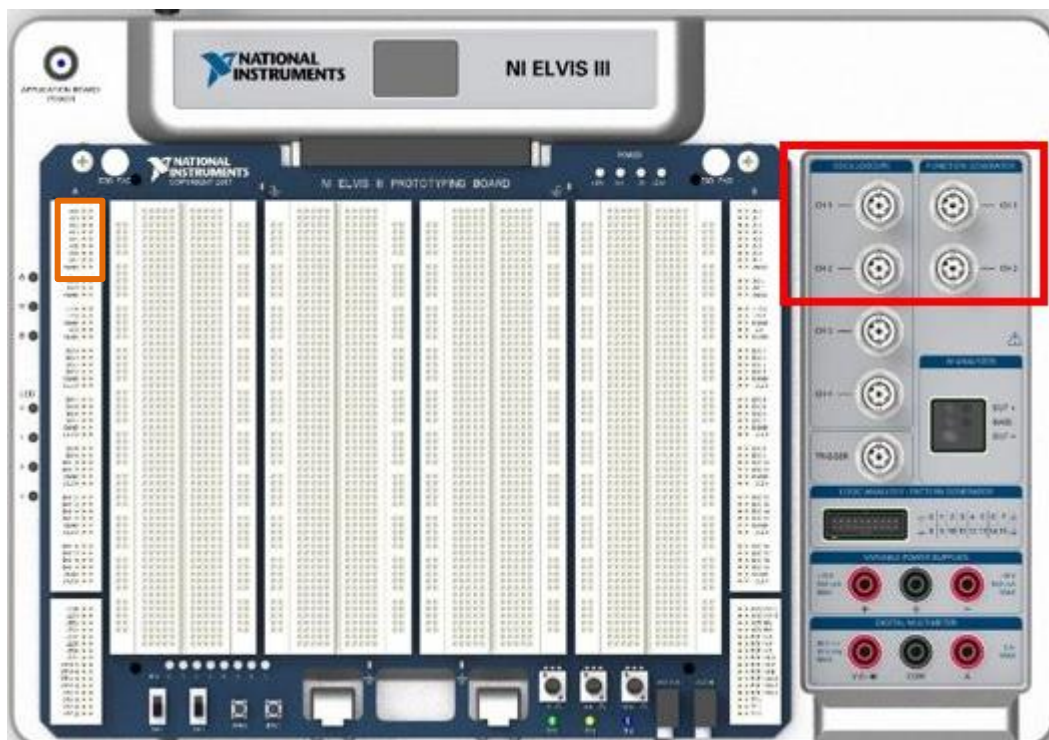
Figure 7.15: NI Elvis III board showing location of analogue input pins (orange) and oscilloscope channel (red box)

In LabView NI Elvis III module, the analogue input VI was used to continuously sample from the analogue input pin 1 that the trigger was connected to. The sampling frequency was set to 1 kHz with 2000 samples ensuring a window of 2 seconds which is much larger than the pulse duration of the generated trigger (20ms). The peak of the acquired signal was always compared to a minimum of 0.8V, when it rose above this value than a trigger

was generated, and a counter is updated along with the row index of the array that stored the hydrophone data. It is important to mention that although the data from the hydrophone is continuously sampled, yet it is not stored unless there was a trigger. That being said, the result of the comparison of the trigger was connected to an if loop in LabVIEW, whenever it became "True", the trigger counter was incremented by 1, the index of the hydrophone data array was incremented and the hydrophone data was saved to the new row in the array. Figure 7.16 shows the graphical code for the comparator of the trigger while figure 7.17 shows the graphical code for the increment and hydrophone data storing. The pseudo code for the graphical code is:

IF (trigger=1)

  THEN <increment counter;

       increment index of array;

        save data from hydrophone>;

  ELSE <DO Nothing>;

ENDIF

7.1.2.2.2: Acquiring the hydrophone signal

 Acoustic mechanical signals produced by the US transducer propagated in the degassed water tank to reach the hydrophone, excited its piezo material, and produced an electrical signal. The frequency of the electrical signal produced was the same as that provided to the US transducer, therefore, acquired hydrophone data frequency ranged between 200 and 700 kHz. The sampling rate for these signals should range between 400kHz and 1.4MHz. We chose a sampling frequency of 1.5MHz to acquire these signals. The analogue input pins in Elvis III don't provide such high sampling rates, but the oscilloscope channels do. We connected the hydrophone to the oscilloscope channel on
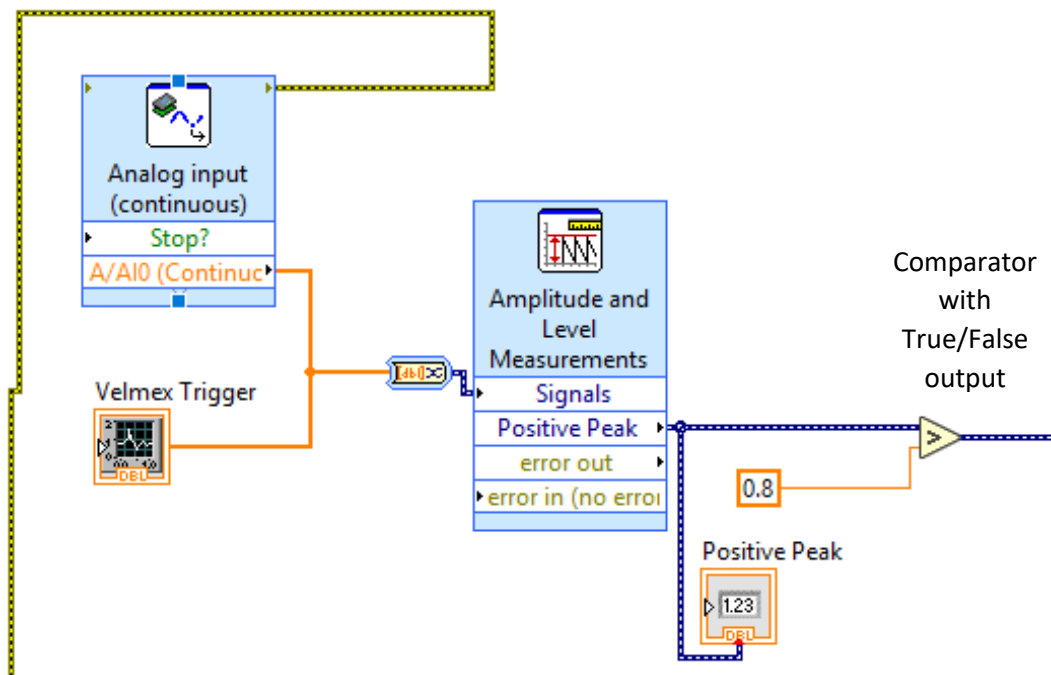
Figure 7.16: LabVIEW screenshot for the trigger comparator
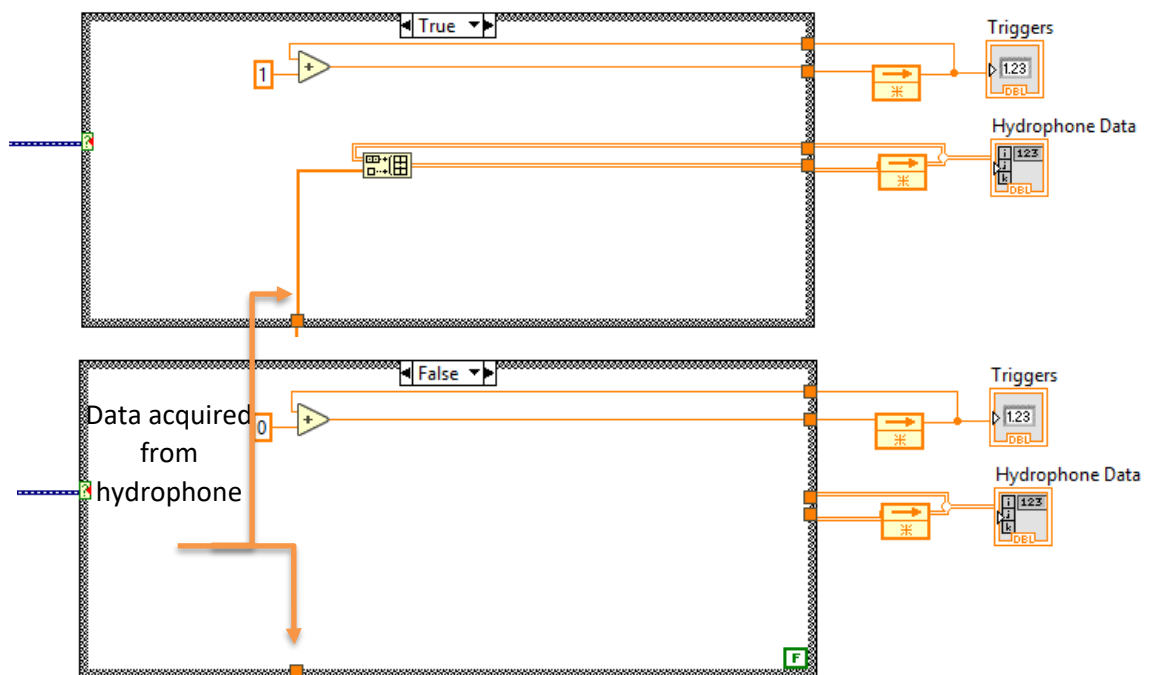
Figure 7.17: Screenshots from LabVIEW showing counter and hydrophone array in "True" and "False" cases

the NI Elvis III board, as shown in figure 7.15 (red box). In LabVIEW NI Elvis III module, the oscilloscope VI was initialized only once and hence the initialization was

57

done outside the while loop. The acquisition on the other hand was continuous and that's why it was placed inside the while loop. The "Read Scope VI" outputs data as a waveform which was transformed into an array and sent to the if loop mentioned earlier. If the trigger was "True", the oscilloscope data was saved in the array. The parameters that should be set for the oscilloscope setting are summarized in table 7.3. Figures 7.18 and 7.19 show the graphical codes for initializing the oscilloscope and transforming the waveform data into integers to be sent to the array.

Table 7.3: Oscilloscope parameters

Parameter	Value
Channel	Scope 1
Vertical Range	1 Volt (since hydrophone signal has small amplitude)
Probe Attenuation	×1
Vertical Offset	1
Sampling Mode	Average
Sampling Rate	1.5MHz
Acquisition Time	20 ms (>duration of US pulse sent from waveform generator)
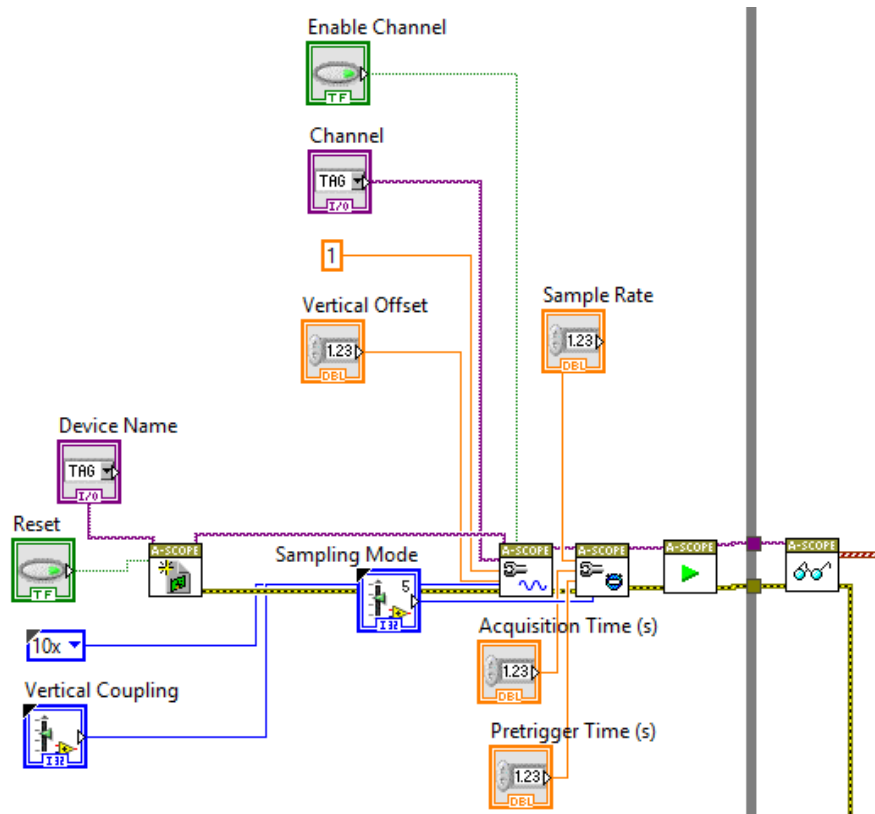
Figure 7.18: LabVIEW screenshot for oscilloscope initialization
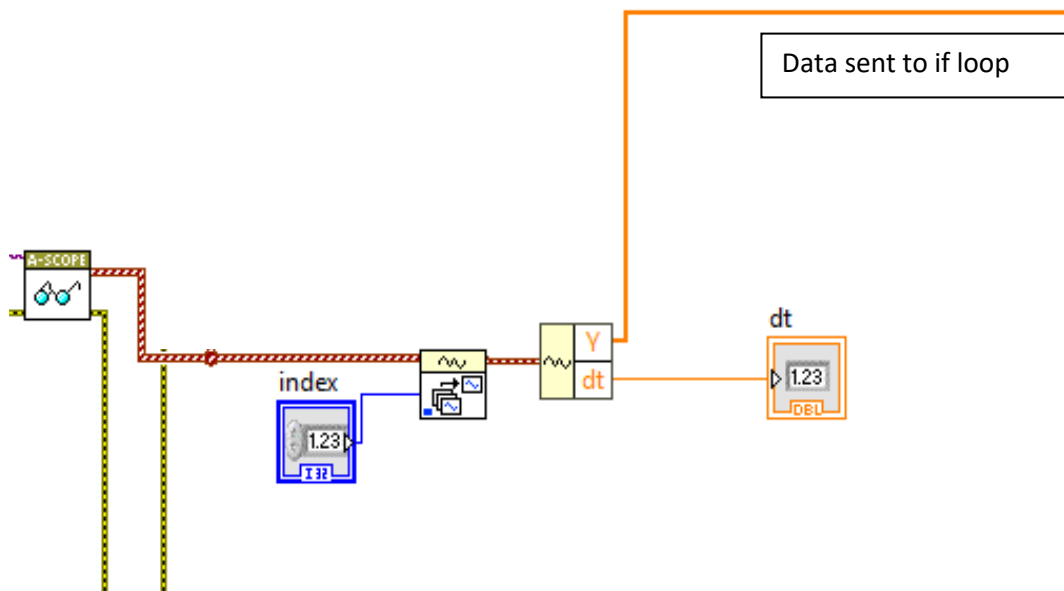
Figure 7.19: LabVIEW screenshot for changing waveform data into integers to be stored in array

To summarize, the flow of the data acquisition was as follows (figure 7.20):

1. The oscilloscope was initialized once every time the VI was run and was outside the while loop (purple box)

2. The oscilloscope read data from the hydrophone continuously and was placed inside the while loop. Data type was transformed from waveform to integer array (red box)

3. The trigger continuously read data from the motorized axes system and was inside the while loop (blue box)

4. Every time a trigger was generated, it was compared to a threshold (green box), if it were greater than 0.8 V, the if loop (orange box) was activated incrementing the trigger counter and saving data received from the oscilloscope into the array.
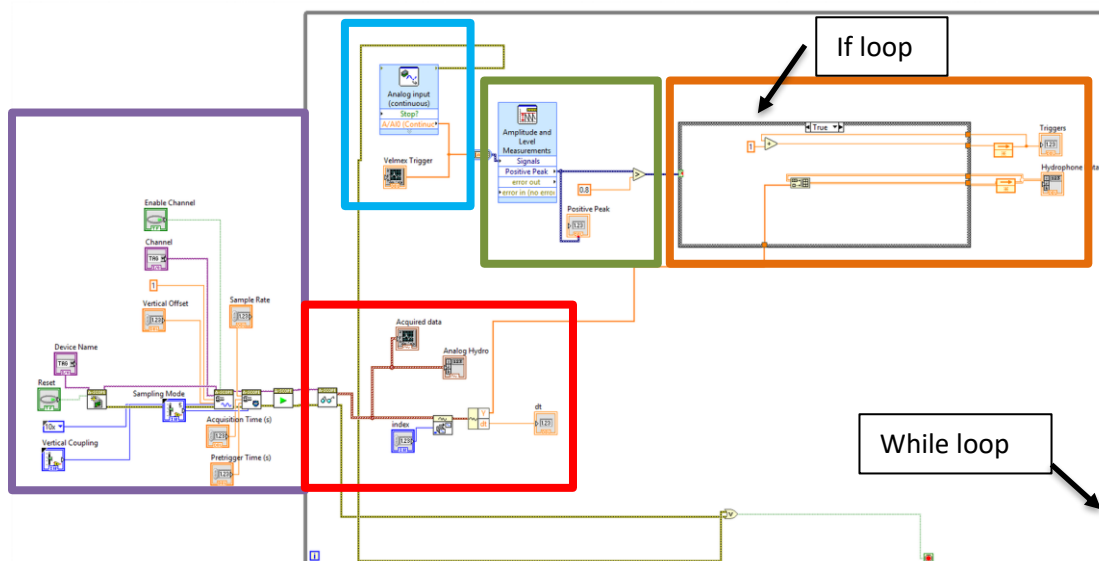
Figure 7.20: LabVIEW screenshot for the entire data acquisition VI

7.1.2.3 Acoustic Profile Setup and Running the Scans

The setup for running a scan was first prepared by sonicating around 7 liters of degassed deionized double distilled water. The water was poured into the water tank gently to avoid the accumulation of air bubbles in it. The US transducer was connected to the waveform

generator as figure 7.1 shows. Then it was immersed into the tank and oriented towards the hydrophone. The scanned grid was a cube of side 40 mm, therefore we ensured that a distance of 12 mm of water exists below, above, to the right and to the left of the transducer to guarantee that the scanned volume is all beneath water level (figure 7.21).
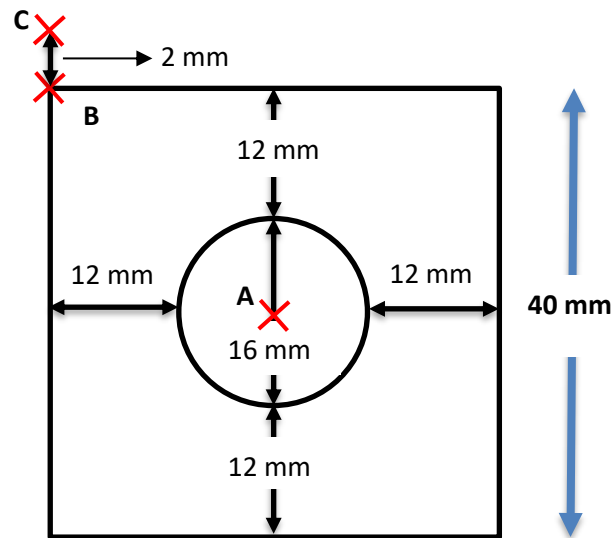
Figure 7.21: Front view of transducer and water minimum water level

The hydrophone was mounted to the 3 axes motorized system and positioned manually facing the center of the transducer and almost touching the face plate of the transducer. Then, it was moved, using a LabVIEW code, 20 mm to the left (Motor 2 advanced 12,120 steps in the negative direction) of the transducer, and 22 mm above the transducer (Motor 3 advanced 13,332 steps in the negative direction). This way we move the hydrophone from point A to point C shown in figure 7.21. Note that the hydrophone was not moved to point B since the motors were programmed to move from point C to B and then collect the first measurement. Figure 7.22 shows a transducer immersed in the water bath, the hydrophone mounted in front of it, and the acquisition pallet showing a trigger and a signal from the hydrophone.
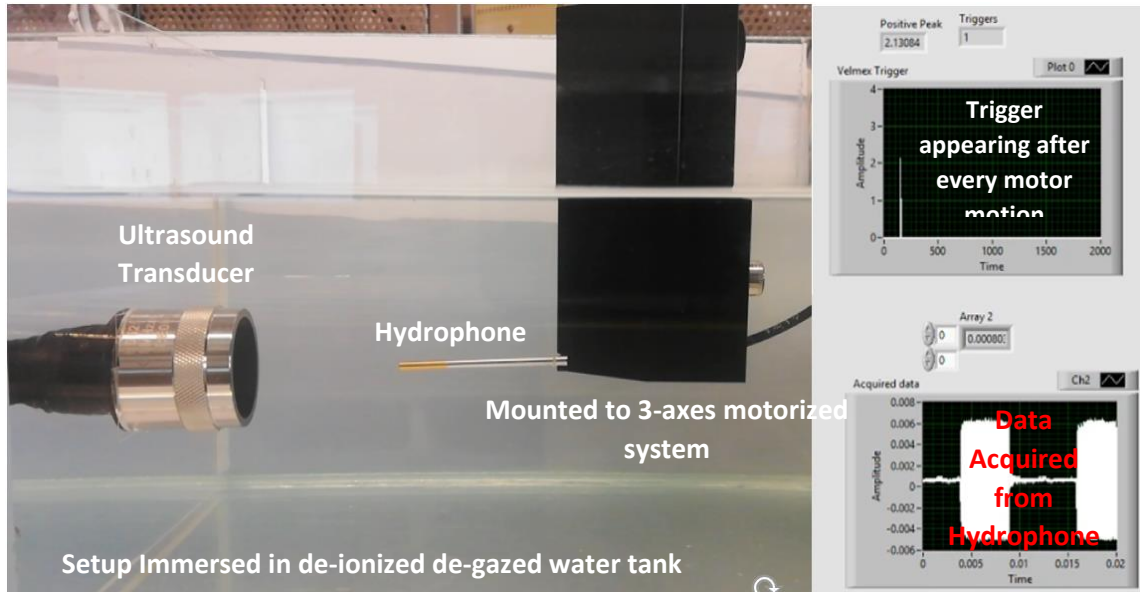
Figure 7.22: Picture of US transducer scanning

7.1.2.4 Data Processing and Acoustic Intensity

The scanning of the volume around the transducer resulted in an output array of size:

$Rows$: $number\ of\ grid\ voxels\ edges + extra\ voxels =$

$number\ of\ grid\ voxels\ edges$

$$+ (20\ extra\ from\ motor\ 2\ in\ each\ plane\ \times number\ of\ planes)$$

$$+ 20\ extra\ from\ motor\ 1 = (n+1)^3 + n^2 + n$$

$$= (21 \times 21 \times 21) + (20 \times 20) + 20 = 9681$$

Columns$= 1638$

Each row, representing a single voxel, was processed separately according to the algorithm of transforming electrical signals to acoustic intensities.

7.1.2.4.1 Acoustic Intensity Algorithm

The signal acquired from the hydrophone is simply an alternating voltage signal depending on the excitation of the piezo material in the hydrophone. To derive the acoustic intensity the following algorithm was used [130]:

1. Transform voltage into acoustic pressure using the formula:

Equation 7.3: $M_1(f) = G_a(f) \times M_c(f) \times \left(\frac{C_h}{C_h + C_a}\right)$

where $G_a(f)$ and C_a are the preamplifier gain and capacitance, and $M_c(f)$ and C_h are the hydrophone EOC sensitivity and capacitance.

In our experiments we didn't use a preamplifier for the acquired signal and therefore we don't have to account for its gain and capacitance while finding the acoustic pressure.

2. Find the pulse intensity integral (PII) using the formula:

Equation 7.4: $PII = \frac{\int_{t1}^{t2} v^2(t)dt}{\rho c \times M_1^2(f)}$

where v(t) is the hydrophone voltage, $M_1(f)$ is the hydrophone sensitivity at the center frequency, $t1$ and $t2$ represent the time duration of interest, and ρc is the specific acoustic impedance.

3. Find the Pulse Duration (PD), using the formula:

Equation 7.5: $PD = 1.25(t_3 - t_4)$

where t_3 is the time when the amplitude is 10% below peak PII and t_4 is 90% below peak PII.

4. Calculate the spatial peak pulse average intensity (I_{sppa}), which is the maximum intensity in the beam averaged over the pulse duration according to the following equation:

Equation 7.6: $I_{sppa} = \frac{PII}{PD}$

5. Calculate the acoustic intensity at each voxel of the grid volume to observe the distribution of the mechanical waves in the volume and to create heat maps that would be helpful in visualizing this distribution.

Table 7.4 below shows the units for each of the above variables.

Table 7.4: Symbols and units for the variables used in the acoustic intensity calculations

Variable	Symbol	Unit
Acoustic pressure	$M_1(f)$	Volts/Pascal (V/Pa)
Preamplifier gain	$G_a(f)$	Unitless
Hydrophone EOC sensitivity	$M_c(f)$	Volts/Pascal (V/Pa)
Capacitance	C_h/C_h	pFarad (pF)
Pulse intensity integral	PII	µJoule/cm² (µJ/cm²)
Hydrophone voltage	$v(t)$	Volts (V)
Specific acoustic impedance	ρc	MPascal.second/meter (MPA.s/m)
Pulse Duration	PD	Seconds (s)
Spatial peak pulse average intensity	I_{sppa}	Watts/cm²

The result of the algorithm is an array of dimension 9681×1.

7.1.2.4.2 Removing Extra Voxels

As discussed in earlier sections, additional steps outside the grid are covered to overcome the limitations of the motorized axes system. These steps should be removed before creating the heat maps. First, we remove the extra steps covered by motor 1 which are multiples of $(n+1)^2$. Then extra steps covered by motor 2 are removed and are multiples of $n+2$. The pseudo code is the following:

```
FOR <i=1: array rows>
        IF <Remainder of  i/(n + 1)² = 0>
                Remove value
                Shift array one row up
        END IF
END FOR
FOR <j=1: new array rows>
        IF <Remainder of  i/n + 2 = 0>
                Remove value
                Shift array one row up
        END IF
END FOR
```

The result is an array of size 9261×1 ($20 \times 20 \times 20$ grid of $21 \times 21 \times 21$ edges)

<u>7.1.2.4.3 Reshaping Matrix & Heat Map</u>

Heat maps are 4D representations of the acoustic intensities. The scanned volume was a cuboidal shape. The first 3 dimensions represented the x, y, and z co-ordinates of each voxel, while the 4rth dimension was the acoustic intensity. The heat map showed a graphical representation of the distribution of the acoustic intensity where the values were represented with colors. The 8000×1 matrix was reshaped in a fashion similar to the motion of the hydrophone. The reshaping was completely dependent on the path that was chosen in the previous section and can be changed based on different volumetric shapes and preferences. Note that MATLAB software was used for signal processing and data analysis presented in section 7.1.2.3.

7.1.3 Coupling Cone

The heat maps generated previously showed the location of the highest intensity. A resin cone was designed using Solid Works software with the dimensions detailed in table 7.5. The cones served as a guiding and coupling tool for the US signal. The diameter of the transducer was much larger than that of the sciatic nerve and the US signal needed a specific medium to travel, which made hollow cones ideal for guiding the US signal to the sciatic nerve and provided a coupling medium. Figure 7.23 shows the design of the cones. The cone was printed using the Formlabs Form 2 3D printer that heated resin to 238ºC and extruded it to form the designed shape. The 3D printed cone was then cured using an ultra-violate (UV) station for 24 hours with a UV light of wavelength 405nm.

Table 7.5: Dimensions of designed coupling cone

Dimension	Value	Reason
Larger Diameter	16 mm	Diameter of the US transducer
Smaller Diameter	1mm	Diameter of the Sciatic nerve is 1-1.5mm
Height	10 mm	Length from US transducer's face plate to point of highest intensity
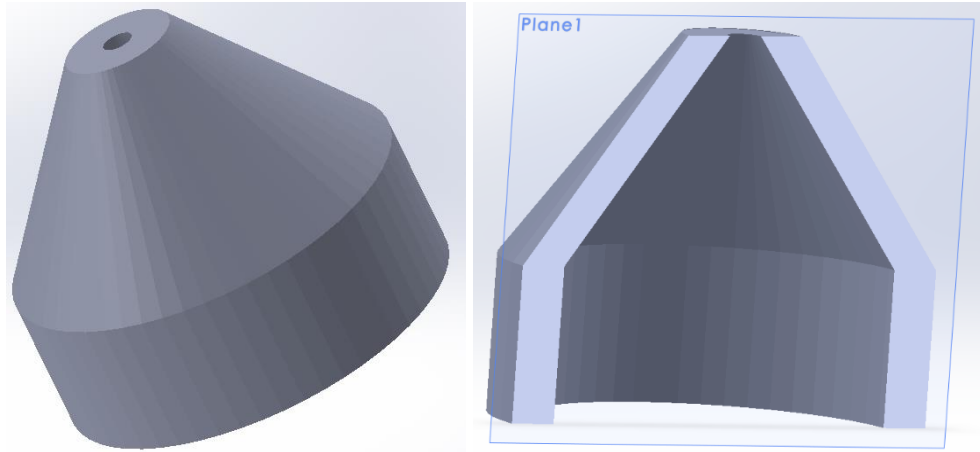
Figure 7.23: Design of PLA coupling cones

7.2. Ultrasound Stimulation of the Sciatic Nerve

The ability of the US stimulation to cause neuromodulation and suppression of pain was tested on the sciatic nerve. As mentioned earlier, the pain experience is translated physiologically into an intense or high frequency stimulus. Therefore, to mimic pain sensation we applied electrical stimulation of several intensities (2.5, 5, and 7.5 V) to an exposed sciatic nerve while subjecting it to US stimulation. We observed the EMG response from the gastrocnemius muscle that is controlled by the sciatic nerve.

7.2.1. Physiological Recording Setup

The setup needed for physiological recordings, namely EMG recordings consists of the following:

1. An electrical stimulator capable of varying the frequency, intensity, and duration of the electrical pulses it generates to stimulate the nerve

2. A stimulus isolation unit used to produce isolated constant pulses

3. A silver-silver bipolar curved stimulating electrode to supply electrical stimulation to the sciatic nerve

4. A bio-filter to remove noise from EMG signals recorded from the gastrocnemius muscle

5. A bio-amplifier to increase the amplitude of the acquired signal that is in few mVs

6. A data acquisition system to acquire and store data

Figure 7.24 shows the flow and connections of the devices used.
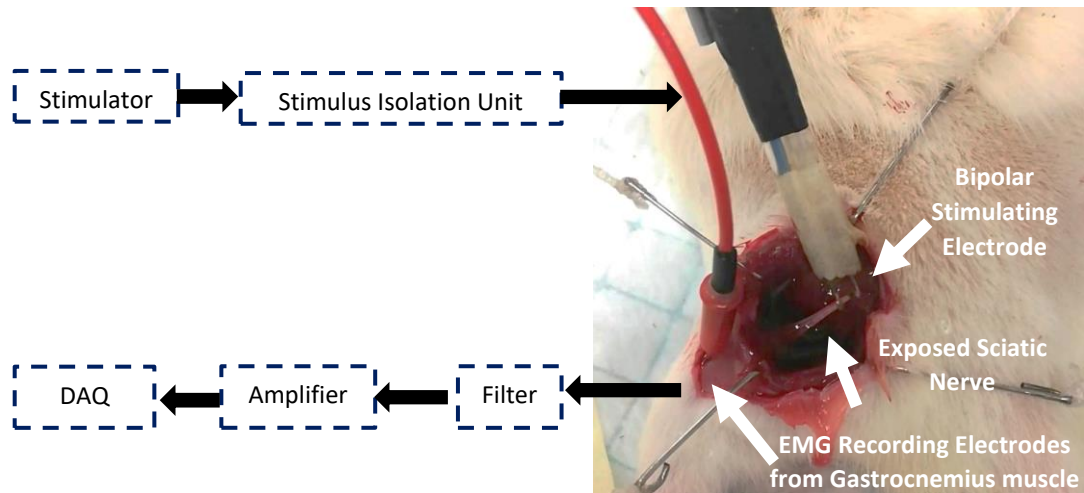
Figure 7.24: Schematic of the physiological recording setup

It is important to mention that the band pass filter used for the acquired EMG signal has a low cut-off frequency of 10 Hz and high cutoff frequency of 3 kHz. As for the bio-amplifier a gain of 100 was used.

The required devices for the US stimulation are the US transducers, the matching circuit, the Rf amplifier and the waveform generator.

7.2.2. Animal Surgery

The Sprague Dawley rats used in these experiments underwent a surgery to expose the sciatic nerve and stimulate it using electrical and US stimulation. The surgical procedure was as follows:

• Prepare 2 to 3 mL of anesthesia 80% Ketamine 20 %Xylazine

• Weigh the rat and inject with a 1 mL dosage of anesthesia

- Wait until rat is sedated (Figure 7.25-a)

- Clip the fur in the surgical site using an electric shaver (Figure 7.25-b)

- Using a scissors, cut through the skin layer surrounding the mid-thigh area of the left/right leg (Figure 7.25-c)

- Using the scissors and the blind dissection method, create a cut few millimeters beneath the leg bone. Blind dissection is used to avoid tissue damage and the cutting of the sciatic nerve by accident (Figure 7.25-d)

- Once the sciatic nerve is detected, use a retractor to open the incision wider and get better access to the nerve

- Using 2 fine forceps, remove fascia surrounding the nerve (Figure 7.25-e,f)

- Place the rat on the stereotactic frame

- Using hooked needles, retract muscles and tissue surrounding the nerve, while ensuring the formation of a cavity to be filled with saline guarantee a coupling medium around the sciatic nerve (Figure 7.25-g)

- Hook the sciatic nerve to the electrical stimulating electrode in a position as close as possible to the spinal cord (Figure 7.25-h)

- Place EMG recording electrodes in the muscles of the thigh (gastrocnemius muscle) (Figure 7.25-i)

- Add saline solution to the location of the surgery to form a saline pool around the nerve

- Fill the coupling cone with US gel while guarantying the absence of air bubbles

- Position the tip of the transducer cone so that it is in the saline pool and aimed at the nerve (Figure 7.25-h)

- Connect the transducer to the function generator and amplifier.

- Set function generator to continuous signal setting and specify the required frequency

- Adjust stimulation parameters and connect recording electrode to a filter, an amplifier, and a data acquisition system.

- Begin stimulation and recording according

Figure 7.25 shows the steps followed.
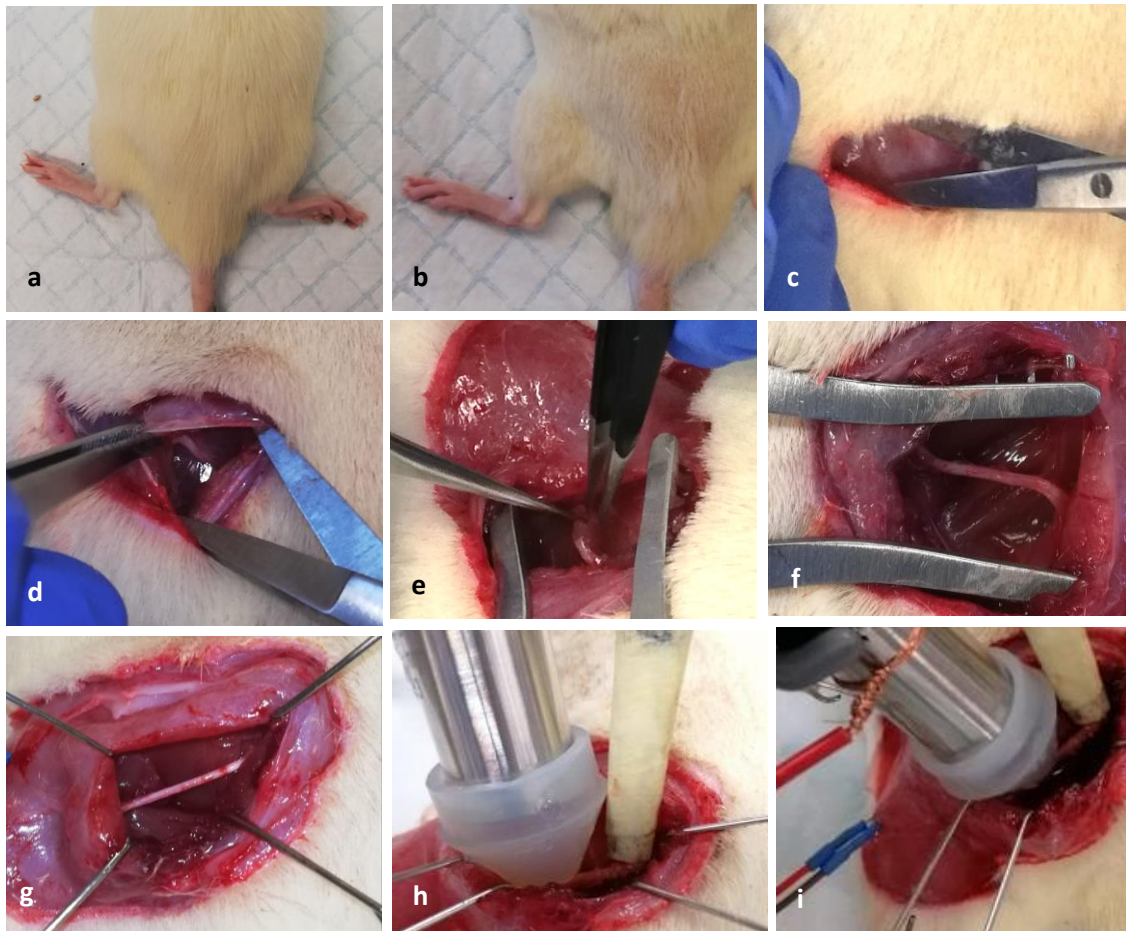
Figure 4.25: Steps for surgical procedure to expose the sciatic nerve

7.2.3. Stimulation Parameters

The electrical stimulation used had a frequency of 10 Hz, pulse duration 2ms, delay 0ms and amplitudes of 2.5, 5, and 7.5 V. The US stimulation had a continuous nature, with frequencies 200, 500, and 700 kHz, and several acoustic intensities (table 7.6).

Tables 7.6 shows the electrical and US stimulation parameters combinations used in the experiments.

Table 7.6: Electrical and US stimulation parameters

US Frequency (kHz)	US Acoustic Intensity (W/cm^2)	Electrical Frequency (Hz)	Electrical Amplitude(V)
200	9.34	10	2.5
			5
			7.5
	4.16		2.5
			5
			7.5
	2.58		2.5
			5
			7.5
500	11.1	10	2.5
			5
			7.5
	6.06		2.5
			5
			7.5
	5.04		2.5
			5
			7.5
700	17.51	10	2.5
			5
			7.5
	5.65		2.5
			5
			7.5
	2.83		2.5
			5
			7.5

It is important to mention that not all these combinations were tested in the same experiment and this will be detailed in upcoming sections.

7.2.4. Data Acquisition

The data was acquired using the Power1401-3A data acquisition device from Cambridge electronic design (CED). 3 waveforms were acquired at a sampling rate of 12.5 kHz: the electrical stimulation waveform, the US stimulation waveform, and the EMG from the

gastrocnemius muscle. The reasons for acquiring all three signals were: to ensure that the electrical and ultrasound stimulation devices are functional and to use them in the data processing, namely in calculating the latency in the muscle response. The data acquisition device has an interface with "Spike 2" software. Each recording stimulation trial recorded was saved as a separate file and converted later into ".m" files to be processed in MATLAB.

7.2.5. Data Processing

The recorded EMG was further processed using MATLAB. First, the 3 waveforms from each file were imported into MATLAB workspace and copied into 1 dimensional arrays. A notch filter was applied to the EMG waveform to eliminate the 50 Hz frequency from the mains. Each recorded EMG waveform was divided into 5 regions:

1. Region 1 (R1): No stimulation was applied

2. Region 2 (R2): Electrical stimulation was applied

3. Region 3 (R3): Electrical and US were applied

4. Region 4 (R4): Electrical stimulation was applied

5. Region 5 (R5): No stimulation was applied

The regions were identified based on the acquired electrical and ultrasound waveforms that indicate the time that each stimulation started and ended. The following outcomes were then observed in each region:

1. *The area under curve (AUC) of the rectified EMG waveform:* in each region, the waveform was rectified (absolute value) and the area was computed and then normalized by the duration of the region. The unit for this outcome is Volts^2/second (V^2/s).

2. *The latency or the time between electrical stimulation and muscle response:* in regions 3, 4, and 5, the latency for each single applied pulse was computed. Then the computed values were averaged and had a unit of milli-seconds (ms).

3. *The amplitude of the recorded EMG or the difference between the maximum (V_{max}) and minimum voltage (V_{min}):* in regions 3,4, and 5 the amplitude for each single applied pulse was computed. Then the amplitudes were averaged in each region separately. The units are in Volts (V).*

4. *The Fourier transform (FFT):* the FFT for all the regions was calculated to check any change in the amplitude of the frequency components upon electrical and ultrasound stimulation.*

7.2.6. Experiments

Each stimulation combination listed in table 7.6 was recorded based on the criterion shown in figure 7.26 where R1, 2, 3, 4, and 5 represent the regions explained in the previous section. This scheme allows us to compare every recording to itself. The electrical stimulation time is greater than the US stimulation time in region R2 to ensure the consistency of the EMG recording while in region R4 to observe if there was recovery from the US stimulation effect.

Pre-stimulus	Electrical	US + Electrical	Electrical	Post-stimulus
10 secs	20 secs	10 secs	20 secs	10 secs
	stimulus	Stimulus	stimulus	
R1	R2	R3	R4	R5
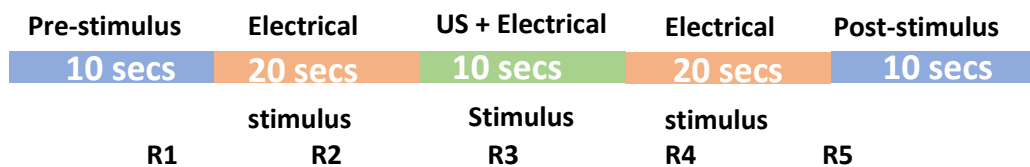
Figure 7.26: Stimulation Criterion

The experiments were conducted as described in the previous sections. The stimulation parameters combinations were randomized, and each was repeated 3 times in each experiment. Moreover, few recordings were obtained with electrical stimulation only (no US) for analysis and comparison reasons only. It is important to mention that not all the combinations were recorded in all the experiments. Table 7.7 details the conducted experiments along with the recorded combinations and total recorded files in each experiment.

Table 7.7: Experiments Conducted

Experiment	Rat Weight (g)	US frequencies (kHz)	US Intensities (W/cm^2)	Electrical Intensities (V)	Total recordings
1	470	200	9.34	2.5, 5, 7	30
		500	11.1		
		700	17.51		
2	490	200	9.34	2.5, 5, 7	30
		500	11.1		
		700	17.51		
3	360	200	9.34 4.16 2.58	2.5, 5, 7	90
		500	11.1 6.06 5.04		
		700	17.51 5.65 2.83		
4	386	200	9.34 4.16	5	21
		500	11.1 6.06		
		700	17.51 5.65		

7.2.7 Statistical Analysis

The recorded EMG files and observed outcomes were grouped based on the stimulation parameters combination. Paired t-tests were then conducted with a confidence interval of

95% to study if the effect of US stimulation and the changes in the recorded outcomes were significant or not.

7.2.8 IR Camera Recordings

During experiment 4 of table 7.7, an intra-red (IR) camera was used to observe the changes in the temperature as electrical and US stimulation were applied. The videos and screen shots were recorded when electrical stimulation had an amplitude of 5V, US stimulation had intensities and frequencies shown in table 7.8 (total of 3 videos)

Table 7.8: Intensities and Frequencies of US stimulation for IR videos

US frequencies (kHz)	US Intensities (W/cm^2)
200	4.16
500	6.06
700	5.65

7.2.9 Histology

Histological Analysis was conducted. The sciatic nerve was stained with anti-neurofilament 200 and Alexa 568 fluorophores.

Table 7.9 summarizes the devices used in this project.

Device	Provider	Model
3D Printer	FormLabs	Form 2
Bio-amplifier	World Precision Instruments	ISO-80
Data acquisition Board (Profile)	National Instruments	Elvis III
Data acquisition Device	Cambridge Electronic Devices	Power 3-1401
Hydrophone	Onda	HNR-0500
IR Camera	FLIR	E40
Isolator	Grass	SIU5
Motorized Axes System	Velmex	X-slide
Oscilloscope	Siglent	SDS 1202X
RF amplifier	Hewlett Packard (HP)	8347A
Stimulator	Grass	S44
US transducer	Manna Instruments	E1012-SU
Waveform Generator	Siglent	SDG 2042X
Sonicator	Branson	2800

CHAPTER 8

RESULTS ANIMAL MODEL

8.1 US Transducer Characterization

We characterized the US transducer by scanning a $20\times20\times20$ voxels, $40\times 40\times40$ mm cubic volume in front of transducer in a bath of degassed, deionized, and double distilled water. The input signal to the US transducer was a pulsed signal with frequency of 500 kHz, burst period 11 ms, and 5000 cycles. The waveform generator voltage (V_{wv}) was set to 0.5 V_{pp}, and RF amplifier gain at 20dBm. This resulted in an input voltage at the transducer of 13.84 V. The developed 4D heat map is shown in figure 8.1 with the US signal propagating in the y direction. Acoustic intensities in the grid ranged from 2.7 to 54 W/cm^2 with the highest intensities in a cylindrical volume at the center of the transducer. The maximum intensity (54 W/cm2) was in plane 11. Figures 8.2 and 8.3 represent 4D plots of plane 11. The plots show that two maxima exist, at distances 4 and 10 mm away from the face plate of the transducer center. Since the first peak at 4 mm is too small, we used the second maxima, 10 mm, to design the coupling cone height.

The acoustic profile shown in figures 8.1, 8.2, and 8.3 is at a frequency 500 kHz. The same distribution was also obtained at 200 and 700 kHz.

After designing and printing the coupling cone, US gel, of density 983kg/m^3 and ultrasonic speed 1516 m/sec, was added in the cone and the acoustic intensity was measured and computed at the tip of the cone. The US signal traveled successfully in the coupling cone and the measured acoustic intensities are shown in table 8.1.

4D Plot of Intensities in Scanned Cubic Volume
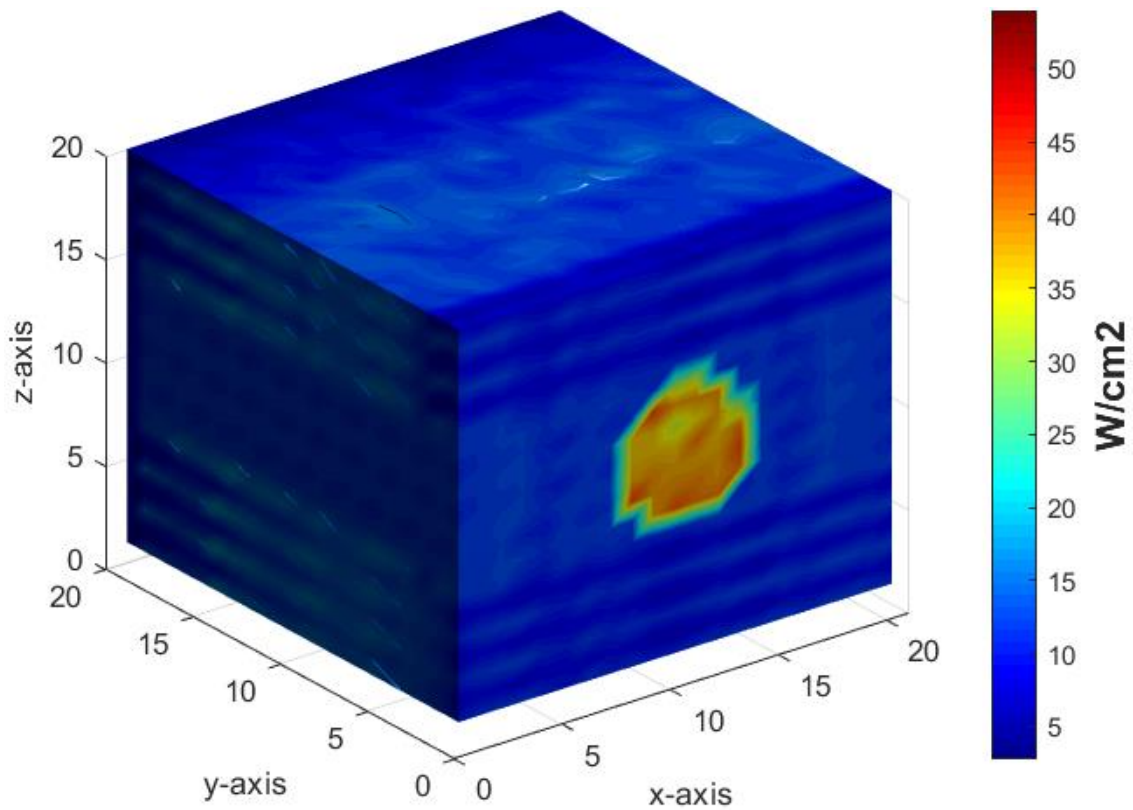
Figure 8.1: Heat map for acoustic profile: The acoustic intensity varies in the volumetric shape scanned. The plot have 4 dimensions: 3 dimensions of x,y, and z location; and a fourth dimension: the acoustic intensity value indicated with a color scale. The US transducer is oriented parallel to the x-axis, in the center of the xz planes, and the US signals propagate in the y-direction. As the color changes from navy blue to hot red, the acoustic intensity increases. The figure shows that the highest intensities are in front of the transducer in almost a circular shape in each xz plane while the intensity drops to almost zero in the surrounding of the transducer. The 4D plot does not allow to show the distribution inside the volume, yet the distribution obtained showed that the US waves travel in the y direction forming a unique cylinder with intensities varying and much higher than the surrounding volume. The cylinder spans the distances between x=7 and 14 (6 voxels), y= 0 to 21 (20 voxels), and z=7 and 13. The scale bar on the right shows that intensities higher than 50 are observed, yet they don't appear in this plot since they occur at z=11, x=10, and y= 2 and 5.

Figure 8.2: 3D plot of plane z=11: The 3D plot shows the distribution of the acoustic intensity in plane z=11, with the first 2 dimensions being the location (x abscissa and y ordinate) and the 3rd dimension being the intensity varying both in color intensity and along the z axis of the plot and not the volumetric shape scanned. The transducer is placed parallel to the x-axis and the US signal propagating in the y- direction. Two sharp peaks are observed and indicated by peak 1 and 2, by the intense red color, and by the maximum height on the z axis of the plot. As we move away from the face plate of the transducer, or as y increases, the intensity drops.

3D Plot of intensities in plane z=11 and x=10
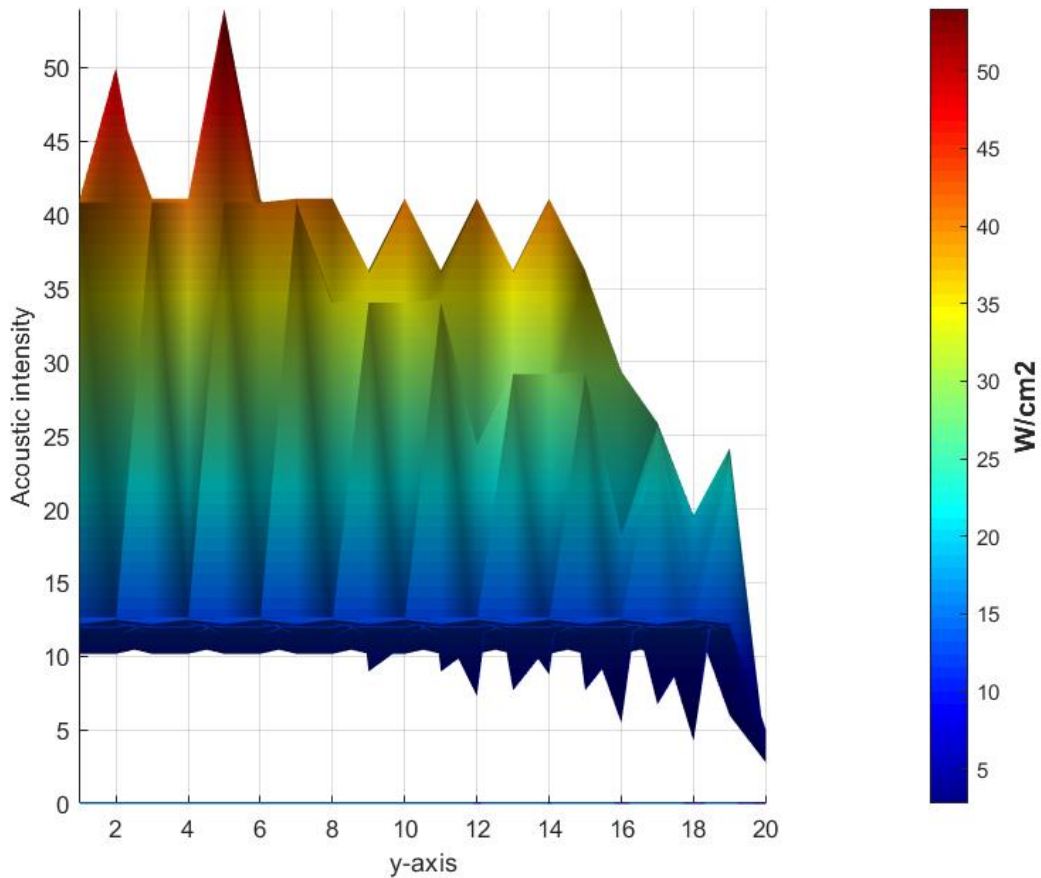
Figure 8.3: 3D plot of plane z=11, x=10 (Y plane): The 3D plot shows the distribution of the acoustic intensity in plane z=11 and x=10. The transducer is placed to the left of the plot and the US signal propagating in the y- direction. Two sharp peaks are observed at y= 2 and 5 units. Each unit is 2mm (motorized axes are programmed to advance 2mm). Therefore, the peaks are at 4mm and 10 mm from the center of the face plate of the transducer. As we move away from the face plate of the transducer, or as y increases, the intensity drops

Table 8.1: Acoustic Intensity at the tip of US transducer and coupling cone

Frequency (kHz)	V at transducer Input (V)	Acoustic intensity (W/cm^2)
	18.2	9.3451
200	8.4	4.1620
	2.84	2.5850
	13.8	11.1023
500	6.8	6.0646
	2.84	5.0483
	12	17.5155
700	6.9	5.6513
	2.96	2.8387

Measurements show that the acoustic intensity decreased as the input electrical signal to the transducer decreased. Also, an increase in the intensity was observed as the US frequency increased.

8.2 US Stimulation of the Sciatic Nerve

8.2.1 Latency and AUC of EMG response (No US)

The amplitude, area under the curve (AUC), latency and FFT of the recorded EMG signals from the gastrocnemius muscle were analyzed. First the variation of the AUC upon electrical stimulation only was studied. Figures 8.4 and 8.5 show that the AUC increased as the electrical stimulation increased from 2.5 V to 7.5 V, while the latency decreased.
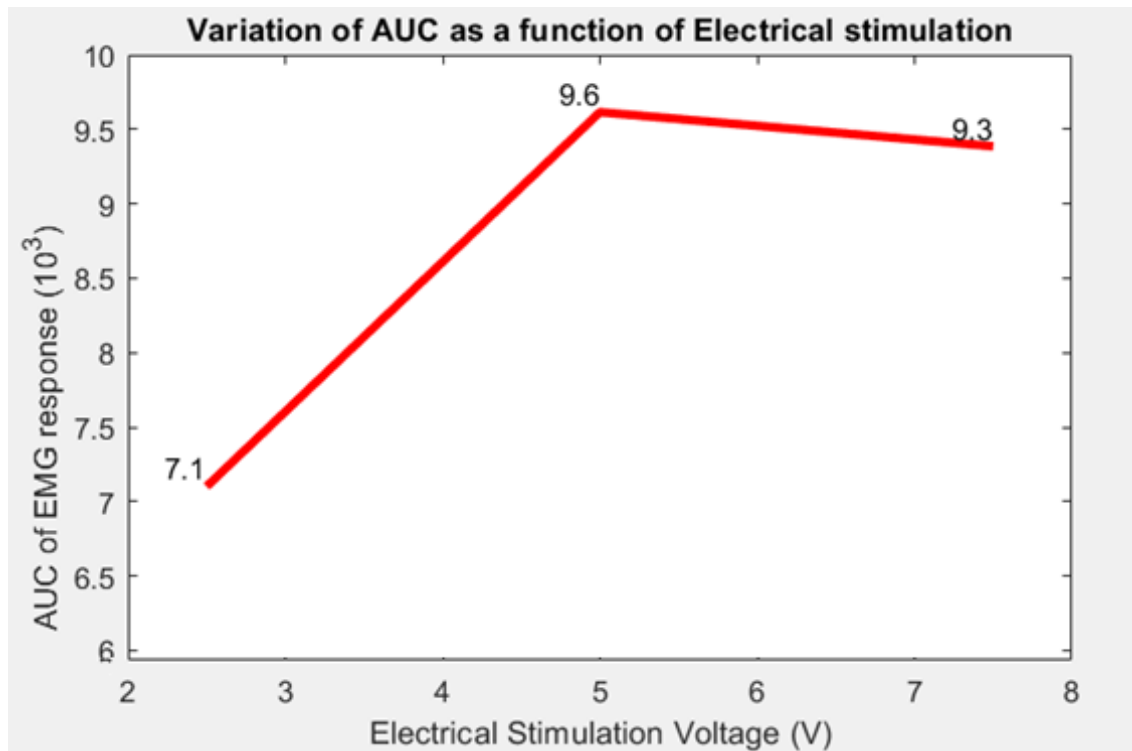
Figure 8.4: Variation of AUC as a function of electrical stimuli intensity: The AUC increases from 7100 mV^2/s to 9600 mV^2/s as the electrical stimulation increases from 2.5 to 5 V, 2ms duration, and 10 pulses per sec (10 Hz). The AUC drops slightly to 9300 mV^2/sec when the electrical stimulation further increases to 7.5 V indicating saturation or recruitment of all muscle fibers with no possibility of a further recruitment or increase in AUC
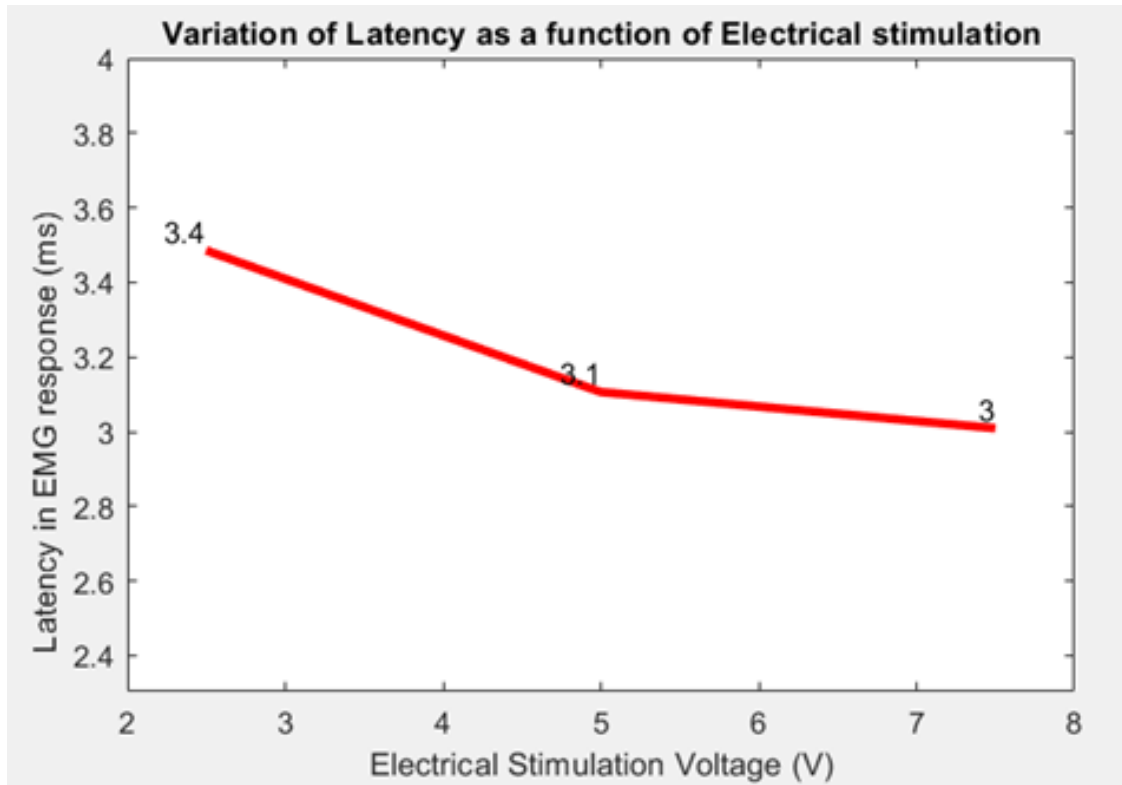
Figure 8.5: Variation of latency as a function of electrical stimuli intensity: As the intensity of the electrical stimuli increases, the latency drops, and the muscle fibers respond faster to stimuli. This is reflected in the decreases in latency from 3.4 ms to 3.1 as the electrical stimulation increases from 2.5 to 5 V, 2ms duration, and 10 pulses per sec (10 Hz). Latency drops slightly to 3 ms when the electrical stimulation further increases to 7.5 V.

8.2.2 Latency, Amplitude, and AUC of EMG response upon US stimulation

The dependency of the EMG amplitude on the electrical stimulation made it difficult to isolate the US effect, which lead to normalizing the change in amplitude and AUC to observe and analyze the percentage change upon US stimulation, comparing these outcomes between: (1) regions R2 and R3, and (2) regions R2 and R4. Upon applying US stimulation for 3 different rats as shown in table 4.7, figure 8.6 shows the variation in the change in amplitude of EMG response as a function of US frequency. The figure shows that US was successful in decreasing muscle activity. The drop in amplitude had a greater magnitude in lower frequencies (200 and 500 kHz) than higher one (700 kHz) and the US

effect remained after the US stimulation was removed. As for figure 8.7, the drop in AUC was also observed in lower frequencies than higher ones and is maintained post US stimulation.
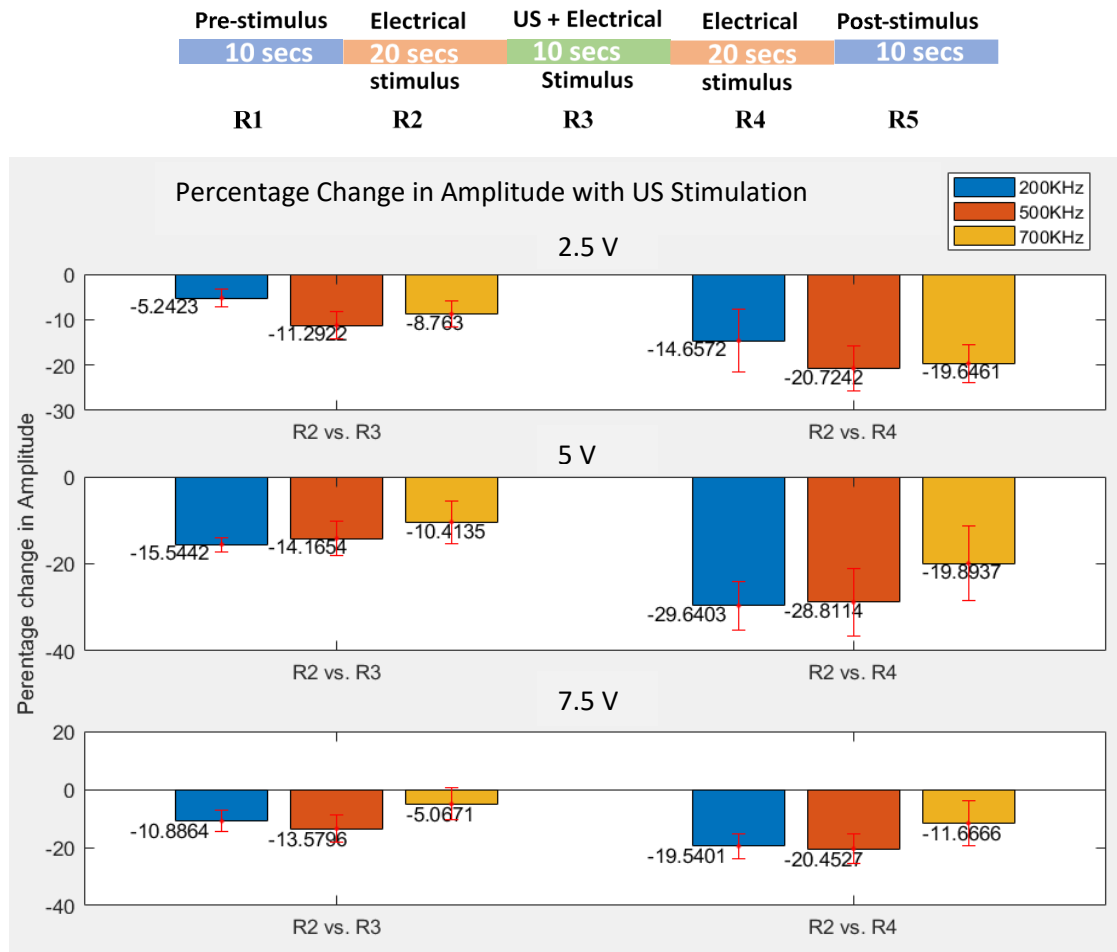
Figure 8.6: Variation of EMG amplitude upon US stimulation: The figure shows the percentage change in amplitude of EMG response upon US stimulation (R2 vs R3) and post-US stimulation (R2 vs R3). The amplitude drops upon US stimulation of 200 kHz (blue), 500 kHz (orange), and 700 kHz (yellow). The effect remains post US stimulation with the drop in amplitude observed with larger magnitudes post US than during US when compared to pre-US stimulation. The change in amplitude shows that lower frequencies (200 and 500 kHz) are more successful in suppressing EMG responses than higher frequencies (700 kHz). Results are consistent for all electrical stimuli (2.5, 5 and 7.5 V).
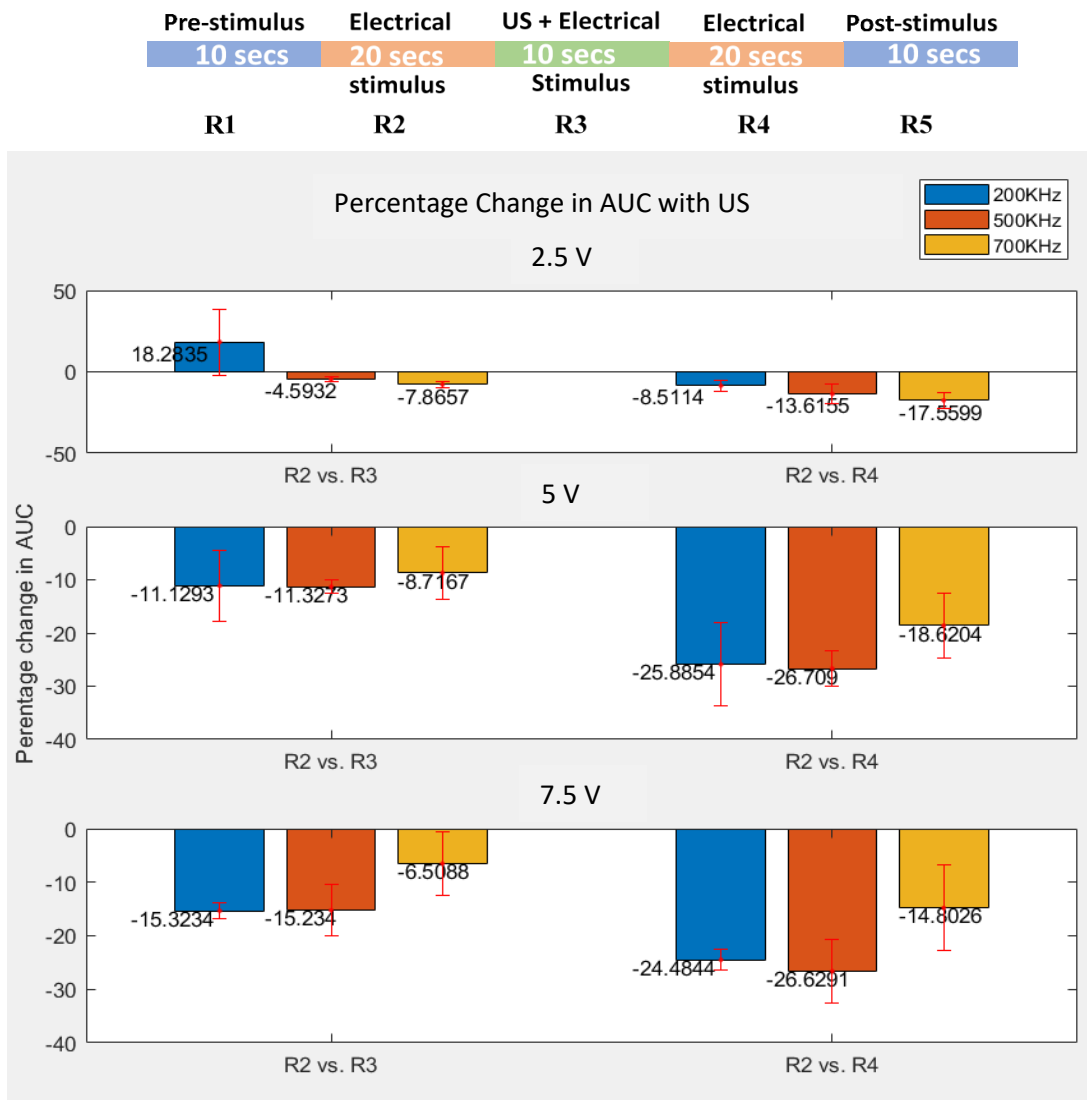
Figure 8.7: Variation of EMG AUC upon US stimulation: The figure shows the percentage change in AUC of EMG response upon US stimulation (R2 vs R3) and post-US stimulation (R2 vs R3). The AUC drops upon US stimulation of 200 kHz (blue), 500 kHz (orange), and 700 kHz (yellow). The effect remains post US stimulation with the drop in AUC observed with larger magnitudes post US than during US when compared to pre-US stimulation. The change in AUC shows that lower frequencies (200 and 500 kHz) are more successful in suppressing EMG responses than higher frequencies (700 kHz). Results are consistent for all electrical stimuli (2.5, 5 and 7.5 V).

The paired t-test studying the difference in means between the amplitude and AUC between: (1) R2 and R3, and (2) R2 and R4, showed that the difference of the means was significant with a confidence interval of 95% and p-value< 0.001 for pair (1) and <0.0001

for pair (2). This shows that the changes observed due to US stimulation were also statistically significant. On the other hand, results showed that US stimulation had no significant effect on latency of EMG responses. Changes in Latency are shown in table 8.2.

Table 8.2: Latency in regions R2, R3, and R4

Frequency (kHz)	Electrical Stimulus (V)	Latency Pre-US (ms) [R2]	Latency during US(ms) [R3]	Latency Post-US (ms) [R4]
200 (9.3451 W/cm²)	2.5	3.36	3.41	3.43
	5	3.49	3.46	3.24
	7.5	3.21	3.19	3.12
500 (11.1023 W/cm²)	2.5	3.51	3.57	3.63
	5	3.24	3.27	3.3
	7.5	3.25	3.22	3.25
700 (17.5155 W/cm²)	2.5	3.49	3.58	3.69
	5	3.11	3.11	3.15
	7.5	3	3.04	3.08

Pre-stimulus	Electrical	US + Electrical	Electrical	Post-stimulus
10 secs	20 secs stimulus	10 secs Stimulus	20 secs stimulus	10 secs
R1	R2	R3	R4	R5

8.2.3 FFT of EMG response upon US stimulation

US stimulation of frequencies 200, 500, and 700 kHz caused a reduction in the amplitudes of some frequency components of the FFT of the EMG response. Drops in these amplitudes were observed during US stimulation and post US stimulation. Partial recovery was observed in post US stimulus regions, but full recovery was never observed. To ensure than the change in the amplitude of the frequency components was due to US stimulation and is not a naturally occurring phenomena, we compared the FFT of an EMG response with only electrical stimulation. We divided the EMG response into 3 regions covering 20 seconds, 10 seconds, and 20 seconds of time to resemble the stimulation

scheme used with US stimulation. The FFT showed no drop or change in any frequency component validating that the change in the FFT spectrum is due to the US stimulation. An example of the drop in frequency components' amplitudes is shown in figures 8.8 and 8.9 presenting the EMG response without and with US stimulation, and figures 8.10 and 8.11 showing the variation in the FFT spectrum.
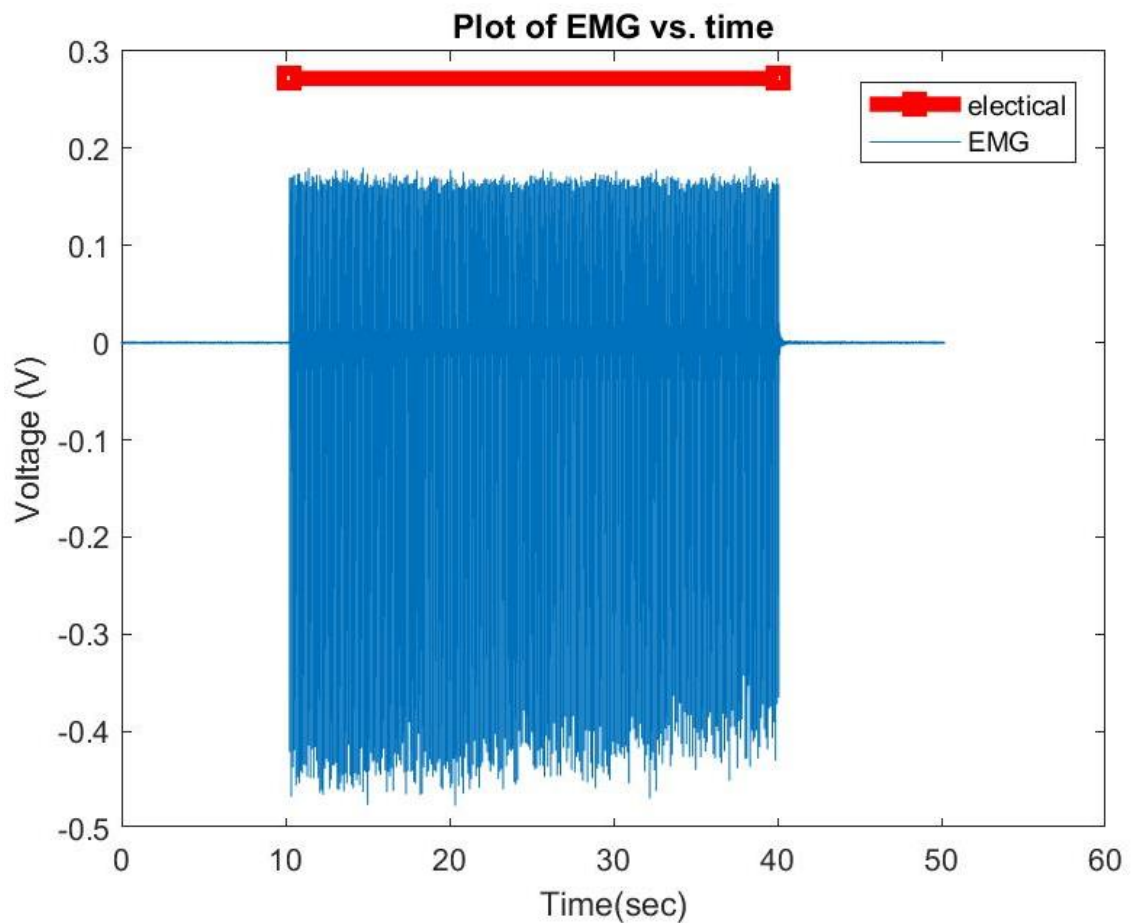
Figure 8.8: EMG response with 2V, 10 Hz electrical stimulation: The EMG response of the gastrocnemius muscle upon electrical stimulation of 2V, 10Hz, and 2ms pulse duration. The EMG amplitude is initially at zero Volts when no electrical stimulation is applied. The amplitude increases upon electrical stimulation and varies around 590 mV. This amplitude is post amplification via a bio amplifier of gain 100.
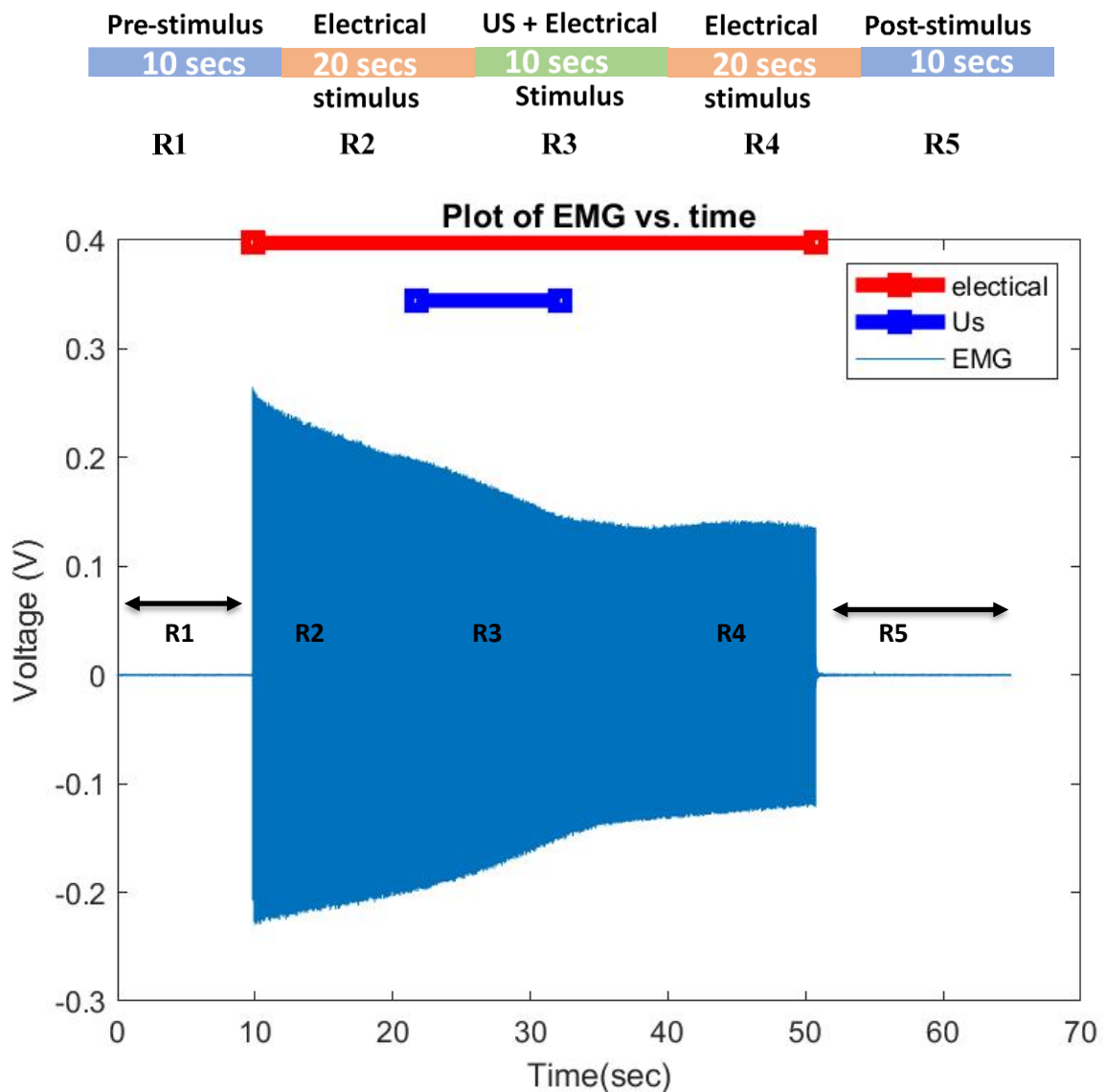
Figure 8.9: EMG response with 2V, 10 Hz electrical stimulation and 500 kHz (11W/cm^2) US stimulation: The EMG response of the gastrocnemius muscle upon electrical stimulation of 2V, 10Hz, and 2ms pulse duration and US stimulation of 500 kHz and 11 W/cm^2 acoustic intensity. The EMG amplitude is initially at zero Volts when no electrical or US stimulation are applied. The amplitude increases upon electrical stimulation (red time duration). Upon US stimulation (navy blue time duration) the EMG response further drops. The amplitude doesn't recover post US stimulation. Amplitudes range between 200 mV and 500 mV, with minimum post-US stimulation and max pre-US stimulation. This amplitude is post amplification via a bio amplifier of gain 100.
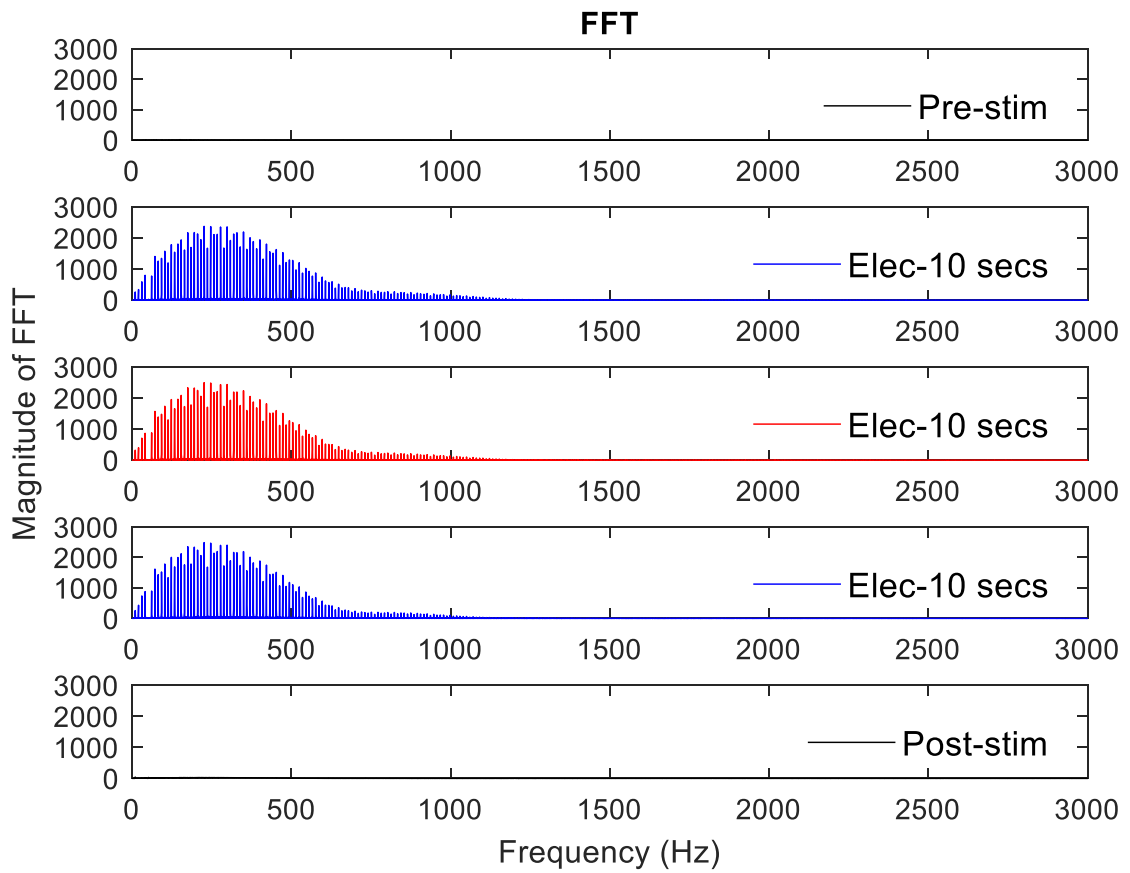
Figure 8.10: FFT of EMG response with 2V, 10 Hz electrical stimulation: The FFT of the EMG response of the gastrocnemius muscle upon electrical stimulation of 2V, 10Hz, and 2ms pulse duration and no US stimulation. The 30 seconds electrical stimulation duration is divided to 3 parts showing a consistency in the magnitude of all the frequency components dominant in the FFT.

Pre-stimulus	Electrical	US + Electrical	Electrical	Post-stimulus
10 secs	20 secs stimulus	10 secs Stimulus	20 secs stimulus	10 secs
R1	R2	R3	R4	R5
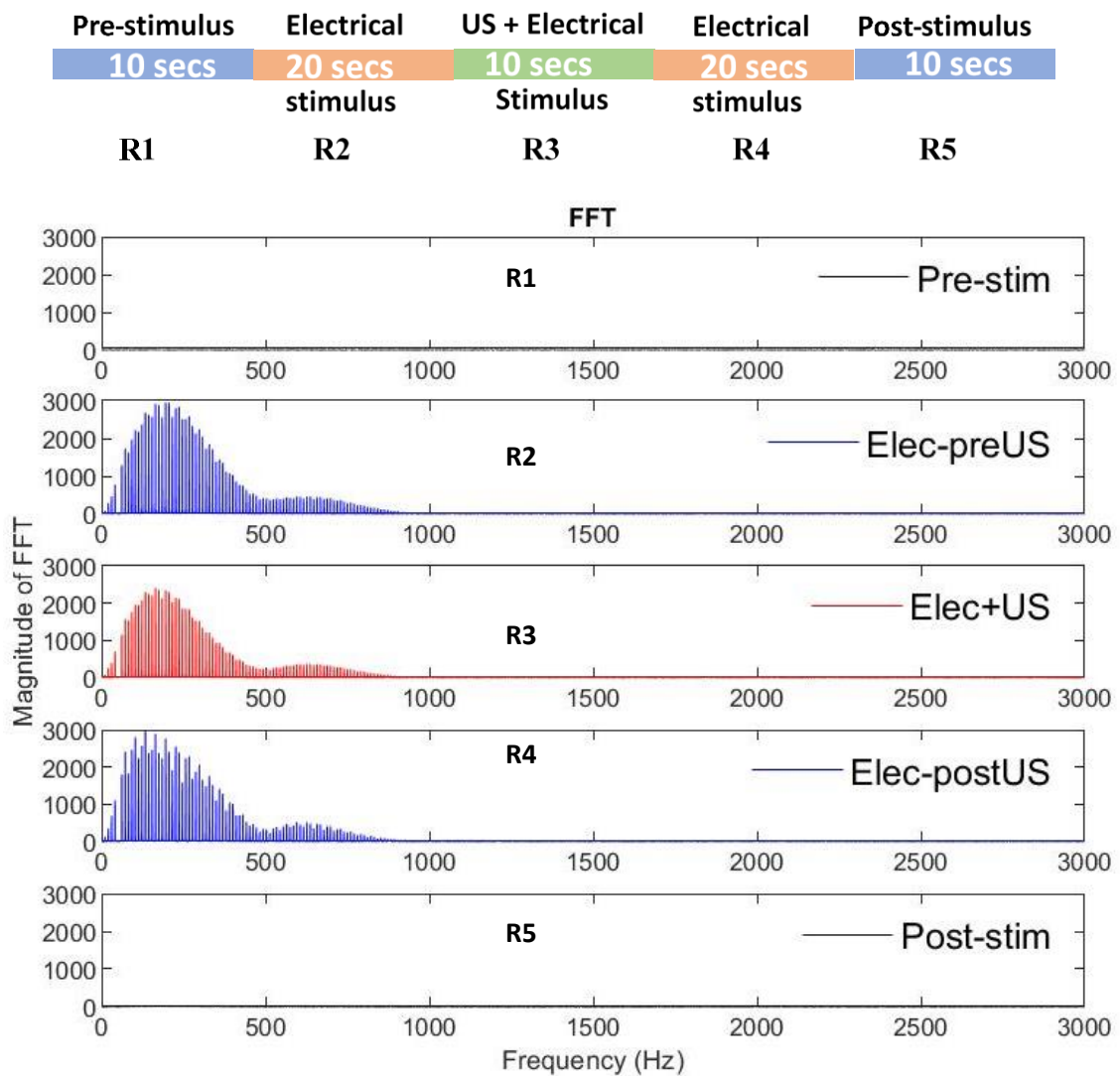
Figure 8.11: FFT of EMG response with 2V, 10 Hz electrical stimulation and 500 kHz (11W/cm^2) US stimulation: The FFT of the EMG response of the gastrocnemius muscle upon electrical stimulation of 2V, 10Hz, and 2ms pulse duration and US stimulation of 500 kHz. Pre-US stimulation frequency components have magnitudes between 0 and 3000. Upon US stimulation, the magnitudes drop to range between 0 and around 200. The change in frequency components is mainly in frequencies below 500 Hz. Post-US stimulation, some frequency components show a rise and recovery of the magnitudes observed pre-US stimulation, yet full recovery isn't observed.

We further analyzed the change in the FFT amplitudes by finding the global minimum amplitude among each recording followed by dividing all other amplitudes by the global minimum. The computed quotients had decimal values and not integers. This indicated

that the effect of US stimulation is restricted to attenuating the activity in each neuron and thereby muscle fibers and not an "on off" response that shuts neurons and muscle fibers completely.

8.2.4 AUC of EMG response upon US stimulation with different acoustic intensities

In attempt to explore more US intensities, we fix the electrical stimulation to 5V and vary the gain in the RF amplifier as mentioned earlier. Table 8.3 summarizes the intensities produced at the tip of the coupling cone and targeted at the sciatic nerve, and the drop in the AUC of the EMG response. Figure 8.12 showed the magnitude of the AUC drop as a function of acoustic intensity when the data is grouped into 4 categories based on the acoustic intensity: (1) 0 to 5 W/cm^2, (2) 5 to 10 W/cm^2, (3) 10 to 15 W/cm^2, and (4) 15 to 20 W/cm^2. The results show that the higher the acoustic intensity the smaller the magnitude of change of the AUC for the EMG when subject to US stimulation.

Table 8.3: Change in AUC of EMG response as a function of US stimulation intensity

US Frequency (kHz)	Intensity (W/cm2)	Change in AUC (%)
200	2.58	-18.82
	4.16	-18.69
	9.34	-11.37
500	5.05	-18.03
	6.06	-11.07
	11.1	-11.73
700	2.84	-13.42
	5.65	-11.35
	17.52	-7.63
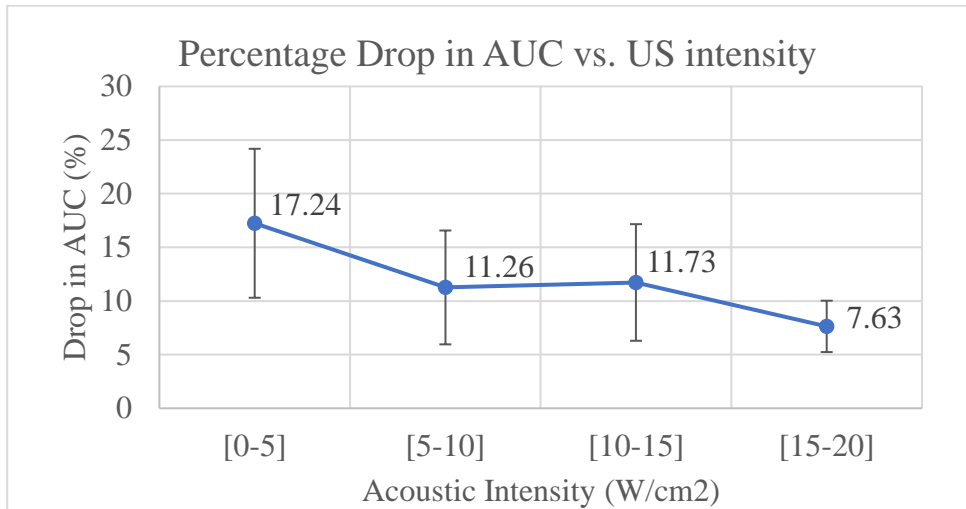
Figure 8.12: Variation in drop of AUC of EMG as a function of acoustic US intensity: The AUC drops when the sciatic nerve is subject to US stimulation. The effect of US stimulation is greater at lower intensities with a drop of around 17% for intensities below $5W/cm^2$, around 11% for intensities between 5 and 15 W/cm^2, and as low as around 7 % for intensities between 15 and 20 W/cm^2.

8.2.5 IR Camera Results

Videos and pictures taken during US stimulation showed no change in the temperature of the sciatic nerve or the surrounding area. Figure 8.13 shows an IR image. The temperature indicated on the top left was the maximum temperature observed in the image. To focus on the sciatic nerve, we adjust the settings of the camera to indicate the temperature at the nerve.
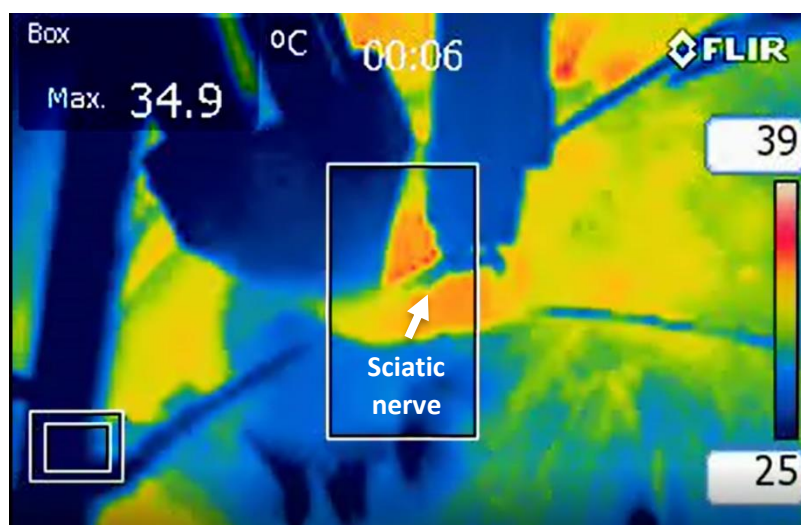
Figure 8.13: IR Image of the sciatic nerve during stimulation

Figure 8.14 (a) shows the temperature of the sciatic nerve when only electrical stimulation is applied (R2), 8.14 (b) shows the temperature when US stimulation is applied (R3), and 8.43 (c) when US stimulation is removed, and electrical stimulation is maintained (R4).
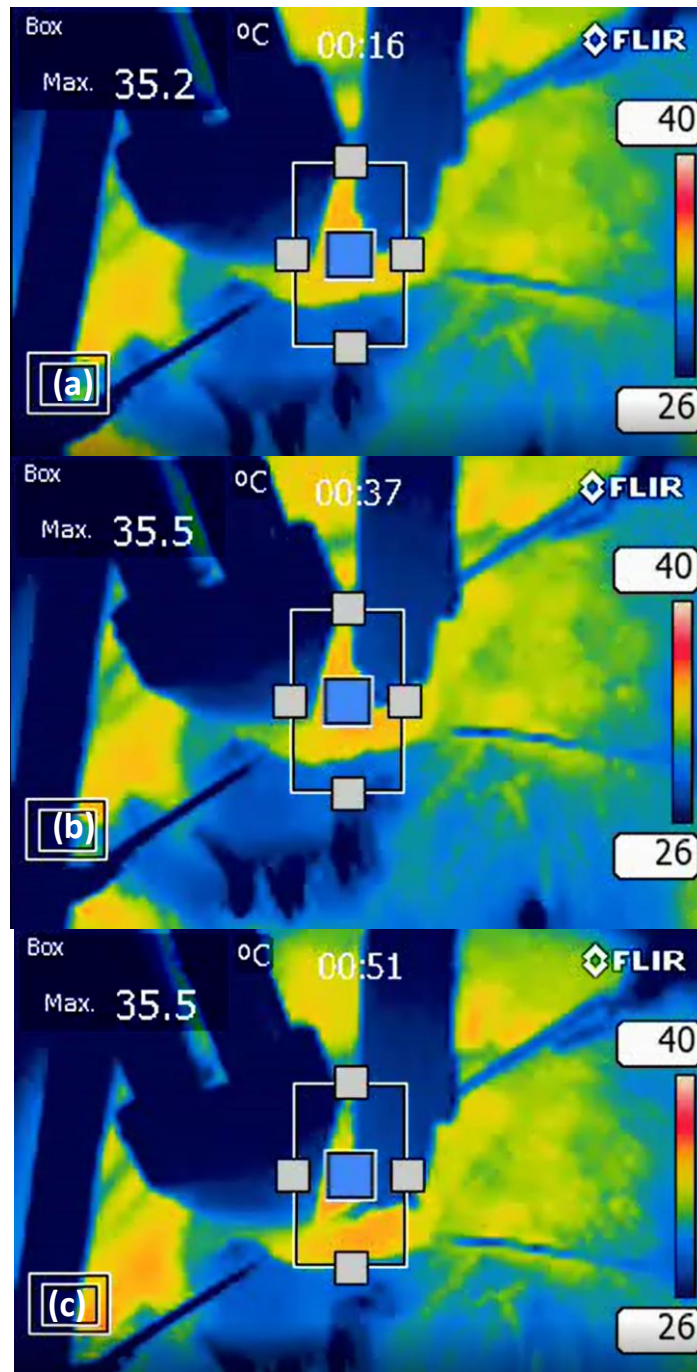
Figure 8.14: IR camera results pre-US (a), during US (b), and post-US (c). The maximum temperature at the sciatic nerve varies between 35.2 and 35.5^{0}C showing that the US stimulation does not cause a temperature increase at the applied intensities and frequencies

8.2.6 Recovery from US stimulation

In order to ensure the reversibility of US neuromodulation and to ensure that the stimulation didn't cause nerve damage, we compare the baseline AUC of EMG recordings of same parameter. In other words, we randomly select an experiment and compare EMG recordings resulting from the same stimulation parameters combinations. Table 8.4 shows the average percentage variation in the baseline AUC for 3 recordings for each combination of stimulation parameters

Table 8.4: Average % change in baseline AUC

US Frequency (kHz)	Electrical Intensity (V)	Average % change in AUC of baseline
200	7	0.16
500	7	0.06
700	7	0.14
700	5	0.05
200	2	0.04

The above table shows that although the effect of US stimulations remains post US stimulation, recovery is then observed and no damage occurs due to the return of the AUC of the baseline (region R2) to the same value hen subjected to same stimulation parameters.

8.2.7 Histology Results

Histological analysis showed no degradation or injury in sciatic nerve. The neurofilaments were intact as shown via confocal imagining. Figure 8.15 shows a confocal image with 40× oil magnification.
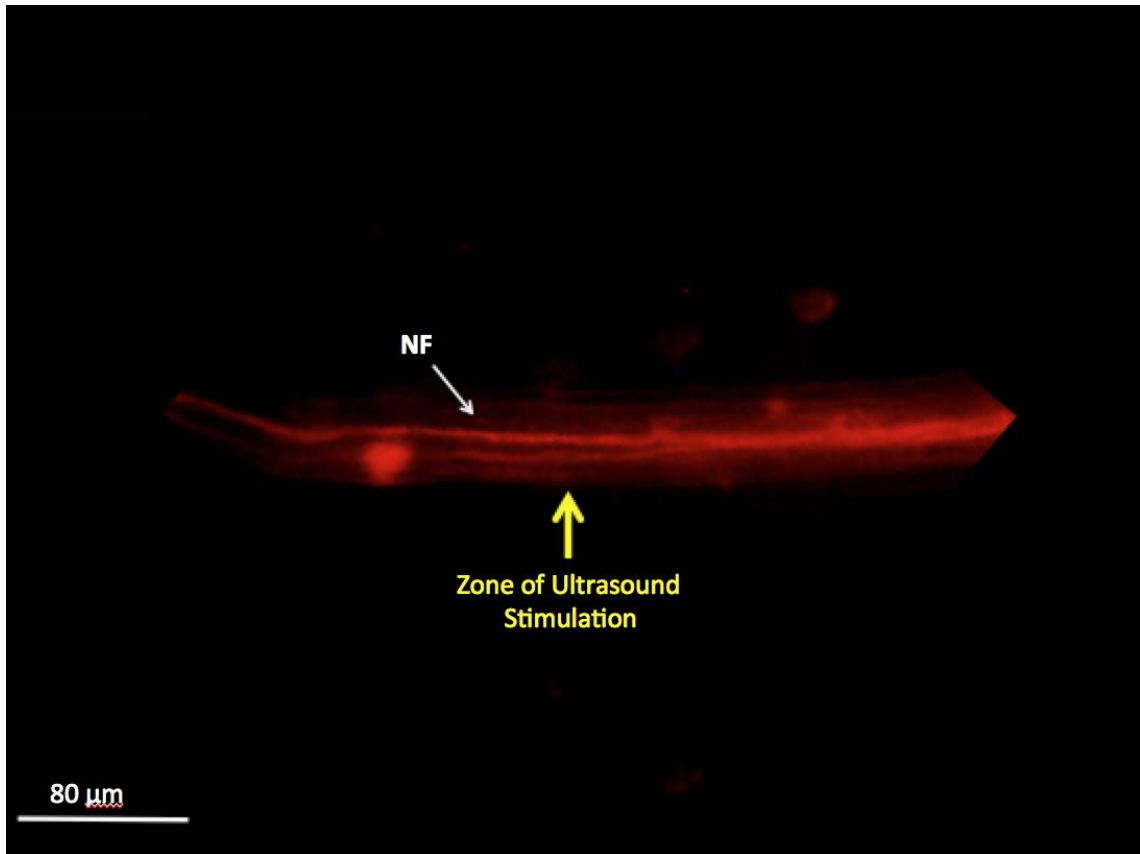
Figure 8.15: Confocal image with 40× oil magnification. No degradation or injury observed in the region subject to ultrasound stimulation

CHAPTER 9

DISCUSSION FOR ANIMAL MODEL

One of the intriguing and highly crucial things in the field of neuromodulation is the replacement of current invasive stimulation techniques with non-invasive ones. The ability of US waves to travel through tissue renders ultrasound stimulation an ideal non-invasive, high spatial and temporal resolution, and widely ranged parameters modality that showed success in altering neural behavior. In the area of diseases of the nervous system, US was used mainly to lesson symptoms of epilepsy, tremor, and Parkinson [24, 39-41, 43]. Moreover, US stimulation was applied to several targets in the CNS and elicited both excitatory and inhibitory responses [86, 99, 105, 131]. The mechanical stimulation modality was rarely studied in pain management which channeled our focus on exploring the ability of US stimulation to modulate neural behavior of networks involved in evoked motor potentials.

In this work, we characterized the immersible US transducer using a degassed deionized water tank and provided it with a coupling cone to guide US waves to stimulate the sciatic nerve. The transducer was capable of delivering US waves with higher intensities as the frequency increased and approached the center resonating frequency of the 1 MHz transducer. Electrical stimulation of the sciatic nerve evoked muscle potentials in the EMG recorded from the gastrocnemius muscle. These potentials increased with the intensity of the electrical stimuli, due to the recruitment of more muscle fibers, but where inhibited upon US stimulation. The elicited inhibitory effects of the US stimulation remained post stimulation for a minimum observed duration of 20 seconds, but recovery was observed later, ensuring that the lessoning of the muscle responses is not due to damage of the sciatic nerve and that US neuromodulation is reversible. The results agree

with published data and validate the ability of US stimulation to modulate neural activity and suppress evoked potentials [95, 99]. Upon US stimulation, muscle activity was reduced with greater effect at lower frequency which is associated to the natural behavior of higher frequency US waves in tissue that tend to diffract more than lower frequencies causing a reduction in their impact.

Although ultrasound stimulation was previously studied to explore its ability in neuromodulation, this work shows novelty in its target and experimental methods. The work is the first to focus on pain suppression by studying the reflex arc, and it is the first to study in vivo responses of the sciatic nerve through EMG recordings. As expected, and reported in literature [98, 99, 132], US stimulation showed a suppression of muscle responses deduced from the drop in amplitudes and AUC of the EMG response.

The higher success of lower intensities of US stimulation gives rise to questions on the magnitude of threshold intensities required to observe modulatory behaviors and opens doors for further experiments to explore lower intensity ranges. Also, it shows the possibility of a saturation in the responses since above an intensity of 5 W/cm^2, drops in amplitudes and AUC remained almost consistent with no thermal effects or nerve damage. On the other hand, US stimulation intensities explored in this work did not affect the temperature of the sciatic nerve. US stimulation with intensities in the order of magnitude of 10^3 causes damage, due to thermal effects, of the targeted tissue. Therefore, this study is limited to a range of intensities that does not set the boundaries for minimum, saturation, and maximum intensities that result in modulatory or destructive effects.

Finally, the work can be further developed by identifying whether US stimulation affects the afferent or efferent pathways bundled & stimulated simultaneously in sciatic nerve, through studying M and H-waves in the EMG response.

To conclude, the work done in this thesis is divided into two parts, one that studies the effect of ultrasound stimulation and other mechanical forces theoretically, via computational modeling, and the seconds, studies the same effects on a pain pathway, via animal experiments. The two aims are inter-related since they both explore ultrasound effects either on a single neuron, in the computational model, or on a nerve bundle, in the animal experiments. Although the computational model explores neural activity amplitudes and firing rates, and the animal experiments studies muscle activity, yet the muscle studied is controlled and in direct relationship with the nerve subject to ultrasound stimulation.

CHAPTER 10

CONCLUSION & FUTURE PROSPECTIVE

In this thesis, we focused on the impact of low frequency ultrasound stimulation on neural excitability. First, we characterized an immersible US transducer and used it as a stimulation tool to modulate the responses of the sciatic nerve to intense electrical stimulus or pain sensation. We recorded muscle activity from fibers controlled by this nerve and showed that US stimulation can suppress neural activity which is deduced from the decrease in EMG response. Experiments also verified the US effect through changes in FFT spectrum. Experimental results agree with several published works [95, 98, 99, 132]. The mechanism of action of US stimulation remains unknown, but IR camera heat recordings confirmed that heating is not the reason behind neural modulation. To further understand the mechanism, we developed a computational model that incorporates mechanical forces induced due to ultrasound stimulation into the HH electrical model. The model explored frequencies ranging from 250 kHz to 750 kHz and intensities from few mW/cm^2 to few 100 kW/cm^2. The simulation results of our model are in agreement with published experimental, and not computational, data when it comes to the effect of lower frequencies and intensities of US stimulation on neural firing [95, 98, 99, 132]. The model showed suppression of action potential amplitudes and large variations in firing rates, but minimal effects on latency.

The novelty in this thesis is not only in developing the first model of its kind that studies the effect of biomechanical forces on electrical stimulus; but also in conducting in vivo experiment on the sciatic nerve to observe the effect of US on neural excitability and explore the possibility of ultrasound, an imaging modality, as a stimulation modality for chronic pain suppression.

Future work involving the animal experiments conducted in this work must include exploring further US stimulation intensities and different sonication durations. On the other hand, further targets, involved in the pain experience, can be studied including stimulation of the spinal cord and deep regions in the brain, namely the periaqueductal grey. On the other hand, the computational model studies the US effect on a single neuron and not a network of neurons or nerve bundle. Therefore, future work must include further development and compartmentalization to study the effect of US stimulation on a nerve fiber or a neural network. Temperature variation due to US intensities can be incorporated in the model to define the US intensity limits that might cause damage to the neuron. Also, further validation of the model can be conducted via experimental tools such as single cell patch clamp experiments where the dynamics of ion channel activation in response to US stimulation can be monitored.

BIBLIOGRAPHY

[1]   R.-D. Treede, "The International Association for the Study of Pain definition of pain: as valid in 2018 as in 1979, but in need of regularly updated footnotes," *Pain reports,* vol. 3, no. 2, 2018.

[2]   T. F. Almeida, S. Roizenblatt, and S. Tufik, "Afferent pain pathways: a neuroanatomical review," *Brain research,* vol. 1000, no. 1-2, pp. 40-56, 2004.

[3]   I. o. M. C. o. Pain and C. I. Behavior, *Pain and Disability: Clinical, Behavioral, and Public Policy Perspectives*. National Academies Press, 1987.

[4]   (December 4). *Basic Medical Key*. Available: https://basicmedicalkey.com/pain-3/#s0030

[5]   E. L. Garland, B. Froeliger, F. Zeidan, K. Partin, and M. O. Howard, "The downward spiral of chronic pain, prescription opioid misuse, and addiction: cognitive, affective, and neuropsychopharmacologic pathways," *Neuroscience & Biobehavioral Reviews,* vol. 37, no. 10, pp. 2597-2607, 2013.

[6]   R. K. Portenoy, "Current pharmacotherapy of chronic pain," *Journal of pain and symptom management,* vol. 19, no. 1, pp. 16-20, 2000.

[7]   E. Wood, D. L. Simel, and J. Klimas, "Pain Management With Opioids in 2019-2020," *Jama,* pp. 1-3, 2019.

[8]   R. G. Heath, "DEVELOPMENTS TOWARD NEW PHYSIOLOGIC TREATMENTS IN PSYCHIATRY," *Journal of neuropsychiatry,* vol. 5, pp. 318-331, 1964.

[9]   K. Kumar, C. Toth, and R. K. Nath, "Deep brain stimulation for intractable pain: a 15-year experience," *Neurosurgery,* vol. 40, no. 4, pp. 736-747, 1997.

[10] S. G. Boccard, E. A. Pereira, L. Moir, T. Z. Aziz, and A. L. Green, "Long-term outcomes of deep brain stimulation for neuropathic pain," *Neurosurgery,* vol. 72, no. 2, pp. 221-231, 2012.

[11] T. Tsubokawa, Y. Katayama, T. Yamamoto, T. Hirayama, and S. Koyama, "Chronic motor cortex stimulation for the treatment of central pain," in *Advances in Stereotactic and Functional Neurosurgery 9*: Springer, 1991, pp. 137-139.

[12] P. Verrills, C. Sinclair, and A. Barnard, "A review of spinal cord stimulation systems for chronic pain," *Journal of pain research,* vol. 9, p. 481, 2016.

[13] J. Dewey, "The reflex arc concept in psychology," *Psychological review,* vol. 3, no. 4, p. 357, 1896.

[14] !!! INVALID CITATION !!! [4-7].

[15] M. Rigaud *et al.*, "Species and strain differences in rodent sciatic nerve anatomy: implications for studies of neuropathic pain," *Pain,* vol. 136, no. 1-2, pp. 188-201, 2008.

[16] M. A. Shampo and R. A. Kyle, "Karl Theodore Dussik—pioneer in ultrasound," in *Mayo Clinic proceedings*, 1995, vol. 70, no. 12, p. 1136: Elsevier.

[17] E. Tohno, D. O. Cosgrove, J. P. Sloane, and E. Vagios, "Ultrasound diagnosis of breast diseases," 1994.

[18] P. Mishra and Z. M. Younossi, "Abdominal ultrasound for diagnosis of nonalcoholic fatty liver disease (NAFLD)," *The American journal of gastroenterology,* vol. 102, no. 12, p. 2716, 2007.

[19] D. Farine, H. E. Fox, S. Jakobson, and I. E. Timor-Tritsch, "Vaginal ultrasound for diagnosis of placenta previa," *American journal of obstetrics and gynecology,* vol. 159, no. 3, pp. 566-569, 1988.

[20] W. Lee *et al.*, "Image-guided focused ultrasound-mediated regional brain stimulation in sheep," *Ultrasound in medicine & biology,* vol. 42, no. 2, pp. 459-470, 2016.

[21] J. L. Foley, J. W. Little, and S. Vaezy, "Image-guided high-intensity focused ultrasound for conduction block of peripheral nerves," *Annals of biomedical engineering,* vol. 35, no. 1, pp. 109-119, 2007.

[22] W. Lee, H. Kim, Y. Jung, I.-U. Song, Y. A. Chung, and S.-S. Yoo, "Image-guided transcranial focused ultrasound stimulates human primary somatosensory cortex," *Scientific reports,* vol. 5, p. 8743, 2015.

[23] D. Schlesinger, S. Benedict, C. Diederich, W. Gedroyc, A. Klibanov, and J. Larner, "MR-guided focused ultrasound surgery, present and future," *Medical physics,* vol. 40, no. 8, 2013.

[24] N. Lipsman *et al.*, "MR-guided focused ultrasound thalamotomy for essential tremor: a proof-of-concept study," *The Lancet Neurology,* vol. 12, no. 5, pp. 462-468, 2013.

[25] A. Carovac, F. Smajlovic, and D. Junuzovic, "Application of ultrasound in medicine," *Acta Informatica Medica,* vol. 19, no. 3, p. 168, 2011.

[26] A. Fenster, D. B. Downey, and H. N. Cardinal, "Three-dimensional ultrasound imaging," *Physics in medicine & biology,* vol. 46, no. 5, p. R67, 2001.

[27] G. R. Lockwood, J. R. Talman, and S. S. Brunke, "Real-time 3-D ultrasound imaging using sparse synthetic aperture beamforming," *IEEE transactions on ultrasonics, ferroelectrics, and frequency control,* vol. 45, no. 4, pp. 980-988, 1998.

[28] P. Hodges, L. Pengel, R. Herbert, and S. Gandevia, "Measurement of muscle contraction with ultrasound imaging," *Muscle & nerve,* vol. 27, no. 6, pp. 682-692, 2003.

[29] C. Kasai, K. Namekawa, A. Koyano, and R. Omoto, "Real-time two-dimensional blood flow imaging using an autocorrelation technique," *IEEE Transactions on sonics and ultrasonics,* vol. 32, no. 3, pp. 458-464, 1985.

[30] E. D. Sullivan, D. J. Peter, and J. J. Cranley, "Real-time B-mode venous ultrasound," *Journal of vascular surgery,* vol. 1, no. 3, pp. 465-471, 1984.

[31] M. Wang, Y. Lei, and Y. Zhou, "High-intensity focused ultrasound (HIFU) ablation by the frequency chirps: Enhanced thermal field and cavitation at the focus," *Ultrasonics,* vol. 91, pp. 134-149, 2019.

[32] S. L. J. Júnior, G. L. Camanho, A. C. F. Bassit, A. Forgas, S. J. Ingham, and R. J. Abdalla, "Low-intensity pulsed ultrasound accelerates healing in rat calcaneus tendon injuries," *journal of orthopaedic & sports physical therapy,* vol. 41, no. 7, pp. 526-531, 2011.

[33] C. Zheng *et al.*, "Low-intensity pulsed ultrasound attenuates cardiac inflammation of CVB 3-induced viral myocarditis via regulation of caveolin-1 and MAPK pathways," *Journal of cellular and molecular medicine,* vol. 23, no. 3, pp. 1963-1975, 2019.

[34] D. Ensminger, *Ultrasonics: The low-and high-intensity applications*. M. Dekker, 1973.

[35] J. E. Kennedy, "High-intensity focused ultrasound in the treatment of solid tumours," *Nature reviews cancer,* vol. 5, no. 4, p. 321, 2005.

[36] K. G. Baker, V. J. Robertson, and F. A. Duck, "A review of therapeutic ultrasound: biophysical effects," *Physical therapy,* vol. 81, no. 7, pp. 1351-1358, 2001.

[37] A. Dupré, D. Melodelima, D. Pérol, Y. Chen, J. Vincenot, and M. Rivoire, "Intra-operative high intensity focused ultrasound for fast and large volume liver ablation. preliminary results of a Phase II Study," *HPB,* vol. 20, p. S368, 2018.

[38] S. B. Devarakonda, K. Stringer, M. B. Rao, M. R. Myers, and R. K. Banerjee, "ASSESSMENT OF ENHANCED THERMAL EFFECT DUE TO GOLD NANO-PARTICLES DURING MR-GUIDED HIGH INTENSITY FOCUSED ULTRASOUND (HIFU) PROCEDURES USING A MOUSE-TUMOR MODEL," *ACS Biomaterials Science & Engineering,* 2019.

[39] M. Ranjan *et al.*, "Neuromodulation beyond neurostimulation for epilepsy: scope for focused ultrasound," *Expert review of neurotherapeutics,* no. just-accepted, 2019.

[40] B.-K. Min *et al.*, "Focused ultrasound-mediated suppression of chemically-induced acute epileptic EEG activity," *BMC neuroscience,* vol. 12, no. 1, p. 23, 2011.

[41] S. Moosa, R. Martínez-Fernández, W. J. Elias, M. del Alamo, H. M. Eisenberg, and P. S. Fishman, "The role of high-intensity focused ultrasound as a symptomatic treatment for Parkinson's disease," *Movement Disorders,* vol. 34, no. 9, pp. 1243-1251, 2019.

[42] A. Sinai *et al.*, "Magnetic resonance–guided focused ultrasound thalamotomy for essential tremor: a 5-year single-center experience," *Journal of neurosurgery,* vol. 1, no. aop, pp. 1-8, 2019.

[43] E. L. Mazerolle *et al.*, "Focused ultrasound resolves persistent radiosurgery related change in a patient with tremor," *Radiology case reports,* vol. 14, no. 10, pp. 1233-1236, 2019.

[44] A. H. Mesiwala *et al.*, "High-intensity focused ultrasound selectively disrupts the blood-brain barrier in vivo," *Ultrasound in medicine & biology,* vol. 28, no. 3, pp. 389-400, 2002.

[45] N. McDannold, N. Vykhodtseva, and K. Hynynen, "Targeted disruption of the blood–brain barrier with focused ultrasound: association with cavitation activity," *Physics in Medicine & Biology,* vol. 51, no. 4, p. 793, 2006.

[46] M. Pan, G. Hong, H. Zheng, and Y. Fei, "Noninvasive Delivery of Adenoviral-Mediated Suicide Gene to Treat Glioma Through Focused Ultrasound-Induced BBB Opening," in *2018 IEEE International Ultrasonics Symposium (IUS)*, 2018, pp. 1-4: IEEE.

[47] C.-Y. Lin *et al.*, "Focused ultrasound-induced blood brain-barrier opening enhanced vascular permeability for GDNF delivery in Huntington's disease mouse model," *Brain stimulation,* 2019.

[48] N. Todd, Y. Zhang, M. Livingstone, D. Borsook, and N. McDannold, "The neurovascular response is attenuated by focused ultrasound-mediated disruption of the blood-brain barrier," *NeuroImage,* vol. 201, p. 116010, 2019.

[49] M. G. Z. Ghali, V. M. Srinivasan, and P. Kan, "Focused ultrasound-mediated blood brain barrier disruption in the enhancement of delivery of brain tumor therapies," *World neurosurgery,* 2019.

[50] A. Abrahao *et al.*, "First-in-human trial of blood–brain barrier opening in amyotrophic lateral sclerosis using MR-guided focused ultrasound," *Nature communications,* vol. 10, no. 1, pp. 1-9, 2019.

[51] S. ANDO *et al.*, "Non-touch, Quick Removal of an Occluding Intratracheal Balloon Using High Intensity Focused Ultrasound and Limonene Emulsion," *The Showa University Journal of Medical Sciences,* vol. 30, no. 3, pp. 351-357, 2018.

[52] S. M. Uddin and Y.-X. Qin, "Enhancement of osteogenic differentiation and proliferation in human mesenchymal stem cells by a modified low intensity ultrasound stimulation under simulated microgravity," *PloS one,* vol. 8, no. 9, p. e73914, 2013.

[53] E. B. Rego, T. Takata, K. Tanne, and E. Tanaka, "Suppl 1: Current Status of Low Intensity Pulsed Ultrasound for Dental Purposes," *The open dentistry journal,* vol. 6, p. 220, 2012.

[54] S. J. Warden, K. L. Bennell, J. M. McMeeken, and J. D. Wark, "Can conventional therapeutic ultrasound units be used to accelerate fracture repair?," *Physical therapy reviews,* vol. 4, no. 2, pp. 117-126, 1999.

[55] U. Farkash, O. Bain, A. Gam, M. Nyska, and P. Sagiv, "Low-intensity pulsed ultrasound for treating delayed union scaphoid fractures: case series," *Journal of orthopaedic surgery and research,* vol. 10, no. 1, p. 72, 2015.

[56] B. G. Dijkman, S. Sprague, and M. Bhandari, "Low-intensity pulsed ultrasound: Nonunions," *Indian journal of orthopaedics,* vol. 43, no. 2, p. 141, 2009.

[57] R. W. Poolman *et al.*, "Low intensity pulsed ultrasound (LIPUS) for bone healing: a clinical practice guideline," *bmj,* vol. 356, p. j576, 2017.

[58] F. Perks and A. Simpson, "What is the role of ultrasound in fracture management?," *Bone,* vol. 2018, no. 0215, p. r2, 2019.

[59] L. Sun *et al.*, "Inhibition of myostatin signal pathway may be involved in low-intensity pulsed ultrasound promoting bone healing," *Journal of Medical Ultrasonics,* vol. 46, no. 4, pp. 377-388, 2019.

[60] A. Loyola-Sánchez, J. Richardson, K. A. Beattie, C. Otero-Fuentes, J. D. Adachi, and N. J. MacIntyre, "Effect of low-intensity pulsed ultrasound on the cartilage repair in people with mild to moderate knee osteoarthritis: a double-blinded, randomized, placebo-controlled pilot study," *Archives of physical medicine and rehabilitation,* vol. 93, no. 1, pp. 35-42, 2012.

[61] L. Ren, Z. Yang, J. Song, Z. Wang, F. Deng, and W. Li, "Involvement of p38 MAPK pathway in low intensity pulsed ultrasound induced osteogenic differentiation of human periodontal ligament cells," *Ultrasonics,* vol. 53, no. 3, pp. 686-690, 2013.

[62] C. Liu, Y. Xu, H. Yang, and J. Zhang, "Establishment of axon regeneration regulatory network and the role of low intensity pulsed ultrasound in the network," *Saudi Journal of Biological Sciences,* 2019.

[63] N. E. Nicodemus *et al.*, "Focused transcranial ultrasound for treatment of neurodegenerative dementia," *Alzheimer's & Dementia: Translational Research & Clinical Interventions,* vol. 5, pp. 374-381, 2019.

[64] Y. Wu *et al.*, "Effects of therapeutic ultrasound for knee osteoarthritis: a systematic review and meta-analysis," *Clinical rehabilitation,* vol. 33, no. 12, pp. 1863-1875, 2019.

[65] K. Ikeda, T. Takayama, N. Suzuki, K. Shimada, K. Otsuka, and K. Ito, "Effects of low-intensity pulsed ultrasound on the differentiation of C2C12 cells," *Life sciences,* vol. 79, no. 20, pp. 1936-1943, 2006.

[66] S.-L. Huang, C.-W. Chang, Y.-H. Lee, and F.-Y. Yang, "Protective effect of low-intensity pulsed ultrasound on memory impairment and brain damage in a rat model of vascular dementia," *Radiology,* vol. 282, no. 1, pp. 113-122, 2016.

[67] S. Zhou, A. Schmelz, T. Seufferlein, Y. Li, J. Zhao, and M. G. Bachem, "Molecular mechanisms of low intensity pulsed ultrasound in human skin fibroblasts," *Journal of Biological Chemistry,* vol. 279, no. 52, pp. 54463-54469, 2004.

[68] K. Kirupa, S. Divya Mary, G. Vaishnavi, R. N. Nisha, J. R. Mercy, and G. Jaiganesh, "A comparative study of ultrasound therapy and transcutaneous electrical nerve stimulation in reducing pain for temporomandibular joint disorder," *Drug Invention Today,* vol. 12, no. 3, 2019.

[69] G. V. Forester, E. A. Peterson, and O. Z. Roy, "Effect of therapeutic level ultrasound on visual evoked potentials in the hypoxic cat," *Ultrasound in medicine & biology,* vol. 13, no. 5, pp. 259-265, 1987.

[70] A. Boutet *et al.*, "Focused ultrasound thalamotomy location determines clinical benefits in patients with essential tremor," *Brain,* vol. 141, no. 12, pp. 3405-3414, 2018.

[71] D. Daniels *et al.*, "Focused ultrasound-induced suppression of auditory evoked potentials in vivo," *Ultrasound in medicine & biology,* vol. 44, no. 5, pp. 1022-1030, 2018.

[72] P.-H. Tsui, S.-H. Wang, and C.-C. Huang, "In vitro effects of ultrasound with different energies on the conduction properties of neural tissue," *Ultrasonics,* vol. 43, no. 7, pp. 560-565, 2005.

[73] K. Cui, S. Zhang, J. Sun, X. Zhang, C. Ding, and G. Xu, "Inhibitory effect of ultrasonic stimulation on the voltage-dependent potassium currents in rat hippocampal CA1 neurons," *BMC neuroscience,* vol. 20, no. 1, p. 3, 2019.

[74] H. Kim *et al.*, "Miniature ultrasound ring array transducers for transcranial ultrasound neuromodulation of freely-moving small animals," *Brain stimulation,* vol. 12, no. 2, pp. 251-255, 2019.

[75] V. Velling and S. Shklyaruk, "Modulation of the functional state of the brain with the aid of focused ultrasonic action," *Neuroscience and behavioral physiology,* vol. 18, no. 5, pp. 369-375, 1988.

[76] L. Gavrilov, "Use of focused ultrasound for stimulation of nerve structures," *Ultrasonics,* vol. 22, no. 3, pp. 132-138, 1984.

[77] E. N. Harvey, "The effect of high frequency sound waves on heart muscle and other irritable tissues," *American Journal of Physiology-Legacy Content,* vol. 91, no. 1, pp. 284-290, 1929.

[78] F. Fry, H. Ades, and W. Fry, "Production of reversible changes in the central nervous system by ultrasound," *Science,* vol. 127, no. 3289, pp. 83-84, 1958.

[79] M. R. Bachtold, P. C. Rinaldi, J. P. Jones, F. Reines, and L. R. Price, "Focused ultrasound modifications of neural circuit activity in a mammalian brain," *Ultrasound in medicine & biology,* vol. 24, no. 4, pp. 557-565, 1998.

[80] G. Clement and K. Hynynen, "A non-invasive method for focusing ultrasound through the human skull," *Physics in Medicine & Biology,* vol. 47, no. 8, p. 1219, 2002.

[81] K. Hynynen *et al.*, "500-element ultrasound phased array system for noninvasive focal surgery of the brain: A preliminary rabbit study with ex vivo human skulls," *Magnetic Resonance in Medicine: An Official Journal of the International Society for Magnetic Resonance in Medicine,* vol. 52, no. 1, pp. 100-107, 2004.

[82] J. L. Foley, J. W. Little, and S. Vaezy, "Effects of high-intensity focused ultrasound on nerve conduction," *Muscle & Nerve: Official Journal of the American Association of Electrodiagnostic Medicine,* vol. 37, no. 2, pp. 241-250, 2008.

[83] M. L. Khraiche, W. B. Phillips, N. Jackson, and J. Muthuswamy, "Ultrasound induced increase in excitability of single neurons," in *2008 30th Annual International Conference of the IEEE Engineering in Medicine and Biology Society*, 2008, pp. 4246-4249: IEEE.

[84] W. J. Tyler, Y. Tufail, M. Finsterwald, M. L. Tauchmann, E. J. Olson, and C. Majestic, "Remote excitation of neuronal circuits using low-intensity, low-frequency ultrasound," *PloS one,* vol. 3, no. 10, p. e3511, 2008.

[85] V. Colucci, G. Strichartz, F. Jolesz, N. Vykhodtseva, and K. Hynynen, "Focused ultrasound effects on nerve action potential in vitro," *Ultrasound in medicine & biology,* vol. 35, no. 10, pp. 1737-1747, 2009.

[86] Y. Tufail *et al.*, "Transcranial pulsed ultrasound stimulates intact brain circuits," *Neuron,* vol. 66, no. 5, pp. 681-694, 2010.

[87] S.-S. Yoo *et al.*, "Focused ultrasound modulates region-specific brain activity," *Neuroimage,* vol. 56, no. 3, pp. 1267-1275, 2011.

[88] P. S. Yang *et al.*, "Transcranial focused ultrasound to the thalamus is associated with reduced extracellular GABA levels in rats," *Neuropsychobiology,* vol. 65, no. 3, pp. 153-160, 2012.

[89] W. Legon, A. Rowlands, A. Opitz, T. F. Sato, and W. J. Tyler, "Pulsed ultrasound differentially stimulates somatosensory circuits in humans as indicated by EEG and FMRI," *PloS one,* vol. 7, no. 12, p. e51177, 2012.

[90] H. Kim, S. J. Taghados, K. Fischer, L.-S. Maeng, S. Park, and S.-S. Yoo, "Noninvasive transcranial stimulation of rat abducens nerve by focused ultrasound," *Ultrasound in medicine & biology,* vol. 38, no. 9, pp. 1568-1575, 2012.

[91] R. L. King, J. R. Brown, W. T. Newsome, and K. B. Pauly, "Effective parameters for ultrasound-induced in vivo neurostimulation," *Ultrasound in medicine & biology,* vol. 39, no. 2, pp. 312-331, 2013.

[92] T. Deffieux, Y. Younan, N. Wattiez, M. Tanter, P. Pouget, and J.-F. Aubry, "Low-intensity focused ultrasound modulates monkey visuomotor behavior," *Current Biology,* vol. 23, no. 23, pp. 2430-2433, 2013.

[93] M. D. Menz, Ö. Oralkan, P. T. Khuri-Yakub, and S. A. Baccus, "Precise neural stimulation in the retina using focused ultrasound," *Journal of Neuroscience,* vol. 33, no. 10, pp. 4550-4560, 2013.

[94] E. J. Juan, R. González, G. Albors, M. P. Ward, and P. Irazoqui, "Vagus nerve modulation using focused pulsed ultrasound: potential applications and

preliminary observations in a rat," *International journal of imaging systems and technology,* vol. 24, no. 1, pp. 67-71, 2014.

[95]   H. Kim, A. Chiu, S. D. Lee, K. Fischer, and S.-S. Yoo, "Focused ultrasound-mediated non-invasive brain stimulation: examination of sonication parameters," *Brain stimulation,* vol. 7, no. 5, pp. 748-756, 2014.

[96]   R. L. King, J. R. Brown, and K. B. Pauly, "Localization of ultrasound-induced in vivo neurostimulation in the mouse model," *Ultrasound in medicine & biology,* vol. 40, no. 7, pp. 1512-1522, 2014.

[97]   W. Legon *et al.*, "Transcranial focused ultrasound modulates the activity of primary somatosensory cortex in humans," *Nature neuroscience,* vol. 17, no. 2, p. 322, 2014.

[98]   J. Mueller, W. Legon, A. Opitz, T. F. Sato, and W. J. Tyler, "Transcranial focused ultrasound modulates intrinsic and evoked EEG dynamics," *Brain stimulation,* vol. 7, no. 6, pp. 900-908, 2014.

[99]   H. Kim, M. Y. Park, S. D. Lee, W. Lee, A. Chiu, and S.-S. Yoo, "Suppression of EEG visual-evoked potentials in rats via neuromodulatory focused ultrasound," *Neuroreport,* vol. 26, no. 4, p. 211, 2015.

[100]   D. W. Gulick, T. Li, J. A. Kleim, and B. C. Towe, "Comparison of electrical and ultrasound neurostimulation in rat motor cortex," *Ultrasound in medicine & biology,* vol. 43, no. 12, pp. 2824-2833, 2017.

[101]   S. Han, M. Kim, H. Kim, H. Shin, and I. Youn, "Ketamine inhibits ultrasound stimulation-induced neuromodulation by blocking cortical neuron activity," *Ultrasound in medicine & biology,* vol. 44, no. 3, pp. 635-646, 2018.

[102] G. Li *et al.*, "Local field potentials responses of ultrasonic neuromodulation in freely moving mouse," in *2017 IEEE International Ultrasonics Symposium (IUS)*, 2017, pp. 1-4: IEEE.

[103] H. Guo *et al.*, "Ultrasound produces extensive brain activation via a cochlear pathway," *Neuron,* vol. 98, no. 5, pp. 1020-1030. e4, 2018.

[104] P. Xie, S. Zhou, X. Wang, Y. Wang, and Y. Yuan, "Effect of pulsed transcranial ultrasound stimulation at different number of tone-burst on cortico-muscular coupling," *BMC neuroscience,* vol. 19, no. 1, p. 60, 2018.

[105] W. Lee, P. Croce, R. W. Margolin, A. Cammalleri, K. Yoon, and S.-S. Yoo, "Transcranial focused ultrasound stimulation of motor cortical areas in freely-moving awake rats," *BMC neuroscience,* vol. 19, no. 1, p. 57, 2018.

[106] G. Li *et al.*, "Noninvasive ultrasonic neuromodulation in freely moving mice," *IEEE Transactions on Biomedical Engineering,* vol. 66, no. 1, pp. 217-224, 2019.

[107] W. Legon, P. Bansal, R. Tyshynsky, L. Ai, and J. K. Mueller, "Transcranial focused ultrasound neuromodulation of the human primary motor cortex," *Scientific reports,* vol. 8, 2018.

[108] X. Wang, J. Yan, Z. Wang, X. Li, and Y. Yuan, "Neuromodulation effects of ultrasound stimulation under different parameters on mouse motor cortex," *IEEE Transactions on Biomedical Engineering,* 2019.

[109] A. L. Hodgkin and A. F. Huxley, "A quantitative description of membrane current and its application to conduction and excitation in nerve," *The Journal of physiology,* vol. 117, no. 4, pp. 500-544, 1952.

[110] J. Tian *et al.*, "A mechanoelectrical coupling model of neurons under stretching," *Journal of the mechanical behavior of biomedical materials,* vol. 93, pp. 213-221, 2019.

[111] T. Lemaire, E. Neufeld, N. Kuster, and S. Micera, "Understanding ultrasound neuromodulation using a computationally efficient and interpretable model of intramembrane cavitation," *Journal of Neural Engineering,* 2019.

[112] W. J. Tyler, "The mechanobiology of brain function," *Nature Reviews Neuroscience,* vol. 13, no. 12, p. 867, 2012.

[113] J. K. Mueller and W. J. Tyler, "A quantitative overview of biophysical forces impinging on neural function," *Physical biology,* vol. 11, no. 5, p. 051001, 2014.

[114] T. D. Nguyen *et al.*, "Piezoelectric nanoribbons for monitoring cellular deformations," *Nature nanotechnology,* vol. 7, no. 9, p. 587, 2012.

[115] A. Auerbach, "The energy and work of a ligand-gated ion channel," *Journal of molecular biology,* vol. 425, no. 9, pp. 1461-1475, 2013.

[116] S. Vlad and R. V. Ciupa, *International Conference on Advancements of Medicine and Health Care through Technology; 5th–7th June 2014, Cluj-Napoca, Romania: MEDITECH 2014*. Springer, 2014.

[117] H. Lodish, A. Berk, S. L. Zipursky, P. Matsudaira, D. Baltimore, and J. Darnell, "Intracellular ion environment and membrane electric potential," in *Molecular Cell Biology. 4th edition*: WH Freeman, 2000.

[118] P.-C. Zhang, A. M. Keleshian, and F. Sachs, "Voltage-induced membrane movement," *Nature,* vol. 413, no. 6854, p. 428, 2001.

[119] A. G. Petrov, "Electricity and mechanics of biomembrane systems: flexoelectricity in living membranes," *Analytica chimica acta,* vol. 568, no. 1-2, pp. 70-83, 2006.

[120] A. Chen and V. T. Moy, "Cross-linking of cell surface receptors enhances cooperativity of molecular adhesion," *Biophysical Journal,* vol. 78, no. 6, pp. 2814-2820, 2000.

[121] Y. Tufail, A. Yoshihiro, S. Pati, M. M. Li, and W. J. Tyler, "Ultrasonic neuromodulation by brain stimulation with transcranial ultrasound," *nature protocols,* vol. 6, no. 9, p. 1453, 2011.

[122] W. D. O'Brien Jr, "Ultrasound–biophysics mechanisms," *Progress in biophysics and molecular biology,* vol. 93, no. 1-3, pp. 212-255, 2007.

[123] G. Ter Haar, "Therapeutic applications of ultrasound," *Progress in biophysics and molecular biology,* vol. 93, no. 1-3, pp. 111-129, 2007.

[124] A. Bystritsky *et al.*, "A review of low-intensity focused ultrasound pulsation," *Brain stimulation,* vol. 4, no. 3, pp. 125-136, 2011.

[125] F. A. Jolesz, "MRI-guided focused ultrasound surgery," *Annual review of medicine,* vol. 60, pp. 417-430, 2009.

[126] L. D. Johns, "Nonthermal effects of therapeutic ultrasound: the frequency resonance hypothesis," *Journal of athletic training,* vol. 37, no. 3, p. 293, 2002.

[127] C. E. Morris and P. F. Juranka, "Nav channel mechanosensitivity: activation and inactivation accelerate reversibly with stretch," *Biophysical journal,* vol. 93, no. 3, pp. 822-833, 2007.

[128] R. A. Wahab, M. Choi, Y. Liu, V. Krauthamer, V. Zderic, and M. R. Myers, "Mechanical bioeffects of pulsed high intensity focused ultrasound on a simple neural model," *Medical physics,* vol. 39, no. 7Part1, pp. 4274-4283, 2012.

[129] R. T. Mihran, F. S. Barnes, and H. Wachtel, "Temporally-specific modification of myelinated axon excitability in vitro following a single ultrasound pulse," *Ultrasound in medicine & biology,* vol. 16, no. 3, pp. 297-309, 1990.

[130] Food and D. Administration, "Guidance for Industry and FDA Staff Information for Manufacturers Seeking Marketing Clearance of Diagnostic Ultrasound Systems and Transducers," *Silver Spring, MD: Author,* 2008.

[131] M. Fini and W. J. Tyler, "Transcranial focused ultrasound: a new tool for non-invasive neuromodulation," *International Review of Psychiatry,* vol. 29, no. 2, pp. 168-177, 2017.

[132] W. J. Tyler, S. W. Lani, and G. M. Hwang, "Ultrasonic modulation of neural circuit activity," *Current opinion in neurobiology,* vol. 50, pp. 222-231, 2018.